

Minor Element Concentrations of Icelandic Olivines: Source or Process Controlled?

Lucy.E.L.Tweed

Part III Geological Sciences

University of Cambridge

Pembroke College

Supervisor: Dr John Maclennan

January 2014

Plagiarism Statement

I declare that the submitted work is my own, except where acknowledgement is given to the work of others or to work done in collaboration. I declare that I have read and understood the Department of Earth Sciences statement on plagiarism.

L.E.L.Tweed

January 2014

Abstract

Ni and Mn contents of olivines in primitive basalts are increasingly being used as a tool to infer the presence of lithological variations in their mantle source regions. In particular, high Ni and low Mn concentrations have been argued to indicate a large contribution to the melting from olivine-free recycled lithologies. Minor element concentrations are influenced both by source composition and processes including partial melting and fractional crystallisation. To understand whether these minor element signals are truly diagnostic of lithological source heterogeneity it is necessary to disentangle these source and process controls.

A forward model of isobaric, non-modal fractional melting of peridotitic mantle during adiabatic decompression melting is developed. Changes in melt fraction, temperature, modal mineralogy of the solid residue, and major and trace element concentrations of the incremental melt fractions are tracked through the melting column. The range in compositions of primitive olivine phenocrysts crystallised at the shallow basalt liquidus are determined. The model assesses the partitioning behaviour of first row transition elements (FRTE) including Ni and Mn using data from recent studies.

Major and minor element analyses are carried out on olivine phenocrysts from five geographically dispersed Icelandic eruptions. Ranges of 1200pm and 1500ppm are found in the Ni and Mn concentrations respectively, with a large part of this variation correlating with olivine fractionation. At given Fo ranges of 800ppm and 300ppm are observed in Ni and Mn respectively.

Model results are compared to measured compositions of Icelandic olivines and published olivine data from a range of geodynamic settings. It is found that almost all measured Ni and Mn are compatible with model predictions of fractional melting of pyrolytic peridotite. Ni and Mn signatures that have previously been attributed to pyroxenite melting are dominantly controlled by variation in mantle T_p and lithospheric thickness. The comparison indicates that a single source composition cannot account for all the variation in Ni and Mn. The variation in initial bulk Ni and Mn concentration of the peridotite required to match the data is in line with published estimates based on mantle xenoliths and abyssal peridotites. Preferential sampling of the high Ni and low Mn source in areas overlain by thick lithosphere indicates that compositional variation is convolved with fusibility and hence mineralogy of the source. The variation in Ni and Mn concentrations between olivines from a single sample and from different Icelandic eruptions implies that lithological heterogeneity occurs on a short lengthscale within the mantle plume.

When source variability is permitted, data can be fit by any degree of melt mixing. The absence of highly forsteritic olivine ($Fo > 92$) predicted for instantaneous fractional melts generated at shallow levels does however imply that some mixing of melts occurs.

Contents

1	Introduction	5
1.1	Project Rationale	5
1.1.1	Mantle heterogeneity	5
1.1.2	Sampling major and minor element heterogeneity	6
1.1.3	Fractional melting control on minor element partitioning	7
1.2	Aims	8
2	Fieldwork	9
2.1	Sample Collection	9
2.2	Sample Selection and Description	10
3	Microanalysis	12
3.1	Sample Preparation	12
3.2	Analysis	14
4	Microanalysis Results	15
5	Fractional Melting Model	30
5.1	Melting Path	31
5.2	Modal mineralogy of residue	34
5.3	Melt Composition	39
5.3.1	Major element melt composition	42
5.3.2	Minor element melt composition	43
5.4	Olivine crystallisation	46
6	Fractional Melting Model Results	47
6.1	Effect of changing input variables	54
7	Discussion	59
7.1	Comparison of model to olivine data: Can fractional melting do it?	59
7.2	Constraints on mantle source heterogeneity	71
8	Conclusions	72
9	Acknowledgements	78
10	Self-Assesment	79
A	Project Proposal	80
B	Major and trace element data	81
C	Matlab Code	92

1 Introduction

1.1 Project Rationale

1.1.1 Mantle heterogeneity

Recycling of oceanic crust into the mantle is an integral part of plate tectonics, with oceanic lithosphere being generated at mid-ocean ridges and recycled back into the mantle at subduction zones. This geodynamic cycle is important in generating mantle heterogeneity (Stracke *et al.*, 2003). Recycled oceanic lithosphere comprising enriched oceanic crust and the complementary highly depleted upper mantle (Allègre and Turcotte, 1986) undergoes both mechanical mixing and chemical reaction within the principally peridotitic convecting mantle.

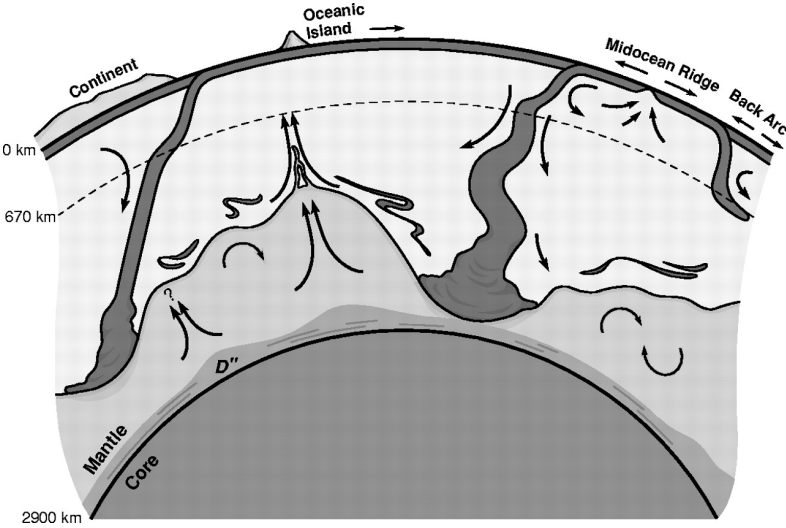


Figure 1.1: Schematic diagram reproduced from Kellogg [1999] illustrating the role of subduction in generating mantle heterogeneity. The mode of convection and the form and scale of the heterogeneities within the mantle remain unclear, representing an active area of research. Thus this diagram illustrates just one model of the possible processes.

Basalt geochemistry is the principle tool for sampling variation in mantle composition. Variations in radiogenic isotope ratios and trace element concentrations in mantle-derived basalts have long been used to demonstrate that Earth's mantle is chemically heterogeneous (e.g. Hofmann and White, 1982; Zindler and Hart, 1986; Stracke *et al.*, 2005). The enriched recycled lithologies have been invoked as a source for ocean island basalts (OIBs); providing an explanation for the high incompatible trace element concentrations and enriched isotopic ratios of OIBs relative to mid-ocean ridge basalt (MORB) (e.g. Hofmann and White, 1982).

More recently it has been shown that isotopic variation correlates with major and minor element variability of erupted basalts (Dasgupta *et al.*, 2010; Hauri, 1996) suggesting that isotopic end-members correspond to lithological or mineralogical heterogeneities in the mantle source regions. Constraining the nature of the major element heterogeneity is paramount as it is major element chemistry that controls the physical and chemical properties of the mantle which are important in the analysis of both geochemical and geophysical data. Constraints on the nature and quantification of the amount of recycled lithologies in the source region of OIBs would also provide insights into the distribution of recycled lithologies in the upper mantle and the processes that create, modify, and destroy heterogeneities in Earth's interior.

1.1.2 Sampling major and minor element heterogeneity

First-row transition elements (FRTE), including Sc, Ti, V, Cr, Mn, Fe, Co, Ni, Cu, and Zn, have emerged as potential indicators of basalt petrogenesis. They are present in minor abundance in the Earth's mantle, are compatible or only mildly incompatible during partial melting in Earth's mantle and unlike incompatible trace elements are insensitive to the extent of melting (Davis *et al.*, 2013). The relative compatibilities of these elements in different mantle phases causes their ratios in erupted lavas to be controlled by the residual phases in equilibrium with the partial melts. Thus they are potential tracers of mineralogical heterogeneity.

A number of high-profile recent publications have used the minor element contents of olivines contained in primitive basalts to infer the presence of large quantities of recycled basaltic material in their mantle source regions. It has been argued that the observed high Ni and low Ca and Mn concentrations cannot be generated by a peridotitic source, but rather that an olivine-free pyroxenite source component is required (Sobolev *et al.*, 2005, 2007; Herzberg, 2011). In their model Si-rich melts derived by deep (190–180 km) melting of eclogitic recycled oceanic crust react with peridotite producing olivine-free pyroxenite (Sobolev *et al.*, 2005; Yaxley and Green, 2000). At a given pressure and temperature melting of this hybrid olivine-free lithology is more voluminous than melting of peridotite meaning aggregate melts will be biased toward those derived from pyroxenite (Pertermann and Hirschmann, 2003). The lower compatibility of Ni and higher compatibility of Mn and Ca in pyroxene relative to olivine means pyroxenite-derived melts are characteristically enriched in Si and Ni but depleted in Mg, Ca, and Mn compared with their peridotite-derived counterparts.

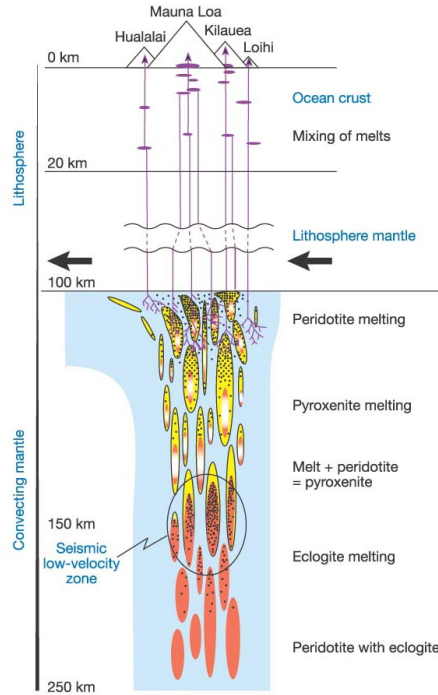


Figure 1.2: Hybrid pyroxenite melting model for Hawaii reproduced from Sobolev *et al.* [2005]. A similar model has been proposed for melting beneath Iceland and other mantle plumes. Recycled material is concentrated in the plume centre. Recycled eclogite is highly fusible and starts to melt at great depth. This melt disappears at lower pressures because it separates from eclogite and is consumed by reaction with peridotite to produce secondary pyroxenite (Sobolev *et al.*, 2005).

The assertion that a distinct olivine-free lithology is required has come under scrutiny with some researchers arguing that the olivine compositions can more simply be explained by partial melting of peridotites variably refertilized with MORB (Shorttle and MacLennan, 2011). Others highlight the importance of the conditions of melt generation over source mineralogy reasoning that, if variation in the partition coefficients as a function of pressure, temperature and melt composition are properly taken into consideration, the olivine compositions can be generated from partial melts of mineralogically homogeneous peridotite (Matzen *et al.*, 2013; Putirka *et al.*, 2011).

1.1.3 Fractional melting control on minor element partitioning

Major and trace element chemistry of mantle melts are controlled by depth and extent of melting and source composition as well as crustal processes including low-pressure fractional crystallisation and crustal assimilation. As a result major and trace element signatures inherited from the mineralogy of the source are difficult to uniquely distinguish. To meaningfully constrain source mineralogy its affect must be considered in conjunction with all other processes and variables involved in the generation and modification of melts prior to their eruption at the surface.

In light of this, an important problem with many previous studies of the behavior of FRTE in olivine is that they have included overly simplistic approximations of the mantle melting process and have not used the most up-to-date partitioning models. Generation of melt in the mantle is thought to be dominated by polybaric fractional melting (Kelemen *et al.*, 1997), however many previous models are based on assumptions of isobaric, modal, batch melting. To make quantitative predictions of the amount of recycled material in the source region it is vital that the role of the melting process is properly addressed.

Accurately modelling the fractional melting process is important as it allows us to constrain whether the observed minor element contents of olivines from basalts can be generated by fractional melting of a peridotite alone or whether the involvement of enriched recycled lithologies is required.

1.2 Aims

- To obtain high precision measurements of FRTE concentrations in olivines from a number of primitive basaltic flows from Iceland to assess the variability in the composition of melts supplied from the mantle.
- To create a forward model of polybaric, non-modal fractional melting of peridotitic mantle during adiabatic decompression melting from which changes in melt fraction, temperature, modal mineralogy of the solid residue, and major and trace element concentrations of the incremental melt fractions can be tracked through the melting column.
- To determine the possible range in compositions of olivines crystallized from these fractional melts.
- To explore the role of fractional melting in creating the signatures that have previously been attributed to pyroxenite melting by comparing model results of Ni and Mn concentrations of primitive olivines to both the new Icelandic data and to published data from different geodynamic settings.

2 Fieldwork

2.1 Sample Collection

To study the variability of minor element concentrations in olivine from primitive basalts it is desirable to focus on an area where compositional heterogeneity of the melt supply from the mantle has been demonstrated and, ideally, where previous estimates of the proportion of recycled material in the source has been estimated. Iceland represents the only subaerial section of the Mid-Atlantic Ridge. Its easily accessible basaltic flows provide a unique record of mantle melting. Isotopic and trace element data from whole-rock samples indicate that the composition of mantle melts generated under the neovolcanic zones of Iceland is variable (e.g. Stracke *et al.*, 2003).

Fieldwork was undertaken in Iceland between the dates of 14/07/2013 and 30/08/2013. Approximately three weeks of this time were spent sampling primitive basalts and picrites along the neovolcanic zones. A number of localities were visited in the Northern Volcanic zone, the Western Volcanic zone, and on Reykjanes peninsula where hand specimens containing fresh olivine phenocrysts were collected.



Figure 2.1: Stafafell quarry on Reykjanes Peninsula where a section through a table mountain is exposed. The table mountain was formed during a subglacial eruption and comprises interlayered fragmented hyaloclasite and pillow basalts. The eruptive style (i.e. explosive phreatic eruptions producing fragmented hyaloclasite or effusive eruption of pillow basalts) depends on the thickness of overlying ice.

2.2 Sample Selection and Description

Five eruptions, representative of the diversity of Icelandic melt compositions were selected for microanalysis. In order to maximise spread in the data between enriched and depleted endmembers and to test the role of lithospheric thickness in controlling the distribution of melting within the mantle geographically dispersed eruptions were chosen. Along the axis of active spreading in the neovolcanic zones, active rift tectonics causes thinning of the lithosphere and allows mantle to upwell to shallow levels. The melts produced here have a large contribution from high melt fraction shallow melts and can thus be expected to be relatively depleted in incompatible trace elements. In contrast off-axis melting, where the lithosphere is not thinned by active rifting, the minimum depth to which the mantle upwells is higher. Melt fractions are lower and the melts produced are enriched in incompatible trace elements. Choosing both on-axis and flank zone basalts also allows us to test the hypothesis of recycled pyroxenite existing within the melting region. At the same Tp pyroxenite melts at higher pressure than peridotite, eruptions overlying thicker parts of the lithosphere would thus be expected to have greater proportional contribution from pyroxenite melting as shallow melting of peridotite is suppressed.

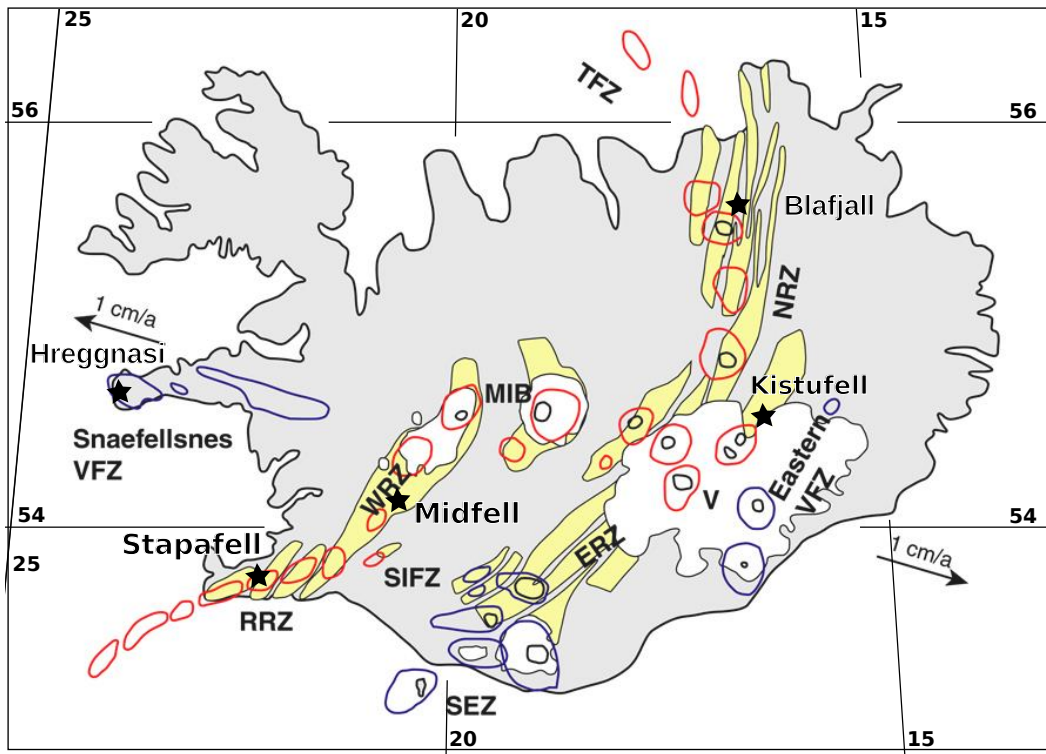


Figure 2.2: Map of Iceland showing locations of samples used in this study. Neovolcanic zones are marked in dark grey and are denoted: NVZ, Northern Vocanic zone; WVZ, Western Volcanic zone; REP, Reykjanes Peninsula; SF, Snaefellsnes.

Of the flows sampled in the summer of 2013, pillow lavas from the Stapafell, Midfell and Blafjall table mountains were selected (see locations in Figure 2.2). Added to these were pillow lava samples from Kistufell collected by Ben Winpenney, and pre-prepared olivine phenocrysts mounted in epoxy from Hreggnasi table mountain provided by Oliver Shorttle. Of these Hreggnasi is expected to represent the compositionally enriched endmember, while Kistufell is expected to be most depleted. Descriptions of the samples are given in Table 1.

Eruption	Sample name	Grid loc. (lat,long)	Type	Phenocrysts	References
Midfell	MH2013-G	64.1748, 021.0478	SGP, gl	ol, plag, cpx	Gurenko and Chaussidon, 1995
Stapafell	STAP01-13G	63.9010, 022.5431	SGP, gl	ol, plag	Gurenko and Sobolev, 2006 Shorttle and MacLennan, 2011
Kistufell	09KS-04	64.7938, 017.1752	SGP, gl	ol, plag	MacLennan, 2008b
Bláfjall	BLA2013-01WR	65.4883, 016.8453	SGP, int	ol	Breddam, 2002
Hreggnasi	CHRG10-5	64.8119, 23.387	SA-sc, gl	ol, plag	Schiellerup, 1995
					Peate <i>et al.</i> , 2010

Table 1: Description of samples selected for microanalysis. The samples are classified according to the type of eruption and the sample type as follows: SGP= sub-glacial pillow lavas; SA-sc= sub-aerial scoria cone; gl= glass; int= whole rock pillow interior.

3 Microanalysis

3.1 Sample Preparation

Samples were prepared for chemical analysis by first crushing the rocks. Handpicked olivine phenocrysts and glass chips were then mounted in epoxy and polished to expose the crystals and achieve a smooth surface. Phenocrysts from Midfell, Stapafell and Kistufell were picked from the glassy pillow rim samples, whereas those for Blafjall were picked from the pillow interior due to the scarcity of olivines in glassy samples.



Figure 3.1: Glassy pillow rim sample from Midfell prior to crushing. This sample was highly olivine-phyric containing ~15 vol%. It also contains fairly abundant plagioclase phenocrysts, some of which were megacrysts such as that seen in the top left of the image. Rarer green clinopyroxene was also present suggesting that this basalt started to crystallise deep within the crust.

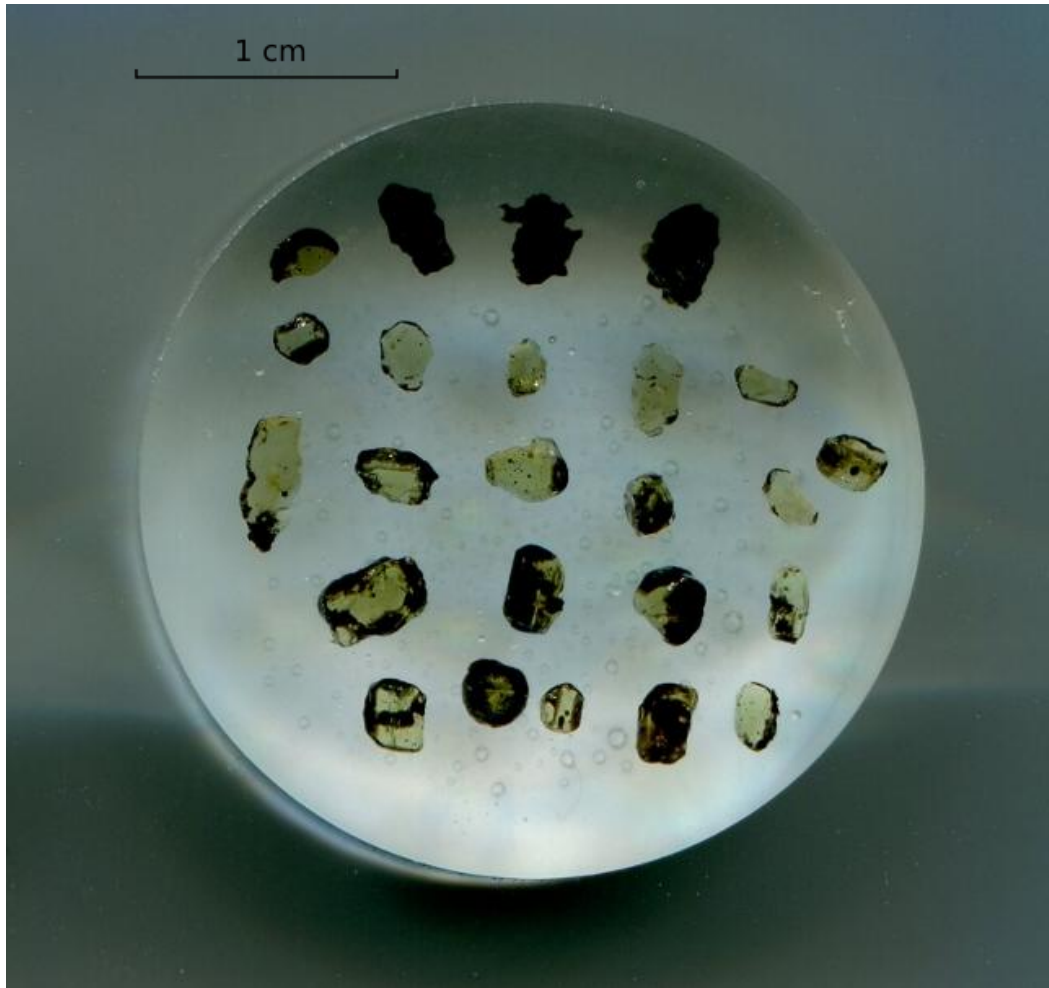


Figure 3.2: Epoxy mounted olivine phenocrysts from Stapafell

3.2 Analysis

Olivine phenocrysts were analyzed using the Cameca SX100 electron microprobe at the University of Cambridge. Five days were spent on the microprobe. Samples were analysed using an accelerating voltage of 15 keV and a beam size of 1 μm . For the first two days on the microprobe a single condition was used with all elements (Si, Ti, Mg, Fe, Mn, Ni, Ca, Al, Cr) measured at a high current of 60nA and counting times of 20s (Si, Fe, Mg), 40s (Ti, Cr) and 120s (Al, Mn, Ca, Ni). Data from this session yielded unexpectedly low totals of between 97-98wt% outside the acceptable range of 100 \pm 1%. These low totals were a result of the high current causing saturation of the detector for major elements. Thus the deficit in the totals was made up uniformly of the major elements (SiO₂, MgO, FeO). Despite minor and trace element data probably being unaffected, the data measured during this setup was discarded.

On the following three days two conditions were used with a beam current of 20nA (Si, Ti, Cr, Fe, Mg) or 60nA (Al, Mn, Ca, Ni, \pm P). Counting times of 20s (Si, Fe, Mg), 40s (Ti, Cr, P) or 120s (Al, Mn, Ca, Ni) were used. This setup yielded totals between 99-101% with most values lying in the range 99.5-100.5%.

Measurements were calibrated using the St Johns olivine standard. Olivine core compositions were analysed to avoid any diffusional overprint and three point measurements were taken per olivine to check their homogeneity and reduce analytical errors. The composition of each olivine was found by averaging the three measurements. In total 42 olivine phenocrysts were analyzed per flow.

Closely spaced linear profiles across several olivines were also measured, with at least one profile taken for each sample with the exception of Blafjall for which lack of glassy rims made it impossible to determine the edge of the crystal. These profiles allow the determination of presence and shape of mineral zonation and diffusional rim overprints.

Average errors ($\sigma_{av} = \frac{\frac{1}{n} \sum_i^n \sigma_i}{\sqrt{n}}$, n=3) from the counting statistics for each species are given in Table 2. Accuracy of the measurements is determined by comparison of the measured composition of the mineral standard with the accepted values. The minor elements of interest in this study (Mn, Ca, Ni) all have percentage errors less than 10%. The trace elements Ti, Cr and P have very high errors >100%, however their concentration is of little interest here and will not be included in further discussion.

	Major Elements				Minor Elements				Trace Elements		
	Si	Fe	Mg	Fo	Al	Mn	Ca	Ni	Ti	Cr	P
σ	0.28	0.33	0.48	0.47	0.0038	0.013	0.0078	0.011	0.016	0.018	0.0020
% error	1.5	3.1	1.8	0.55	14	8.3	3.7	6.1	430	120	320

Table 2: Average errors in the microprobe element concentrations from counting statistics. σ =standard deviation in wt%; % error= 100 σ /measured concentration]

4 Microanalysis Results

Results of the microprobe analysis are plotted in Figures 4.1-4.7 (full data tables provided in Appendix B). For comparison global data from different geodynamic settings from Sobolev *et al.* [2007] are also plotted. The Icelandic samples belong to the WPM-thin group corresponding to OIB erupted above thin lithosphere (<70km). They have intermediate concentrations of Ni, Mn and Ca sitting between WPM-thick and MORB.

Forsterite content (Fo) of the olivines ranges between 76.5-91.0mol% indicating variable extents of olivine fractionation. Midfell is the most primitive and Hreggnasi is the most evolved. Olivines from a single hand specimen have very variable compositions. Blafjall shows the greatest variability with Fo ranging from 78 to 90 mol%.

Ni and Mn strongly correlate with Fo. Since Ni is compatible in olivine progressive olivine fractionation causes the residual Ni concentration to decrease. Conversely, Mn is incompatible in olivine meaning Mn concentration increases with olivine fractionation. To constrain mantle source composition the effects of fractionation must be removed. Therefore in addition to Mn and Ni concentrations Mn/Fe and Ni/(Mg/Fe) ratios are also plotted. These ratios do not vary significantly with olivine fractionation. There is still some fractionation dependence, making it hard to make inferences about the primitive mantle melts for Hreggnasi due its high extents of fractionation.

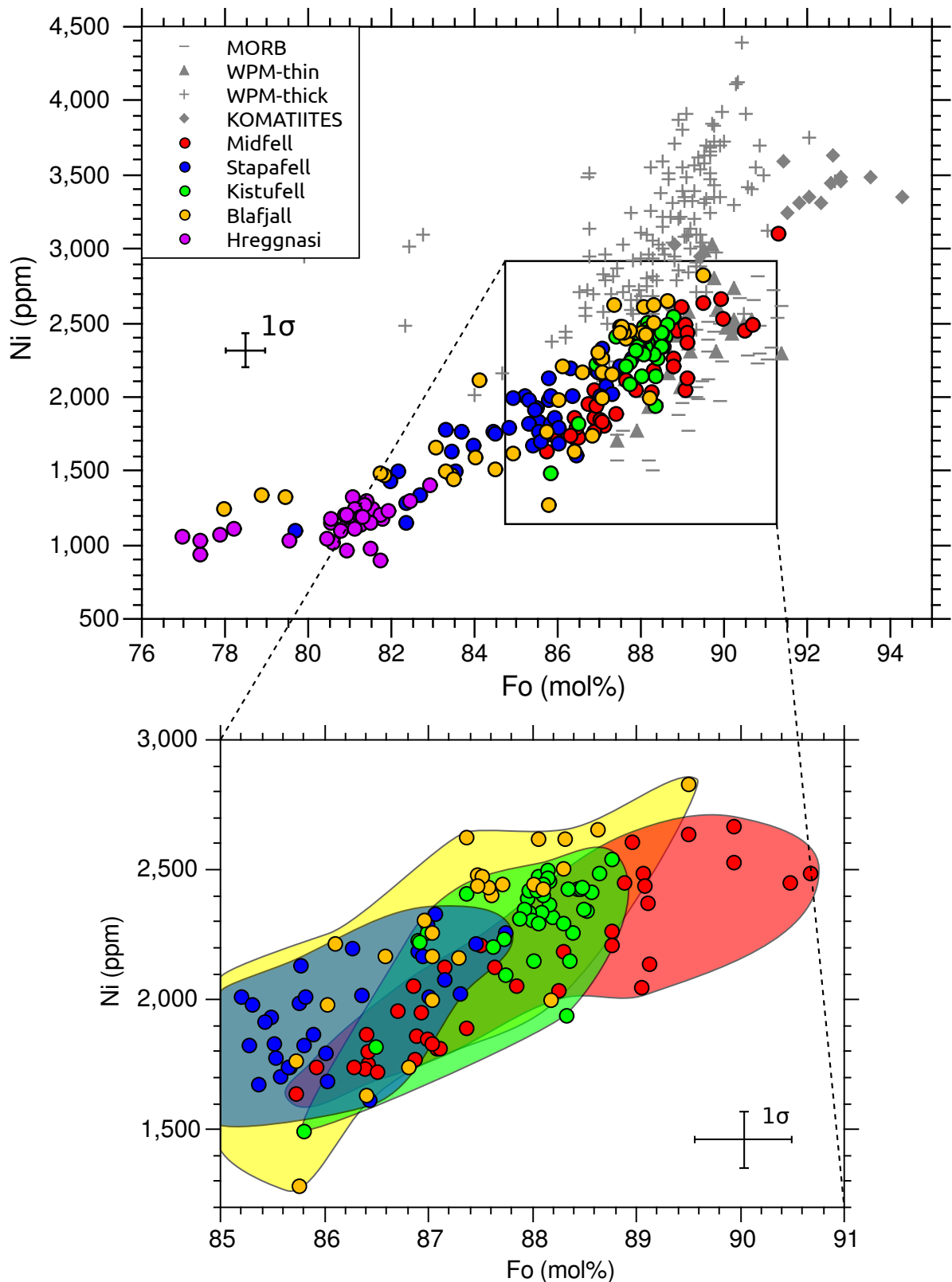


Figure 4.1: Ni content of olivines from five Icelandic eruptions with blow-up of the most primitive olivine data in which the distribution of olivines from different flow are shaded. plot with shaded regions showing the distribution of olivines from different flows. Each point is the average value of three point measurements taken at the core of each olivine. Representative 1σ error bars are shown. Data from Sobolev *et al.* [2007] are shown for comparison.

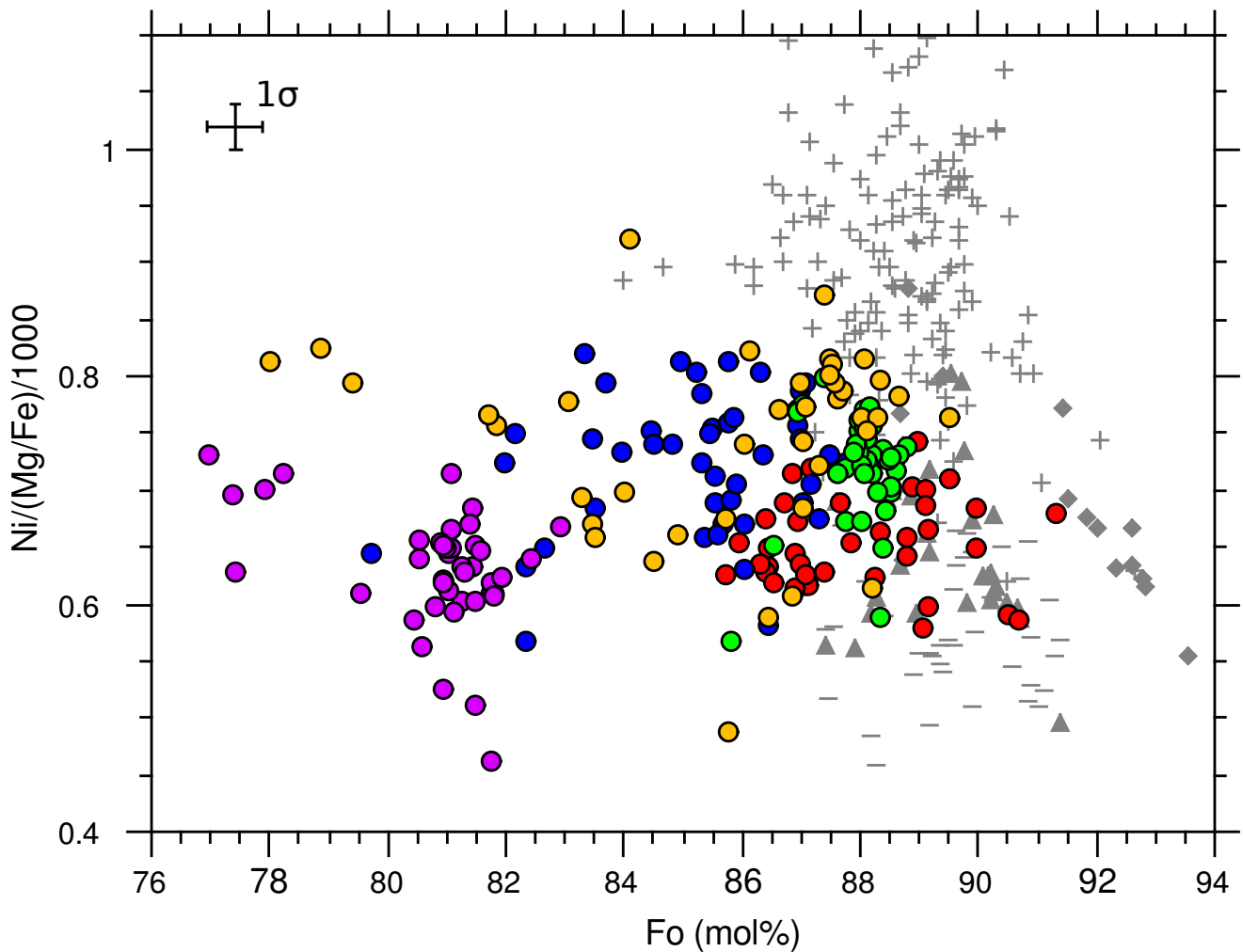


Figure 4.2: $\text{Ni}/(\text{Mg}/\text{Fe})/1000$ vs Fo . Plotted to remove effect of fractionation on Ni contents so that signatures from primitive mantle melts can be identified. Each point is the average value of three point measurements taken at the core of each olivine. Representative 1σ error bars are shown. Data from Sobolev *et al.* [2007] are shown for comparison.

There is significant overlap in Ni content and $\text{Ni}/(\text{Mg}/\text{Fe})$ ratio between different flows. Despite this some distinctions can be made. At a given Fo Midfell has the lowest Ni content followed by Kistufell and then Blafjall. At the same Fo , Stapafell has similar Ni to Blafjall.

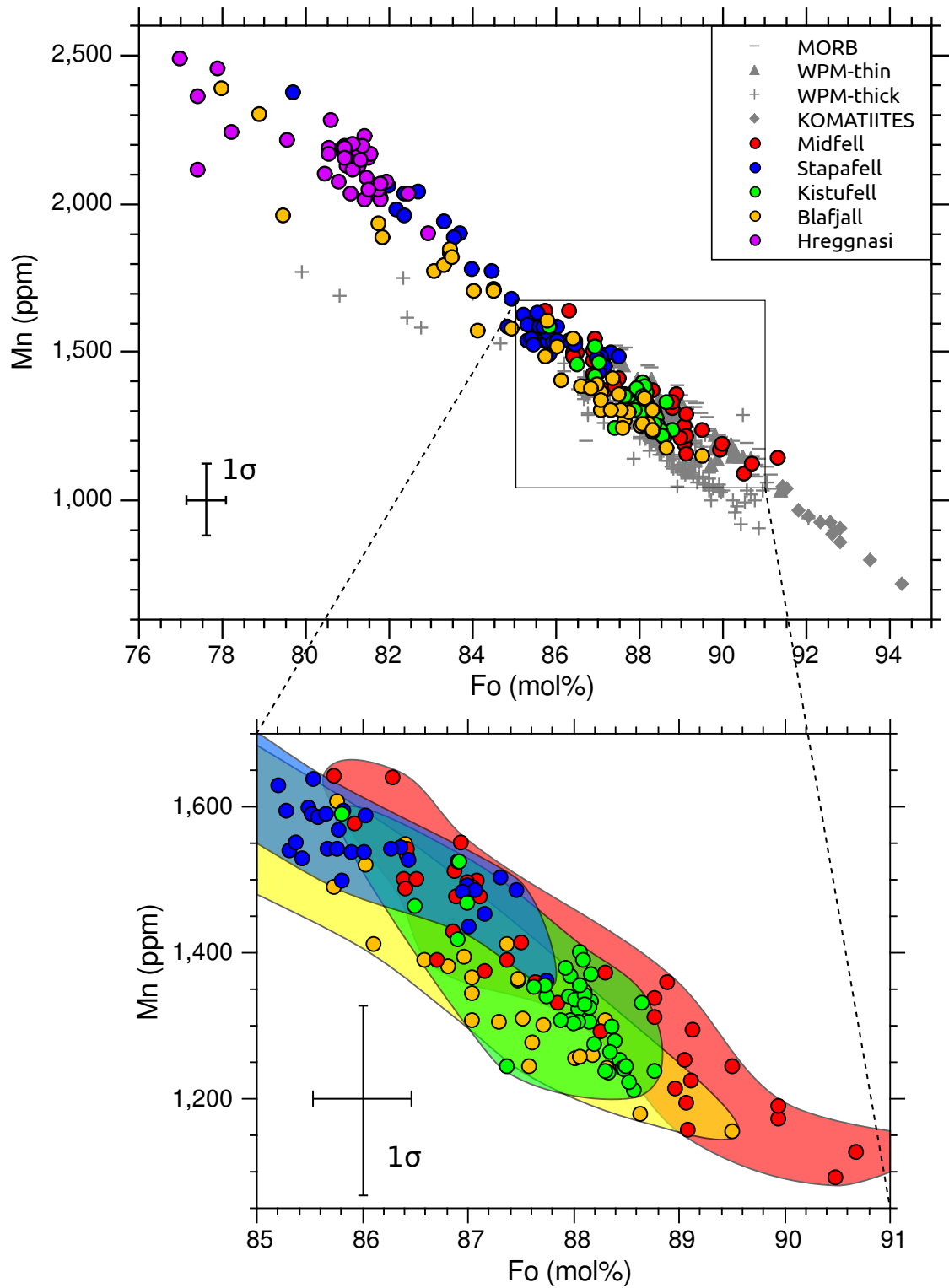


Figure 4.3: (A) Mn content of olivines from five Icelandic eruptions. (B) Close-up of plot (A) with shaded regions showing the distribution of olivines from different flows. (C) $100\text{Mn}/\text{Fe}$ vs Fo. Plotted to remove effect of fractionation on Mn contents so that signatures from primitive mantle melts can be identified. Each point is the average value of three point measurements taken at the core of each olivine. Representative 1σ error bars are shown for each plot. Data from Sobolev *et al.* [2007] are shown for comparison.

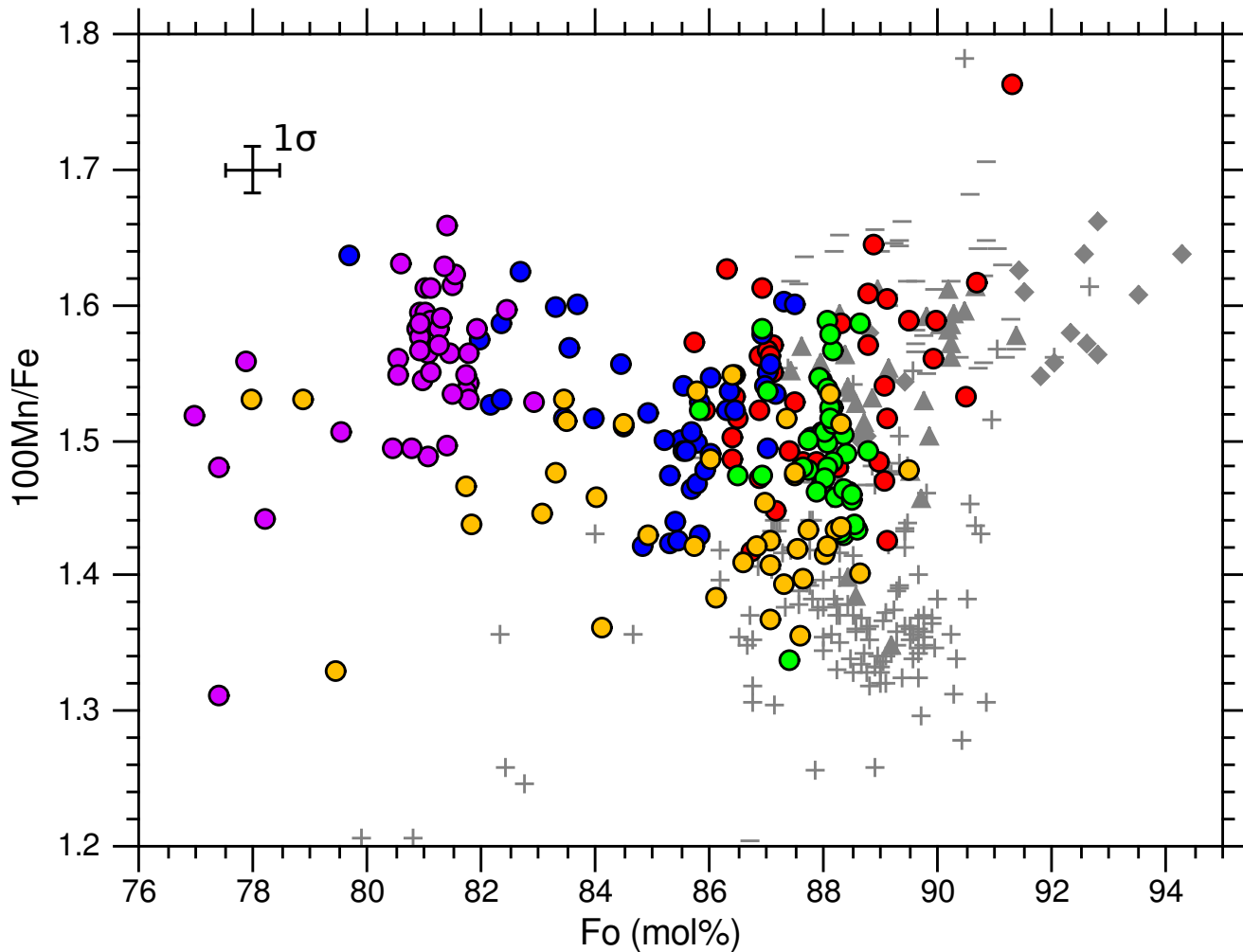


Figure 4.4:

Mn concentrations of the different eruptions also overlap considerably. Overall Midfell has the highest Mn at a given Fo, followed by Kistufell and then Blafjall. At the same Fo, Stapafell overlaps with both Stapafell and Kistufell.

Of the three more primitive basalts, Stapafell shows the greatest affinity for the WPM-thick group, while Midfell is more MORB-like. When Mn/Fe is plotted against Ni/(Mg/Fe) (Figure 4.5) an approximate negative linear correlation is observed for olivine from Midfell, Kistufell and Blafjall.

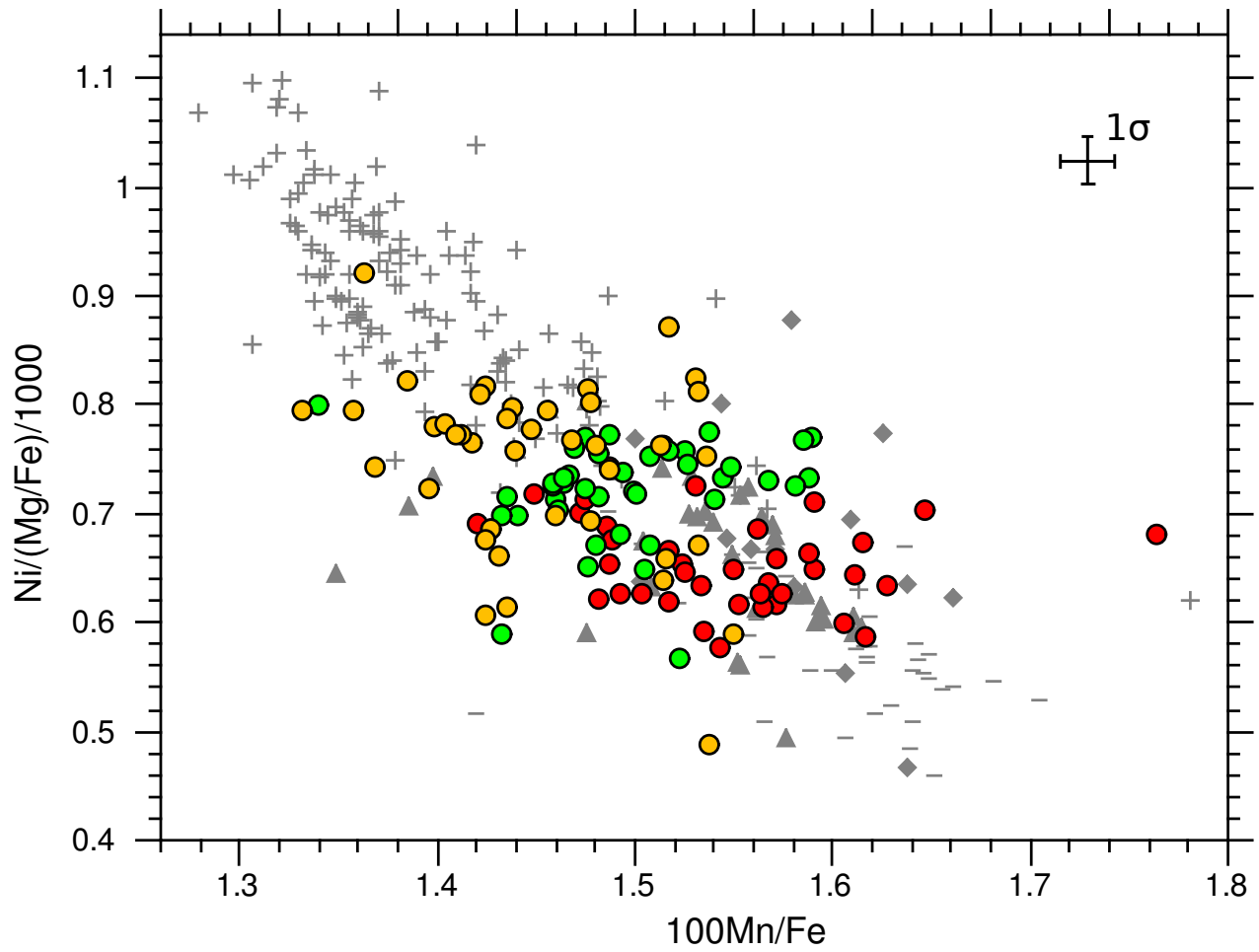


Figure 4.5: $\text{Ni}/(\text{Mg}/\text{Fe})/1000$ vs $100\text{Mn}/\text{Fe}$ for the three most primitive Icelandic flows: Midfell, Kistufell, Blafjall. Symbols are as defined in Figure 4.1. Representative 1σ error bars are shown for each plot. Points extend along the linear array defined by the global data of Sobolev *et al.* [2007].

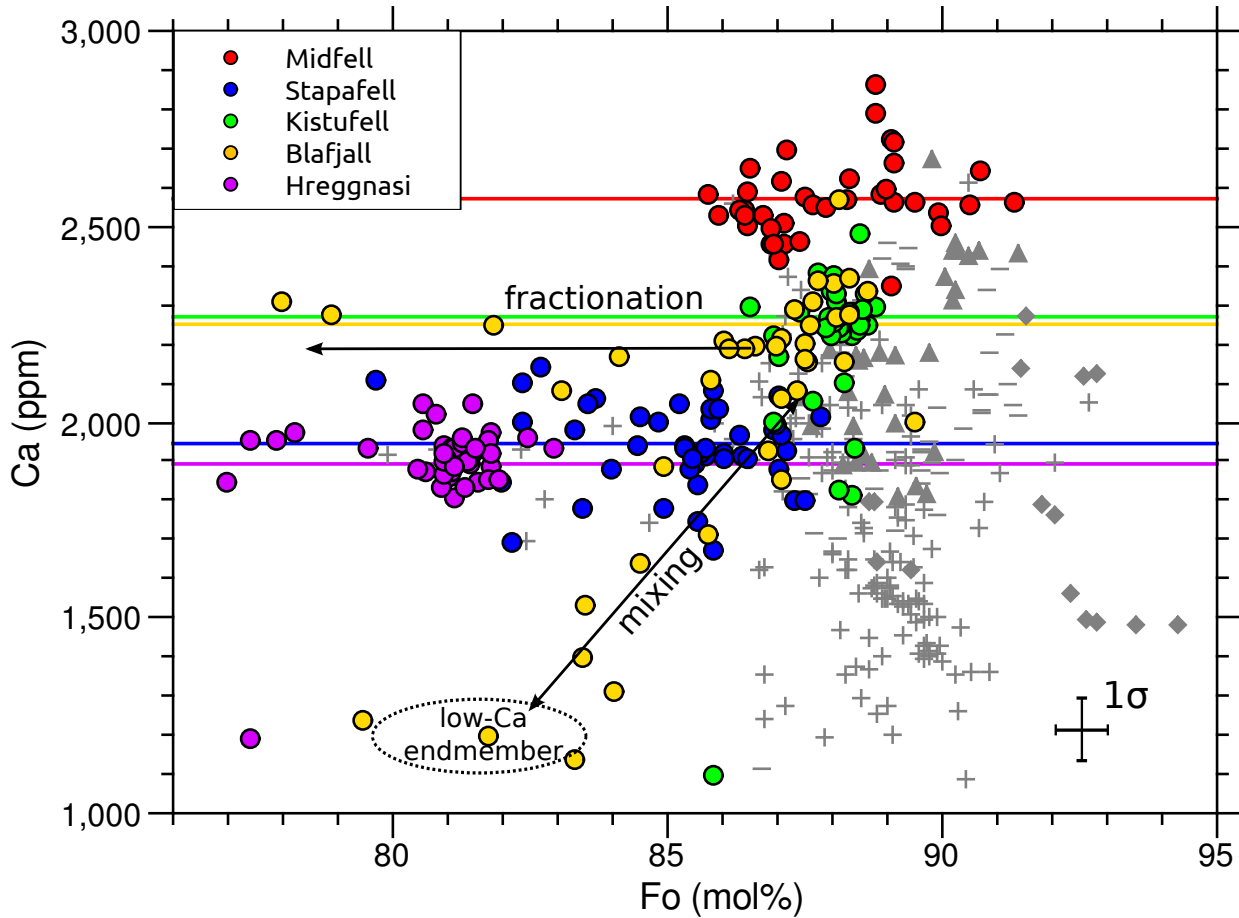


Figure 4.6: Ca content of olivines from five Icelandic eruptions. Annotations show rough vectors of olivine fractionation and a potential mixing trend with a low-Ca endmember. The horizontal lines show the average Ca content of all the olivines from each sample.

Ca is the parameter least dependent on olivine fractionation. Thus, it is diagnostic of parental magma compositional differences. More variation is seen in Ca between the different flows than in Mn/Fe or Ni/(Mg/Fe) ratios. Midfell is the most enriched in Ca while Hreggnasi and Stapafell are depleted in Ca and Kistufell and Blafjall have intermediate concentrations. Midfell has unusually high Ca concentrations, projecting above most MORB samples.

The Ca concentrations agree with expectations. Hreggnasi and Stapafell occur in the flank zones where the lithosphere is thick due to the absence of active extensional tectonics. The geodynamic setting is thus more similar to that of the WPM-thick group. Midfell, Kistufell and Blafjall occur within the neo-volcanic zones where the lithosphere is thinned by active rifting. The greater contribution from shallow melting means they have greater affinity to MORB.

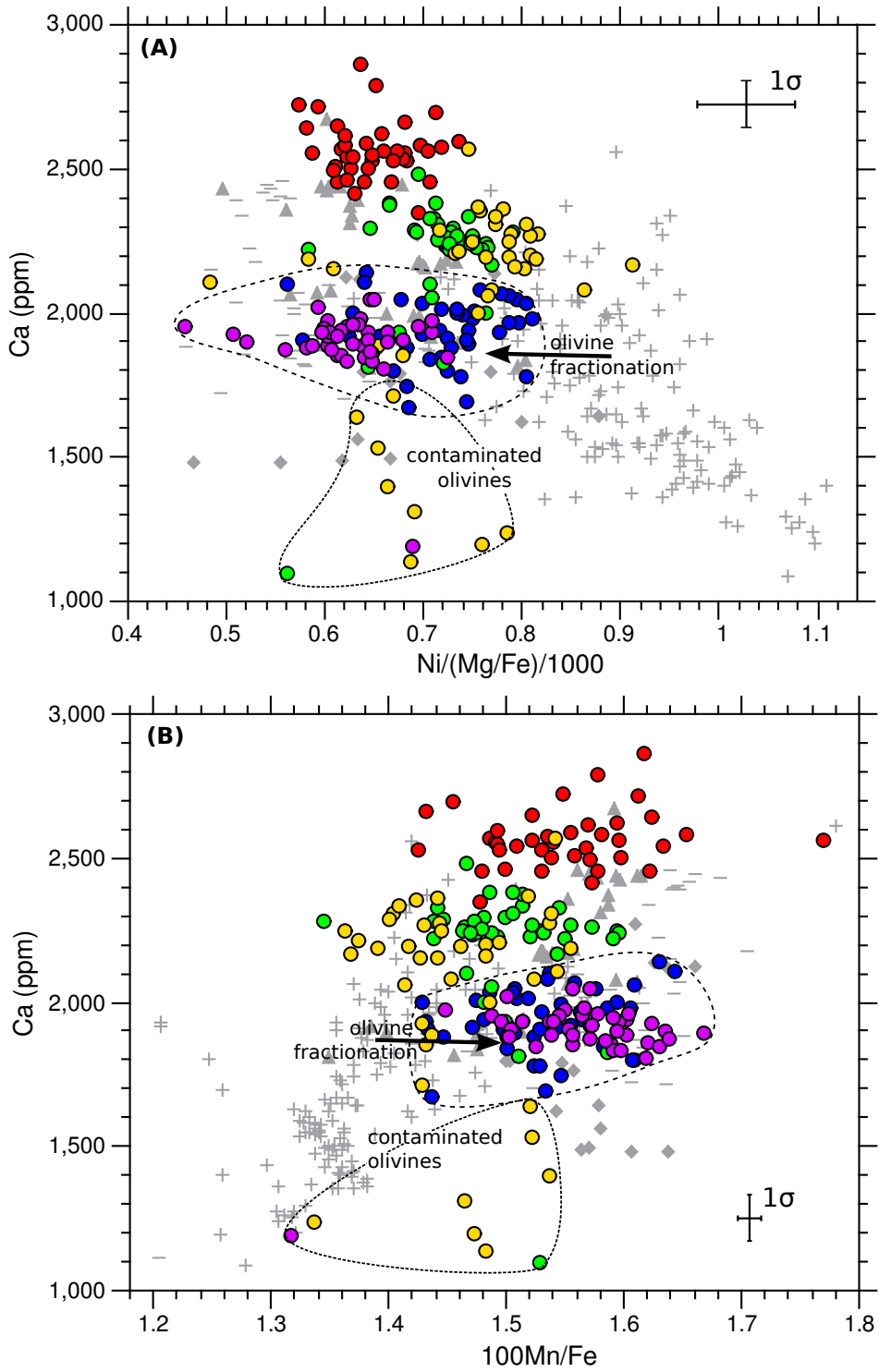


Figure 4.7: (A) Ca vs Ni/(Mg/Fe)/1000. More primitive eruptions show a negative correlation with olivines lying along the array demarcated by the global data. The vector for olivine fractionation is shown. This causes olivines from Hreggnasi and Stapafell to be offset to lower Ni/(Mg/Fe). (B) Ca vs 100Mn/Fe. For the more primitive eruptions there is a positive correlation with olivines lying along the global array. Olivines from Hreggnasi and Stapafell are offset to higher Mn/Fe for given Ca concentration.

These trends in magma composition are produced by a combination of source and melting process effects. Without clues from isotope data it is difficult to deconvolve these two effects. The potential roles of source mineralogy and the fractional melting process will be discussed later. Additional to mantle source effects and fractional crystallisation some of the variability observed may be due to shallow processes such as assimilation of crustal melts or localized reaction with cumulate rocks. There is some indication of mixing in the Blafjall sample with primitive mantle melts mixing with a more evolved low Ca end-member; potentially representing crustal melts or contamination by hydrothermal alteration, although no signs of alteration were observed in hand specimen.

Rim gradients, which are identified from scanning electron microscope (SEM) images and measured by taking closely-spaced profiles, were found to be negligible in olivines from Midfell and Kistufell indicating either minimal magma mixing during their generation, or a long period of incubation for diffusional re-equilibration of the rims.

Stronger gradients are observed in olivines from Staphafell and Hreggnasi. Some Staphafell olivines show narrow normal zonation (Figures 4.8 and 4.9). The smooth variation in concentration of the different species (Mg-Fe, Ni, Ca, Mn) suggests they are produced as diffusional overprints from re-equilibration with a more evolved disequilibrium carrier liquid rather than forming by crystallisation upon cooling. The irregular resorptional margins of some of the olivines (Figure 4.8(A)) provides further evidence that these olivines were out of equilibrium. The re-equilibration has been interpreted to occur after re-entrainment from a cumulate (Thomson and MacLennan, 2012).

Hreggnasi olivines show a variety of rim gradients including normal, reverse and oscillatory zonation; consistent with a complex history of magma mixing/ assimilation. The changes in concentration are often sharp and represent overgrowths following a change in carrier melt composition. Diffusional overprinting is also evident. Examples showing the variety of rim gradients are shown in Figures 4.10-4.13.

Importantly, even in the most strongly zoned crystals, compositional gradients are restricted to the crystal rims (which are typically $<100\mu\text{m}$). The olivines have homogeneous interiors which are unaffected by diffusion and can thus be assumed to record the composition of the magmas from which they were initially crystallised. This could be verified by measuring the composition of melt inclusions to check they are in equilibrium with the olivine.

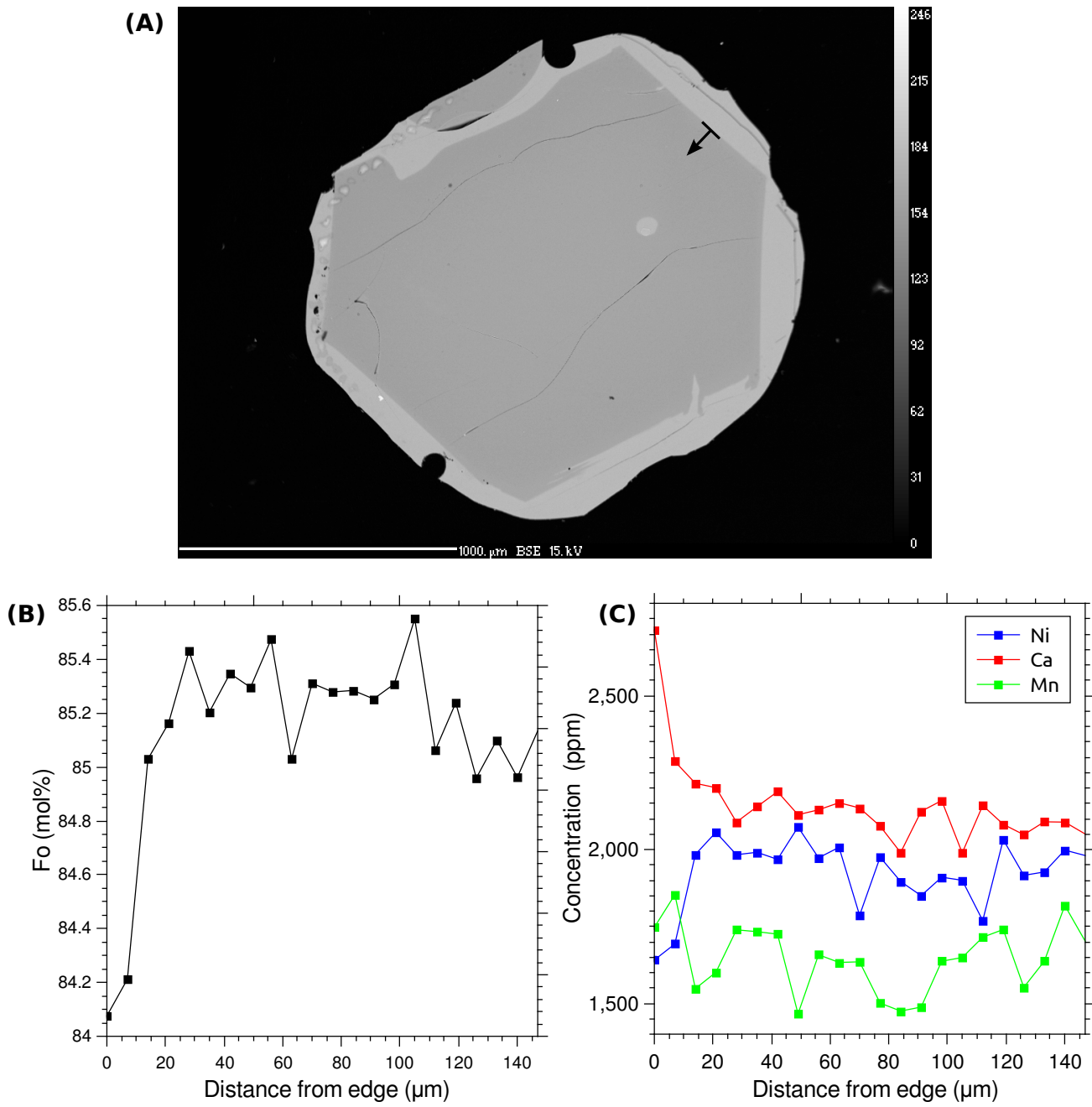


Figure 4.8: (A) A density map, obtained by SEM, of an olivine phenocryst (STAP2013-01GA-ol7) from Stapafell. The olivine shows a uniform forsterite composition. It has sharp crystal faces and at the bottom-right of the crystal dendritic growths typical of Stapafell olivines are observed. (B) Variation in Fo along the profile marked by the arrow in (A) demonstrating a uniform core and a narrow rim, 20 μm, of more evolved material. (C) Variation in Ni, Ca and Mn measured along the same profile showing an increase in Ca and decrease in Ni within the narrow rim. The rim gradients are interpreted as being a result of diffusional re-equilibration of the olivine with a more evolved carrier liquid.

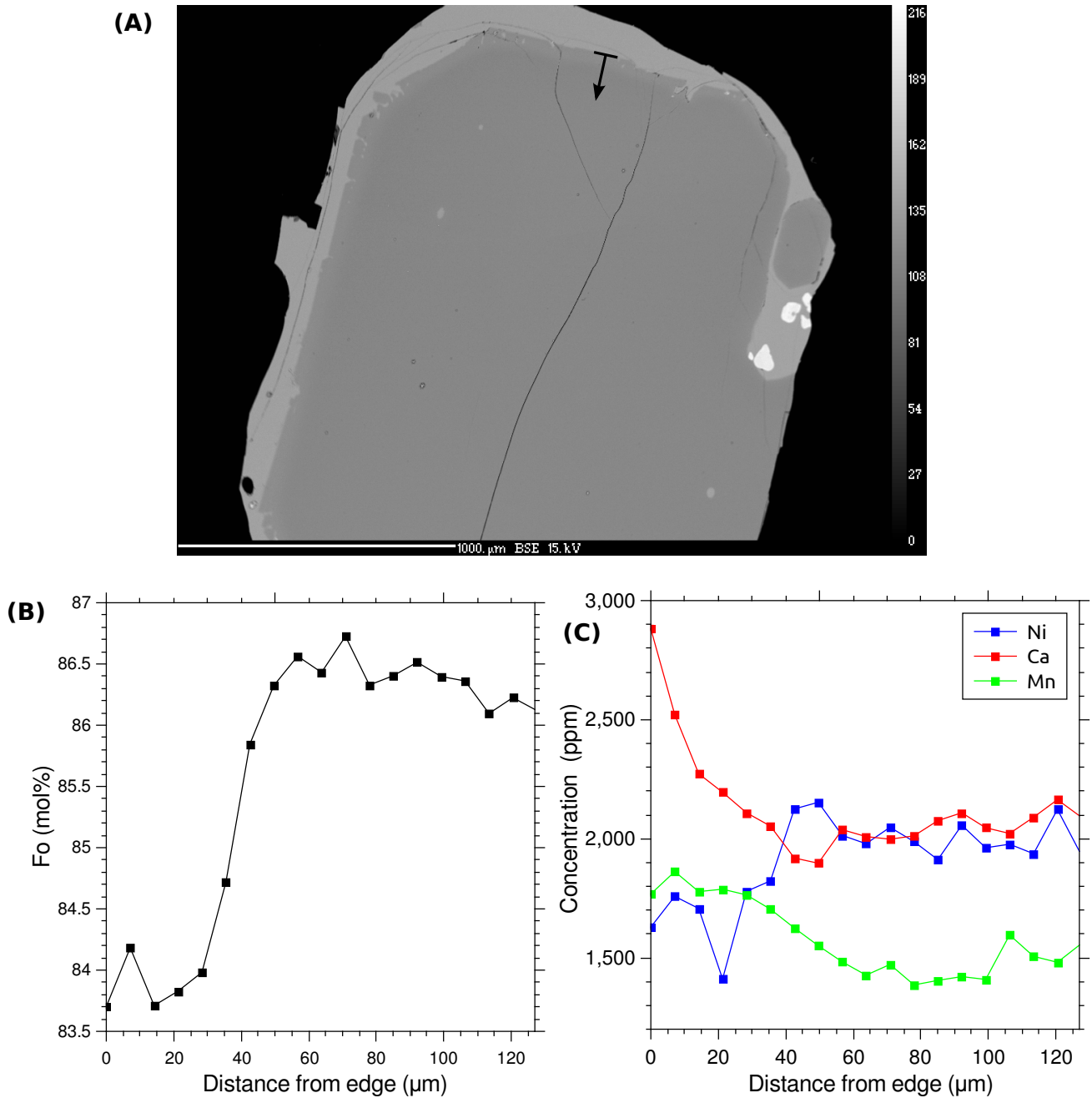


Figure 4.9: (A) A density map, obtained by SEM, of an olivine phenocryst (STAP2013-01GA-ol18) from Stapafell. The olivine core has a uniform forsteritic composition and a rim of more evolved material (shown by the lighter greyscale). It represents the most strongly zoned crystal from the Stapafell sample. Disequilibrium is indicated by the irregular reactive crystal margins. (B) Variation in Fo along the profile marked by the arrow in (A) demonstrating a uniform core and a narrow rim, 50 μm, of more evolved material. There is a slight increase in Fo within the outer 20 μm of the crystal suggesting a later more magnesian overgrowth (C) Variation in Ni, Ca and Mn measured along the same profile showing an increase in Ca and Mn and a decrease in Ni within the rim. The Mn and Ni record the later overgrowth of more primitive olivine within the outer 20 μm, while Ca does not. This is indicative of diffusive re-equilibration as the diffusivity of Ca in olivine is greater than Mg-Fe, Mn and Ni. The 2-stage zonation suggests a more complex history involving at least two phases of compositional change of the host liquid.

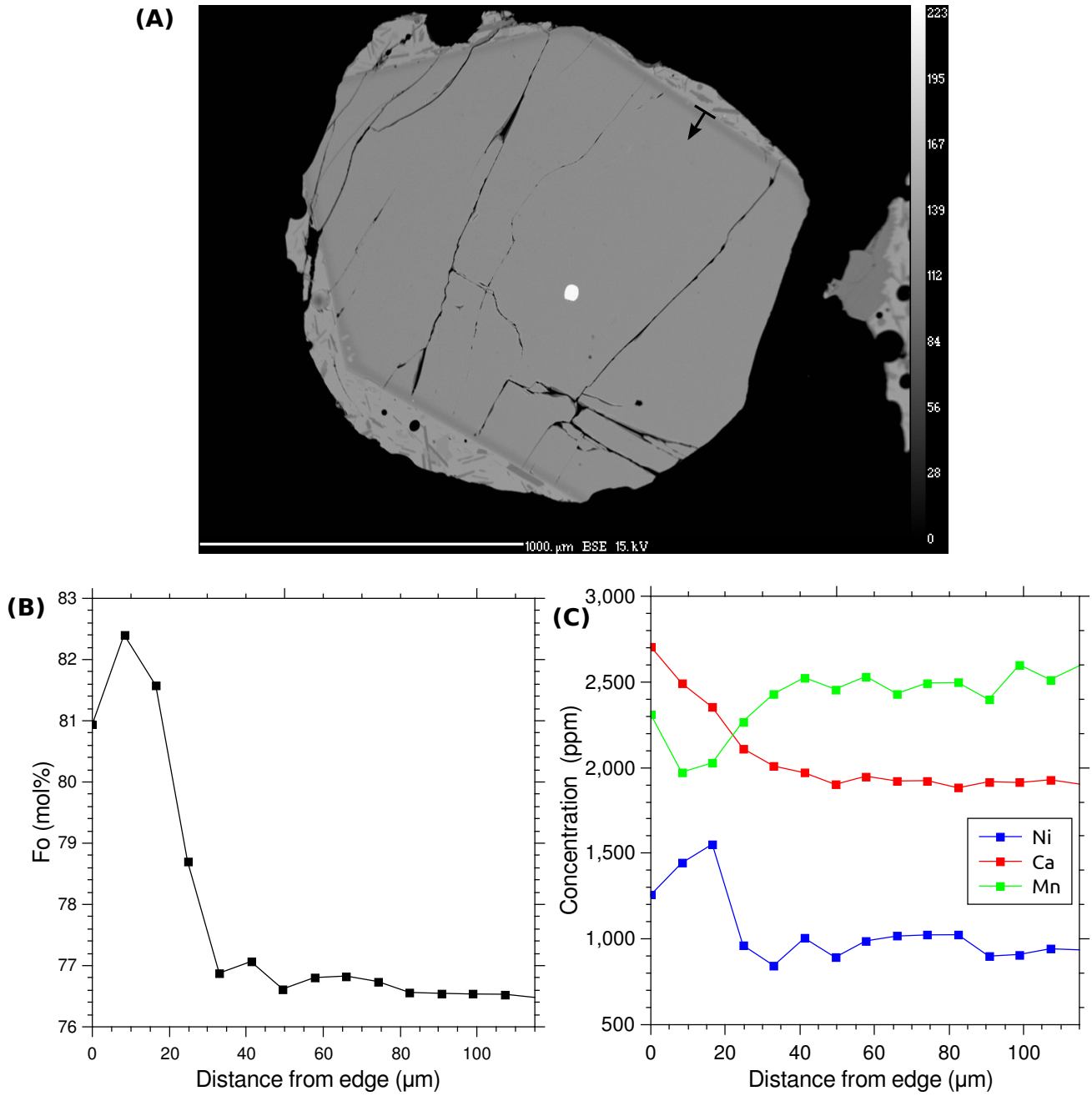


Figure 4.10: (A) A density map, obtained by SEM, of an olivine (CHRG10-5A-ol3) from Hreggnasi. The olivine has a uniform evolved core and an outer overgrowth of more forsteritic material (shown by the darker greyscale). (B) Variation in Fo along the profile marked by the arrow in (A) demonstrating a uniform core and a narrow rim, 30 μm , of more magnesian material. There is a slight decrease in Fo within the peripheral 20 μm of the crystal suggesting some late-stage re-equilibration with a more evolved carrier liquid (C) Variation in Ni, Ca and Mn measured along the same profile. A correlating increase in Ni and decrease in Mn are observed in the outer 20-40 μm followed by a decrease in Ni and increase in Mn in the outermost 20 μm . Ca shows a smooth increase due to the faster rates of diffusive re-equilibration of Ca in olivine. The more forsteritic outer rim suggests either that this is an antecrust, grown in a more evolved melt, that was entrained in a more primitive melt during a magma-mixing event; or that the fractionated host melt was replenished with more primitive melt from a deeper reservoir.

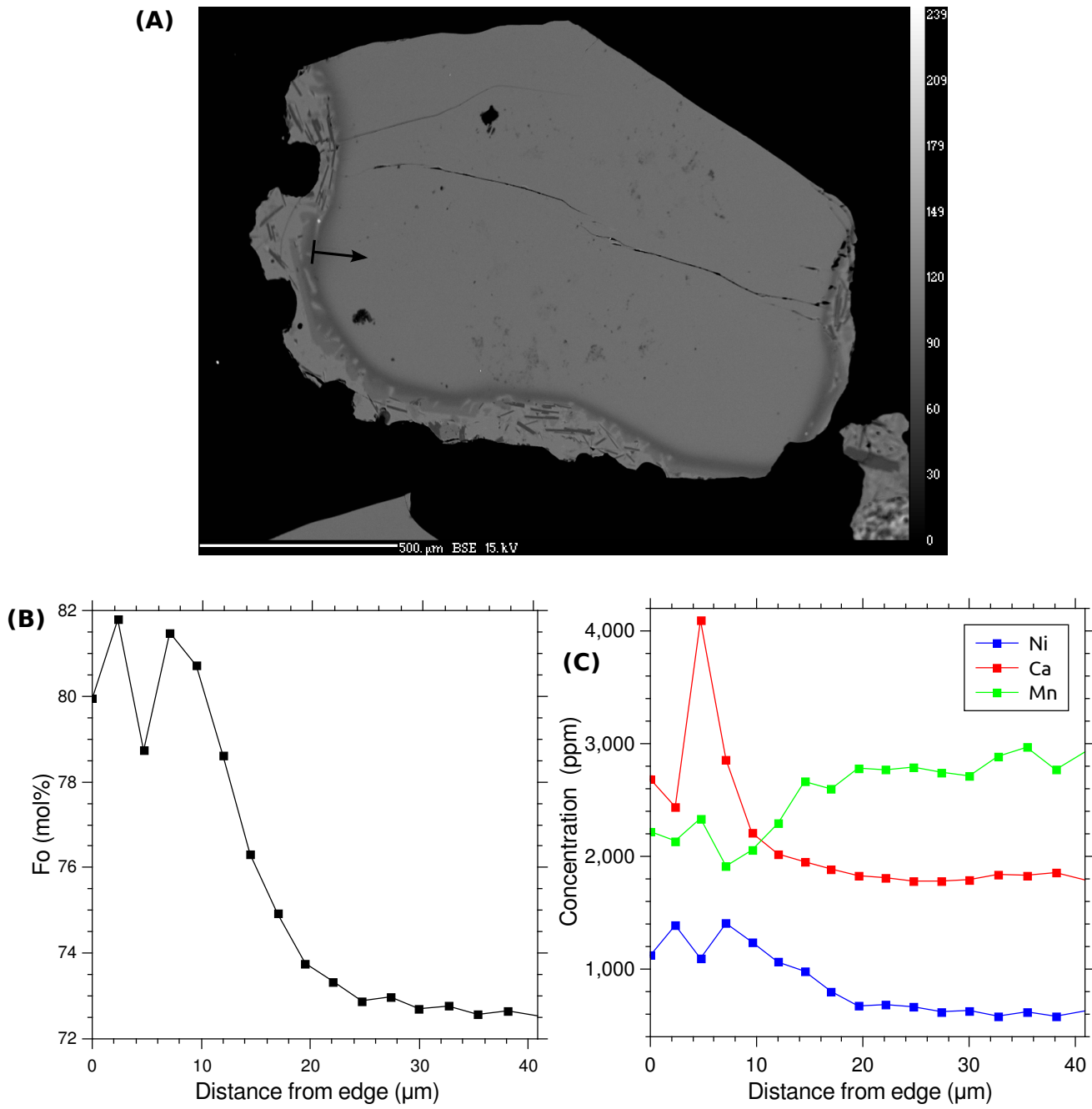
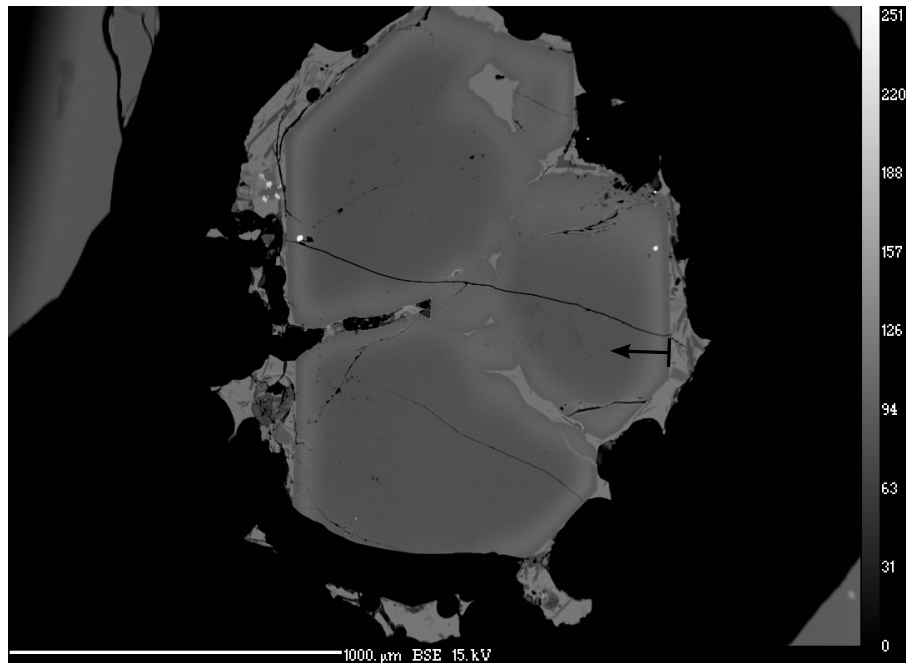


Figure 4.11: (A) A density map, obtained by SEM, of an olivine (CHRG10-5C-ol15) from Hregnasi. The olivine has a uniform evolved core and a narrow rim of more forsteritic material (shown by the darker greyscale). The rounded crystal shape and irregular reactive margin suggests that the olivine is out of equilibrium with the host glass. (B) Variation in Fo along the profile marked by the arrow in (A) demonstrating a uniform core and a narrow rim, 20 μm, of more magnesian material. (C) Variation in Ni, Ca and Mn measured along the same profile. A similar interpretation to that of the olivine in Figure 4.10.

(A)



(B)

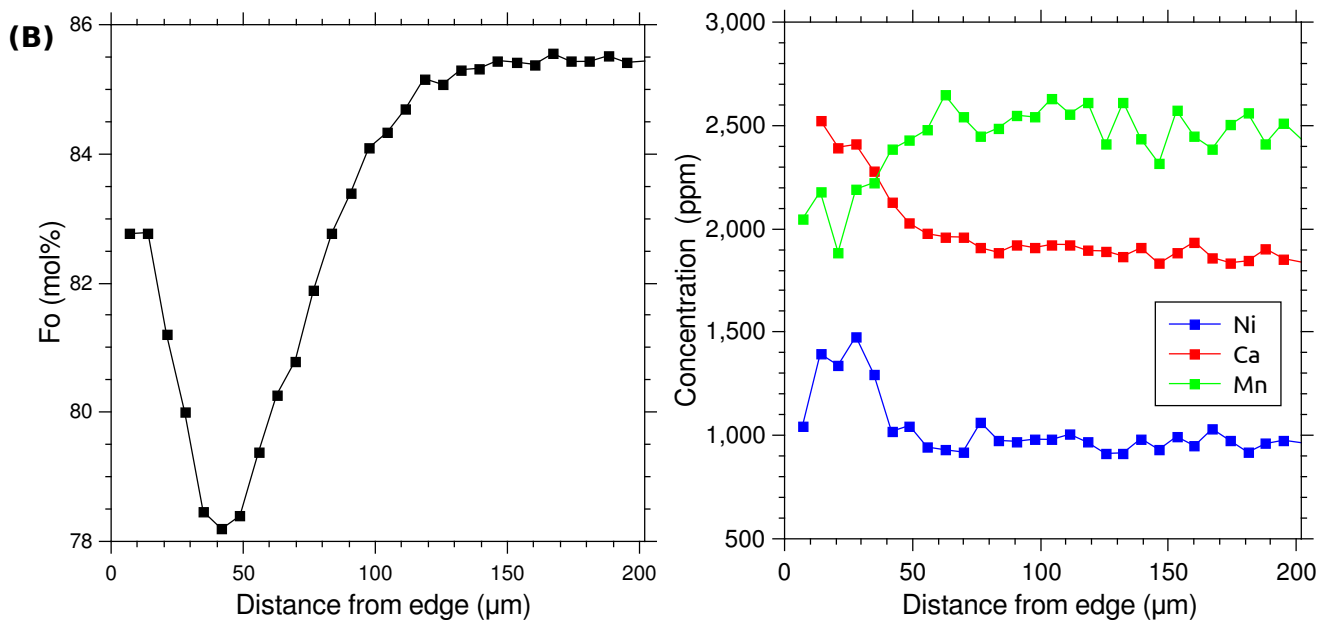


Figure 4.12: (A) A density map, obtained by SEM, of an olivine (CHRG10-5C-ol23) from Hreggnasi. The olivine has a forsteritic core and shows oscillatory zonation which switches abruptly from normal zonation to reverse zonation. Despite the glomerocrystic appearance the is a transect through a single olivine with an irregular crystal shape. (B) Variation in Fo along the profile marked by the arrow in (A) demonstrating a uniform core and a broad rim, 120 μm, containing a normal zone followed by a reverse zone. The oscillatory zonation indicates there was at least two events punctuating the olivine petrogenesis that caused the composition of the melt to change, i.e. magma mixing, magma chamber replenishment or crustal assimilation. (C) Variation in Ni, Ca and Mn measured along the same profile.

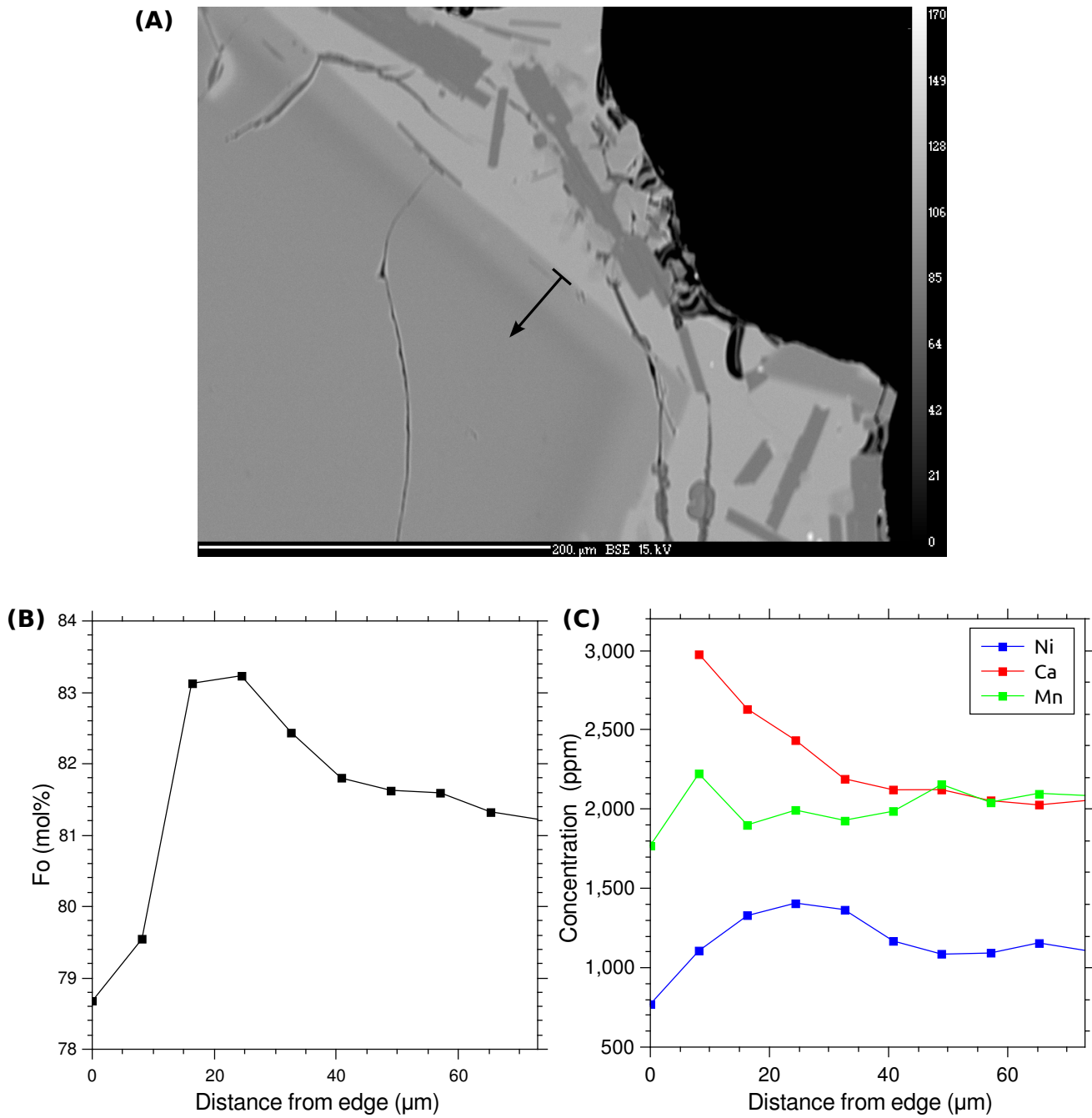


Figure 4.13: (A) A close-up density map, obtained by SEM, of an olivine (CHRG10-5D-ol29) from Hreggnasi. The olivine has a uniform core and a narrow rim within which a gradual decrease in the Fe-content is followed by a more evolved (more Fe-rich) growth zone. (B) Variation in Fo along the profile marked by the arrow in (A) demonstrating a uniform core and a narrow compositionally zoned rim, 40 μm. (C) Variation in Ni, Ca and Mn measured along the same profile. The Ni concentration mimics the variation in Fo, while Ca increases smoothly across the rim indicating a greater degree of diffusional re-equilibration of Ca.

5 Fractional Melting Model

Rather than following the full thermodynamic treatment of mantle melting as done in MELTs and pMELTs (Asimow *et al.*, 2004; Ghiorso *et al.*, 2002) the model constructed here is an empirically-based parameterisation of mantle melting. The benefits of this treatment are that it is computationally efficient and mathematically simple. This means that the effect of different parameters can easily be discerned and initial conditions varied over wide ranges applicable to mantle melting on Earth whilst stability of the model is maintained. An additional benefit is that the most up-to-date experimental partitioning data can be used.

The model describes adiabatic decompression melting of passively upwelling anhydrous peridotitic mantle and tracks the composition of melt fractions produced within the melting column. It was built from scratch on Matlab and full code is provided in appendix C. The stages of model development are outlined below.

Symbol	Definition	Units
P	Pressure	GPa
z	Depth	km
T	Temperature	°C
F	Melt fraction	wt fraction
T_p	Potential temperature	°C
t_l	Lithospheric thickness	km
$T_{cpx-out}$	Temperature at which cpx is exhausted from the solid residue	°C
$T_{solidus}$	Solidus temperature of anhydrous peridotite	°C
$T_{liquidus}$	Liquidus temperature of anhydrous peridotite	°C
$T_{lherz}^{liquidus}$	'Lherzolite liquidus'	°C
P_{sp-in}	Pressure at which sp first appears in residue	GPa
P_{gt-out}	Pressure at which gt disappears from residue	GPa
$P_{plag-in}$	Pressure at which plag first appears in residue	GPa
P_{sp-out}	Pressure at which sp disappears from residue	GPa
X_j	Modal proportion of mineral j in solid residue	wt fraction
fw_j	Formula mass of phase j	$gmol^{-1}$
n_j	Melting reaction coefficient of phase j	mol
p_j	Reaction coefficient of phase j during subsolidus phase transition	mol
c_i^j	Instantaneous concentration of species i in phase j	wt fraction
C_i^j	Point average concentration of species i in phase j	wt fraction
ζ_i^j	Point and depth average concentration of species i in phase j	wt fraction
$K_{D_{Fe^{2+}-Mg}}^{ol/L}$	Exchange coefficient for Fe^{2+} and Mg between olivine and melt	
x_i^j	Instantaneous molar concentration of species i in phase j	mol fraction
Fo	Forsterite content of olivine. Defined as $\frac{100x_{MgO}^{ol}}{x_{MgO}^{ol} + x_{Fe^{2+}O}^{ol}}$	mol %
$D_i^{j/L}$	Solid-liquid partition coefficient of trace element i in phase j	
D_i	Bulk solid-liquid partition coefficient of a trace element i	
Q_i	Bulk distribution coefficient of trace element i in the liquid modified by the formation of new phases	

Table 3: Notation

5.1 Melting Path

First, melt fraction is parameterised as a function of temperature and pressure. The approach followed is that of Katz *et al.* [2003].

The anhydrous peridotite solidus and liquidus are parameterised as second-order polynomials fit to experimental data. As well as the ‘true liquidus’ a ‘lherzolite liquidus’ is also introduced as a means for creating a kinked melting function at cpx-out. It can be conceptualised as the temperature the liquidus would have if cpx remained in the residue (Katz *et al.*, 2003). Prior to exhaustion of cpx F is expressed as a power-law of the fractional distance in temperature between the solidus and the lherzolite liquidus (equation 5.1), while after exhaustion of cpx, it is a function of the fractional distance between $T_{cpx-out}$ and the true liquidus (equation 5.2).

The kinking of the melting function at cpx-out reflects the discontinuous decrease in productivity at this point. The effect of phase exhaustion on productivity is only considered for cpx despite exhaustion of the aluminous phase also being expected under normal melting conditions (Walter, 1998).

For $F < F_{cpx-out}$:

$$F = \left(\frac{T - T_{solidus}(P)}{T_{lherz}^{liquidus}(P) - T_{solidus}(P)} \right)^{\beta_1} \quad (5.1)$$

For $F > F_{cpx-out}$:

$$F = F_{cpx-out} + (1 - F_{cpx-out}) \left[\frac{T - T_{cpx-out}}{T_{liquidus} - T_{cpx-out}} \right]^{\beta_2} \quad (5.2)$$

Where β_1 and β_2 are constants whose values are given in Katz *et al.* [2003].

To simplify the model, only anhydrous melting is considered. This approximation is valid for a number of reasons:

1. depleted upper mantle contains very little water. Its H_2O content has been estimated at 270 ± 20 ppm (Bell and Rossman, 1992);
2. The presence of small amounts of volatiles would act to increase the depth of the solidus and liquidus permitting melting to occur at greater depth. However due to the incompatibility of water during melting, the residue is quickly stripped of all its water causing melting to proceed anhydrously after only a very small degree of melting;
3. In the mid-ocean ridge setting, such as at Iceland, the mantle upwells to shallow depths and large degrees of melting are attained. Thus the small degree of hydrous melting is volumetrically negligible. It follows that in intraplate setting where melting is restricted to occurring at great depths, the role of hydrous melting becomes more important and the assumption of anhydrous melting less valid.

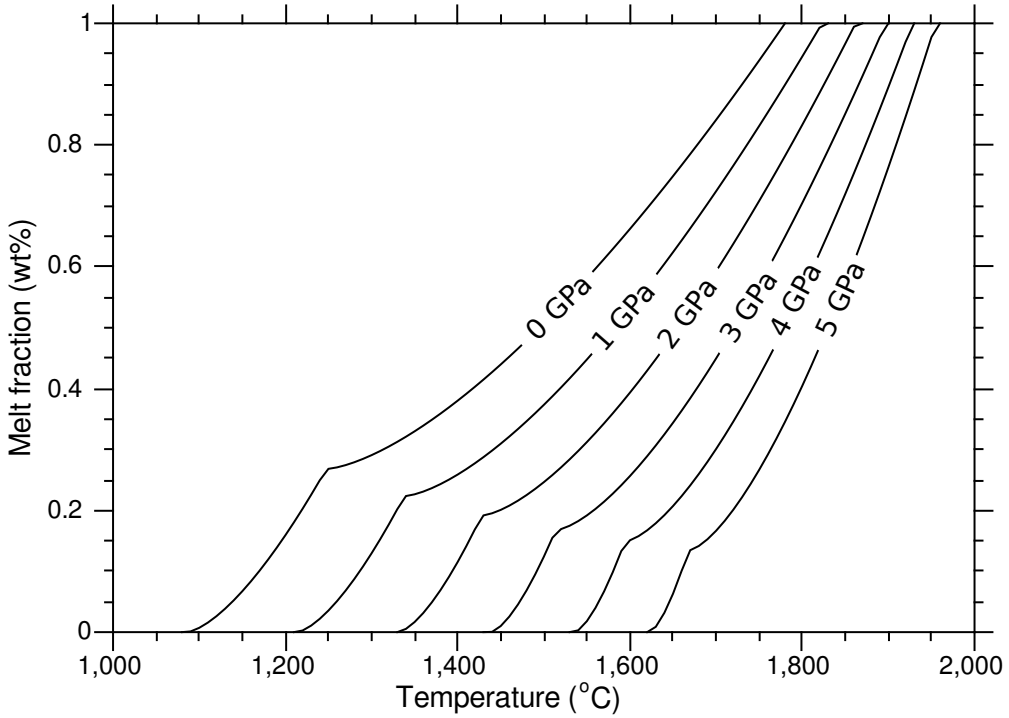


Figure 5.1: Isobaric anhydrous peridotite melting curves at different pressures. Curves are concave upward as a result of the condition that isobaric productivity ($\frac{dF}{dT}$) increases with increasing temperature: $\frac{dF}{dT} > 0$ and $\frac{d^2F}{dT^2} > 0$. The kink occurs at $F_{cpx-out}$ due to a discontinuous decrease in productivity when cpx is exhausted from the residue. Curves calculated for an initial modal cpx of 10 wt%.

The parameterisation of $F(P,T,X_{\text{Cpx}})$ is applied to adiabatic decompression melting. Mantle decompression can occur either by passive upwelling in response to plate separation at mid-ocean ridges or by buoyant upwelling in hot mantle plumes. In both cases the variation of F and T with depth are described by equations 5.3 and 5.4 which are from McKenzie [1984]. These are solved by numerical integration using a 4th order Runge Kutta scheme.

$$\frac{dF}{dP}|_s = \frac{-\frac{c_p}{T} \frac{\partial T}{\partial P}|_F + F \frac{\alpha_f}{\rho_f} + (1 - F) \frac{\alpha_s}{\rho_s}}{\Delta S + \frac{c_p}{T} \frac{\partial T}{\partial F}|_P} \quad (5.3)$$

$$\frac{dT}{dP}|_s = T \left(\frac{F \frac{\alpha_f}{\rho_f} + (1 - F) \frac{\alpha_s}{\rho_s} - \Delta S \frac{dF}{dP}|_s}{c_p} \right) \quad (5.4)$$

Melting is initiated at the pressure at which the mantle adiabat intersects the solidus. The T-P gradient of adiabatically upwelling mantle derived by Phipps Morgan [2001] is given by:

$$\frac{dT}{dP} = \frac{-\frac{\partial S}{\partial P}|_T}{\frac{\partial S}{\partial T}|_P} = \frac{\alpha/\rho}{c_p/T} \quad (5.5)$$

A numerical solver is used to find the solidus-adiabat intersection.

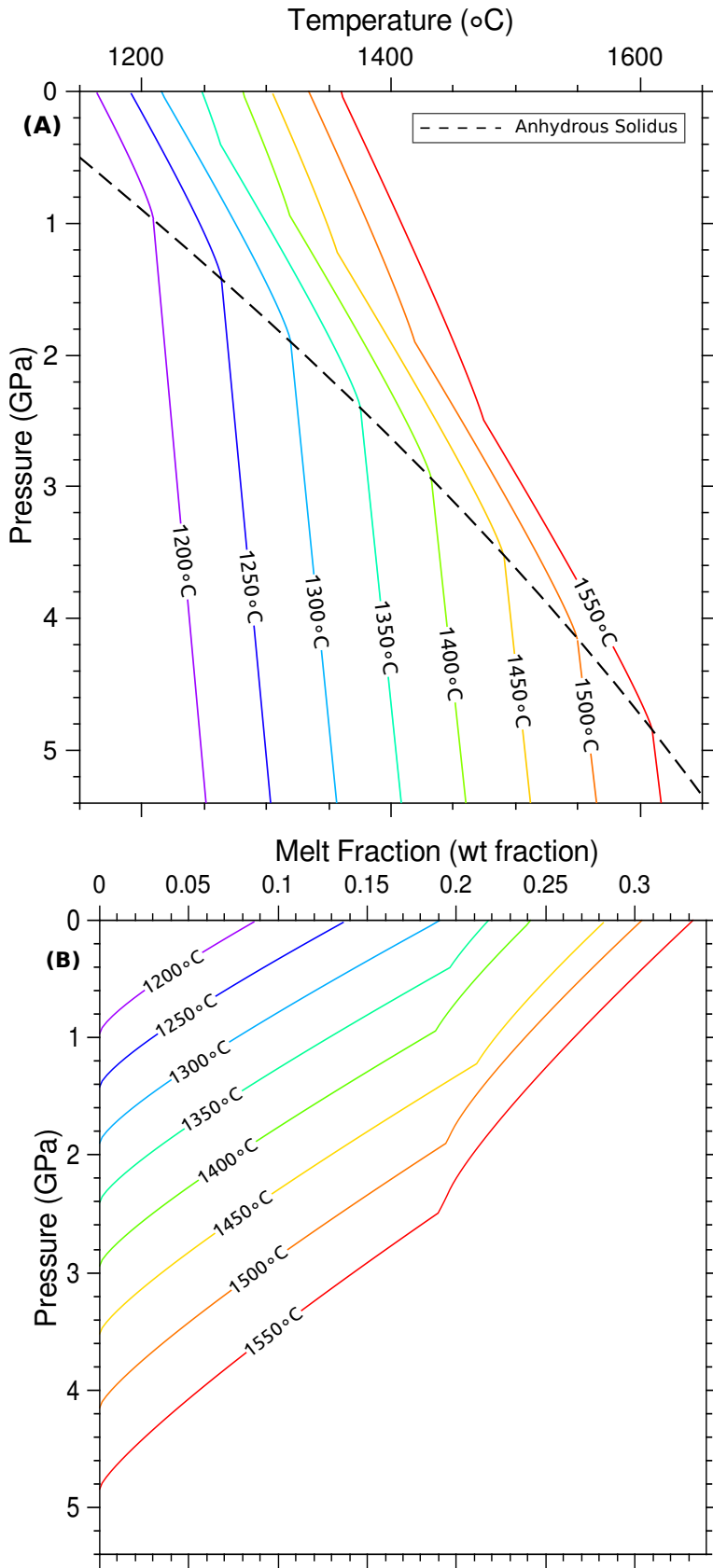


Figure 5.2: Melting paths for adiabatic upwelling mantle at a range of mantle potential temperatures obtained by numerical integration of equations 5.3 and 5.4. Calculated for anhydrous peridotitic mantle with modal cpx of 10 wt%. Kinks in the curves occur at cpx-out

5.2 Modal mineralogy of residue

To generate the residual modal mineralogy with depth, an initial mineralogy of the unmelted peridotite must be input into the model. This is then passed through the subsolidus and melting reactions to calculate the mineralogy of the solid residue. The chosen mineralogy must be consistent with general expectations of the composition of the upper mantle and be representative of the compositions used in the peridotite melting studies used to constrain parameters included later in the model. The upper mantle (DMM) is thought to have a pyrolytic composition corresponding to a fertile lherzolite (e.g. KLB-1, Takahashi, 1986; KR4003, Walter, 1998; DMM1, Wasylenki *et al.*, 2003). The mineralogy reported by Workman and Hart [2005] is used as a median estimate of ‘typical’ DMM. Variable depletion by partial melting to produce basaltic melts or variable enrichment by metasomatism means the mineralogy of the mantle may vary on a range of lengthscales. To account for this, a range of initial mineralogies are considered ranging from a fertile lherzolite, typified by KR4003 (Walter, 1998), to a depleted harzburgite, typified by 84-402 (Eggins *et al.*, 1998).

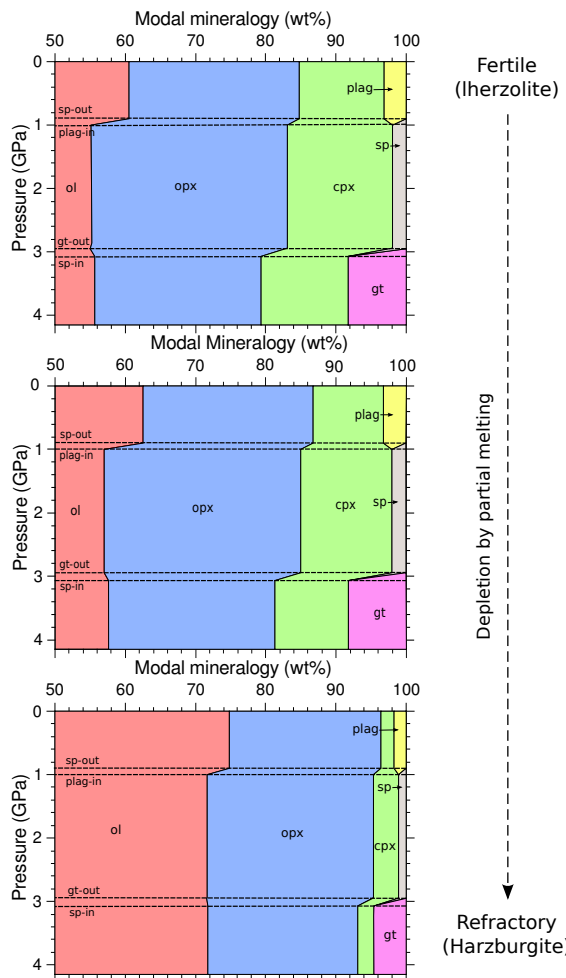


Figure 5.3: Variation in modal mineralogy of unmelted peridotite with depth for $T_p=1500^\circ\text{C}$ for three different starting mineralogies: KR4003 (Walter, 1998); DMM (Workman and Hart [2005]); 84-402 (Eggins *et al.*, 1998).

The change in mineralogy accompanying the aluminous phase changes is then considered. The garnet-spinel transition is given by:

$$2.84ol + 4.31gt = 3.96opx + 2.31cpx + 2.81sp \quad (5.6)$$

The spinel-plagioclase transition is represented by:

$$4.53opx + 3.23cpx + 2.81sp = 6.40ol + 2.48plag \quad (5.7)$$

The pressure and temperature of the subsolidus reactions are parameterised. For the garnet-spinel transition the results for fertile peridotite close to the depleted peridotite solidus from Robinson and Wood [1998] are used. The pressure of the transition is slightly higher than that used in many other studies which often use results from lower temperature studies. The effect of this is discussed in section 6.1 For the spinel-plagioclase transition the experimental results of Borghini *et al.* [2009] are used. Both transitions have small positive gradients in P-T space and occur over a finite pressure range of between 0.1-0.2GPa. The pressure of the reactions are given by:

$$P_{sp-in} = 0.00175T + 0.435 \quad (5.8)$$

$$P_{gt-out} = 0.00175T + 0.313 \quad (5.9)$$

$$P_{plag-in} = 0.0005T + 0.25 \quad (5.10)$$

$$P_{sp-out} = 0.0005T + 0.15 \quad (5.11)$$

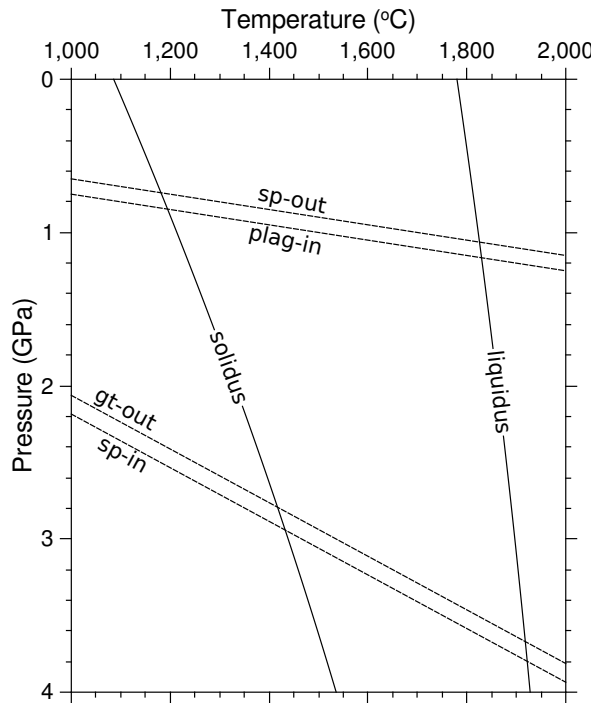


Figure 5.4: P-T graph showing the subsolidus aluminous phase transitions and their relation to the anhydrous solidus and liquidus.

Melting reaction coefficients are obtained from various experimental studies. Reactions change once minerals such as cpx or the aluminous phase are exhausted from the residue. The reaction coefficients used are given in Table 4. During lherzolite melting cpx is the main phase contributing to the melt while after cpx has been exhausted opx is the main melting phase. The dramatic switch in melting reaction at cpx-out is responsible for the discontinuous decrease in isobaric productivity at this point.

	Reaction	Reference
Garnet-field		
gt- and cpx-out	$0.083\text{ol}+0.810\text{cpx}+0.298\text{gt}=0.190\text{opx}+1\text{melt}$	
gt-out	$0.13\text{ol}+0.62\text{opx}+0.25\text{gt}=1\text{melt}$	
cpx-out	$0.094\text{ol}+1.469\text{cpx}=0.563\text{opx}+1\text{melt}$	Walter, 1998
opx-out	$0.03\text{ol}+0.97\text{opx}=1\text{melt}$	
Spinel-field		
sp- and cpx-out	$0.56\text{opx}+0.72\text{cpx}+0.04\text{sp}=0.34\text{ol}+1\text{melt}$	
sp-out	$1.06\text{opx}+0.04\text{sp}=0.10\text{ol}+1\text{melt}$	Wasylenski <i>et al.</i> , 2003
opx-out	$1.24\text{opx}=0.24\text{ol}+1\text{melt}$	
Plag-field		
plag- and cpx-out	$0.05\text{ol}+0.15\text{opx}+0.32\text{cpx}+0.48\text{plag}=1\text{melt}$	
plag-out	$0.059\text{ol}+0.376\text{cpx}+0.565\text{sp}=1\text{melt}$	Longhi, 2002
opx-out	$1.21\text{opx}=0.21\text{ol}+1\text{melt}$	

Table 4: Melt reactions in the different aluminous phase stability fields.

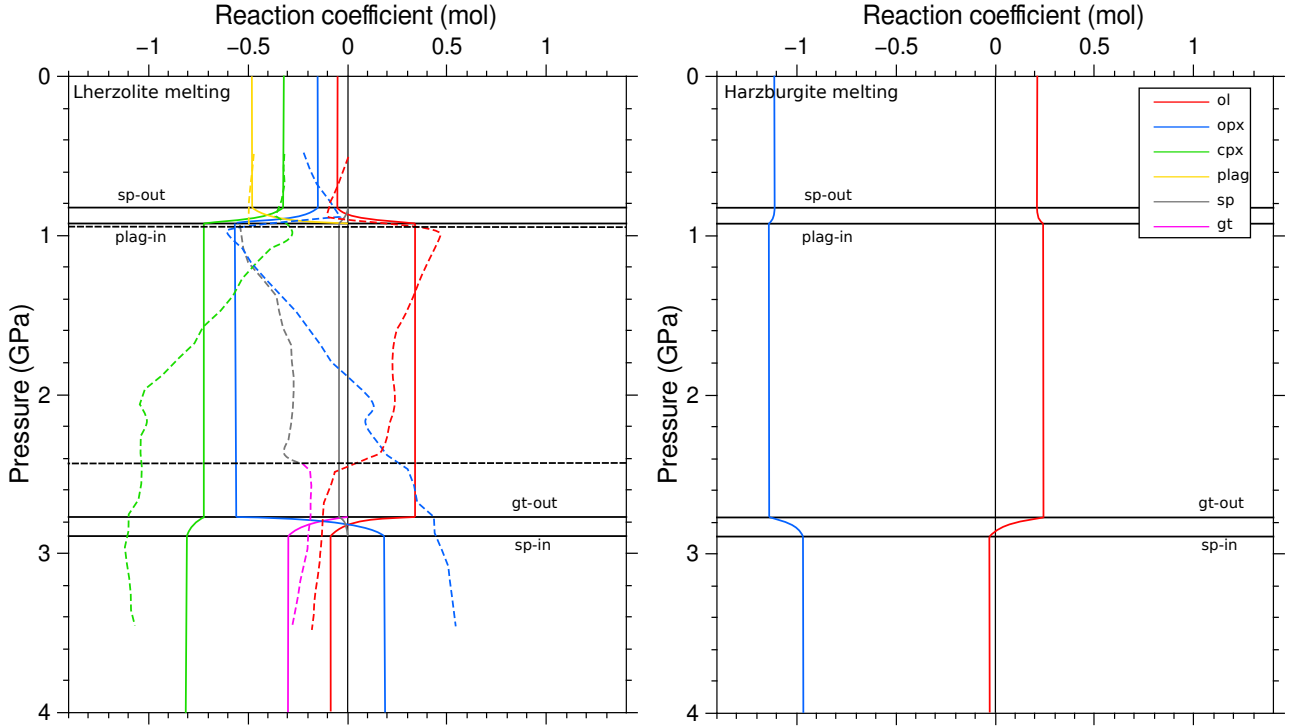


Figure 5.5: Reaction coefficients as a function of depth for lherzolite (left) and harzburgite (right) melting. Negative coefficients correspond to phases that are consumed and positive coefficients to phases that are produced during the melting reaction. Coefficients are normalised to the production of 1 mole of melt. For simplicity the coefficients are set to be constant within the aluminous phase fields. In the transition zones they are weighted according to the proportion of the respective aluminous phases present in the residue. The pressure-dependent lherzolite reaction coefficients from Longhi [2002] are shown in dashed lines for comparison.

With these reactions, the incremental melt fractions and the unmelted starting mineralogy the modal mineralogy of the residue is tracked through the melting column by applying a mass balance. The change in mineral weight fraction across each pressure increment is given by:

$$dX_j = n_j \frac{fw_j}{fw_L} dF \quad (5.12)$$

where:

$$fw_L = \sum_j fw_j n_j \quad (5.13)$$

Due to the finite pressure region over which the subsolidus transitions occur, both the subsolidus and melting reactions occur simultaneously over these intervals. Within these transition zones the melt reaction coefficients of the garnet- and spinel-field, or the spinel- and plagioclase-field reactions are weighted according to the relative proportions of the aluminous phases in the residue. For example over the gt-sp transition the melting coefficients are given by:

$$n_j = \frac{X_{gt}}{X_{gt} + X_{sp}} n_j^{gt-lherz} + \frac{X_{sp}}{X_{gt} + X_{sp}} n_j^{sp-lherz} \quad (5.14)$$

Where $n_j^{sp-lherz}$ and $n_j^{gt-lherz}$ are the melting coefficients in the sp- and gt-fields respectively. The mass balance in these regions is then given by:

$$dX_j = n_j \frac{fw_j}{fw_L} dF + p_j \frac{fw_j}{fw_{AlSi}} dX_{AlSi} \quad (5.15)$$

Where dX_{AlSi} is the incremental change in the aluminous phase that is being reacted out. The subsolidus reactions are assumed to progress linearly such that dX_{AlSi} has a constant value across the transition zone (Figure 5.6).

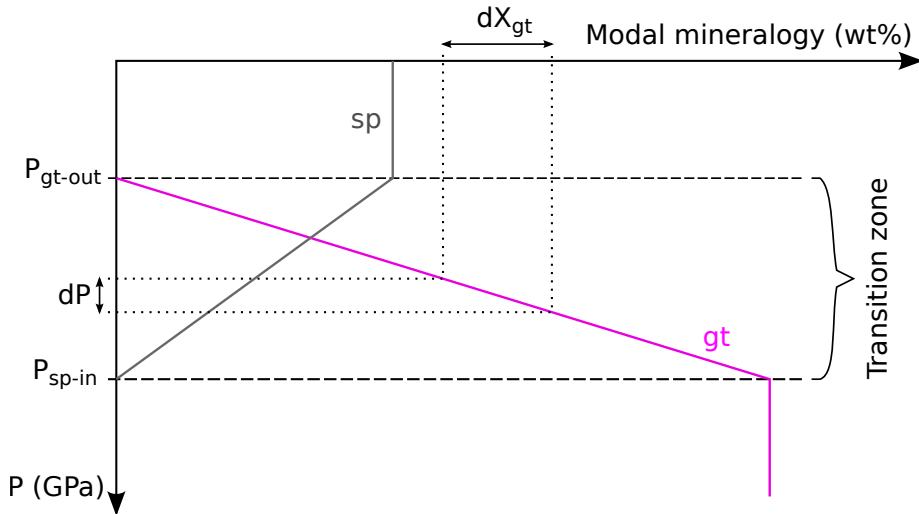


Figure 5.6: Graphical illustration showing assumed linear progress of subsolidus reaction across the divariant gt-sp transition.

5.3 Melt Composition

Melting occurs beneath mid-ocean ridges within a 2-dimensional melting region and melts erupted at the surface are a complex weighted average of the melt produced at depth. The melting path described above is for a 1-dimensional column of upwelling mantle. Within this column two different melt compositions can be defined. The instantaneous melt composition $c(F,P)$ is that of melts generated over each increment of pressure, P to $P+dP$, and melt fraction, F to $F+dF$. After weighting these incremental melts by dF they can be summed to yield an average composition generated along the melting path (McKenzie and Bickle, 1988). This composition is referred to as the point average melt composition $C(F,P)$ and is defined as:

$$C(F) = \frac{1}{F} \int_0^F c(F') dF' \quad (5.16)$$

Where the instantaneous melt composition is given by:

$$c = \frac{d}{dF}(FC) \quad (5.17)$$

The average composition of all the melt generated is termed the point and depth average ζ and depends on the weighted average of c over the whole melting region. The weighting of melts generated in the melting region is a function of both F and the mantle flow field. The mantle flow field is different in the cases of passive upwelling at mid-ocean ridges and dynamic upwelling of a mantle plume. In general the average melt composition is given by:

$$\zeta = \frac{\int_v c \left(\frac{dF}{dt} \right) dV}{\int_v \left(\frac{dF}{dt} \right) dV} \quad (5.18)$$

Where V is the melting volume and $\frac{dF}{dt}$ is the melting rate. Richardson and McKenzie [1994] described mantle flow beneath a spreading ridge using a stream function. They showed that for the special case of an isoviscous mantle, solutions of ζ for corner flow are equivalent to those for mantle upwelling with constant velocity, w , in the melting region. Taking the expression for $F(P,T,X_{cpx})$ from above, if isotherms are horizontal and mantle entering the melting region is homogeneous then F varies only as a function of depth. $\frac{dF}{dt}$ is then given by $\frac{dz}{dt} \frac{dF}{dz} = w \frac{dF}{dz}$. The solutions for passive upwelling are independent of the spreading rate and the ridge angle.

$$\zeta = \frac{\int_0^{z_0} cz \frac{dF}{dz} dz}{\int_0^{z_0} z \frac{dF}{dz} dz} \quad (5.19)$$

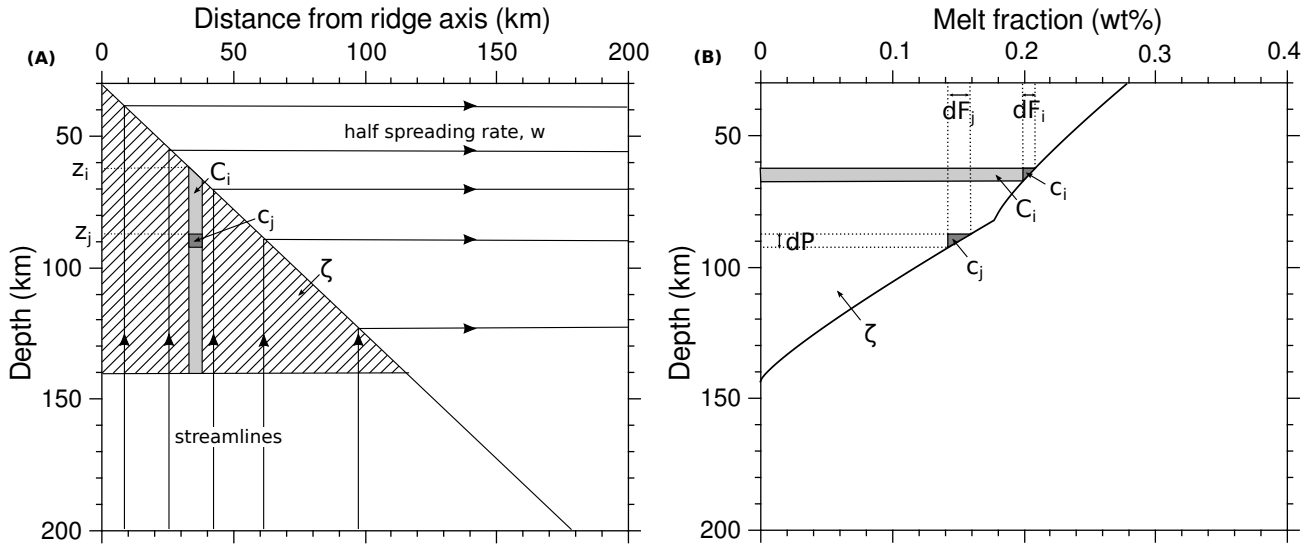


Figure 5.7: Relationship between different melt compositions in melting region beneath mid-ocean ridge. (A) Simple corner flow model for passive upwelling of an isoviscous mantle used in this model. The vertical velocity has a constant value of w within the melting region and is zero everywhere else. The hatched area represents the melting region for a mantle potential temperature of 1400°C . Only half of the geometry is shown as the flow is symmetrical about the ridge axis. (B) $F(z)$ for adiabatic decompression melting of a mantle with potential temperature of 1400°C .

This model of average melt composition is not applicable to active upwelling in mantle plumes. Iceland represents the surface expression of a mantle plume that is spatially coincident with an ocean ridge. Isotherms are therefore not expected to be horizontal and one cannot assume mantle flow velocity to be constant throughout the melting region. Models of Ito *et al.* [1996] and MacLennan *et al.* [2001] reveal that under central Iceland melting rates in the deepest part of the melting region are 10 times higher than those for plate-driven isoviscous upwelling alone. Average melt composition will thus be weighted more strongly towards deeper fractional melts. However MacLennan *et al.* [2001] showed that at distances $> 150\text{km}$ from the plume centre melting is predominantly driven by passive upwelling, meaning that this model for ζ holds for much of Iceland.

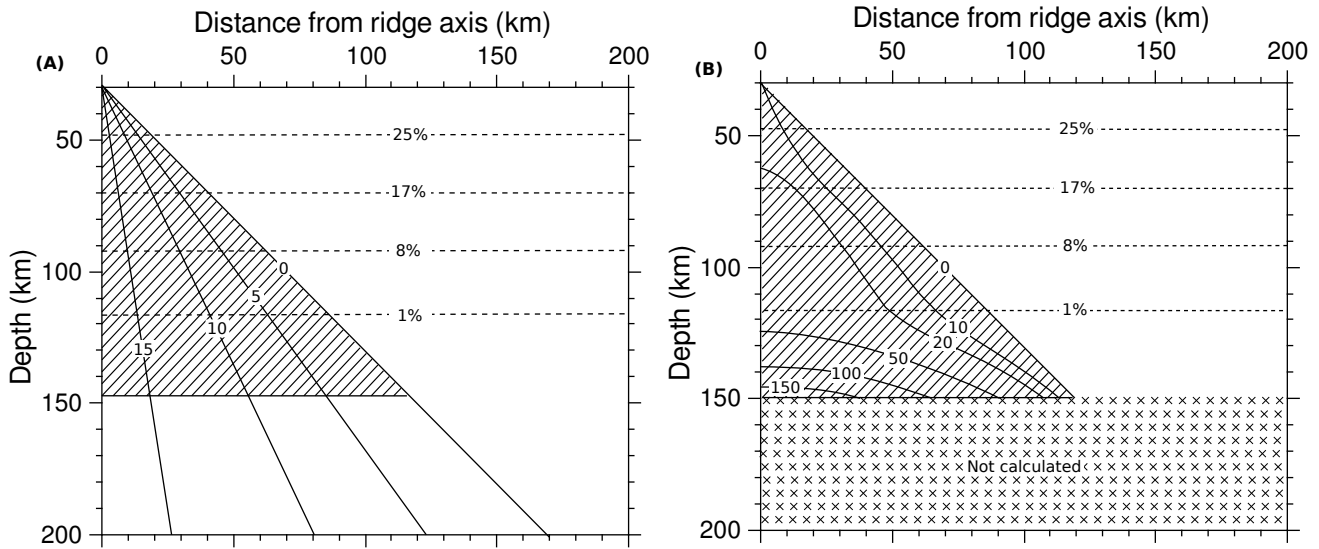


Figure 5.8: Models of mantle flow beneath ridge reproduced from MacLennan *et al.* [2001]. (A) Corner-flow model for ridge angle of 45° and full spreading rate of 18 mm yr^{-1} . Contours of vertical upwelling are shown as solid lines and marked in mm yr^{-1} . Melting region expected for mantle with $T_p = 1500^\circ\text{C}$ is hatched. Dashed lines show extent of melting in wt%. This model can be approximated by the model in figure 5.7(A). (B) Flow model for plume superimposed on ridge.

An important question to consider is which of these compositions is represented by the melts erupted at the surface. If mixing and homogenisation of melts within the melting region were complete you would expect to sample the point and depth average composition. The range in isotope and trace element ratios observed at a single locality suggest that mixing is not complete. The other extremity is that there is no mixing within the melt column. In this case a wide range of melt compositions would be sampled representing the instantaneous fractional melt compositions generated at different depths within the melting column. This too is unrealistic as mixing is suggested by the fact that trace element and isotopic compositions of melt inclusions are known to be far more variable than those of their carrier magmas (MacLennan, 2008a). This implies that there must be some degree of mixing and homogenisation of melts either during their ascent to the surface or when pooled in a crustal magma chamber. Although numerous geochemical studies qualitatively highlight the role of magma mixing, the exact extent of mixing is poorly constrained. It is therefore important to consider the maximum possible range in compositions that can be achieved by fractional melting i.e. by considering the instantaneous fractional melt compositions. Throughout the model all three melt compositions are calculated.

5.3.1 Major element melt composition

The partitioning of many FRTE is dependent on the MgO and FeO content of the melt (e.g. Beattie *et al.*, 1991; Herzberg, 2002; Matzen *et al.*, 2013). To accurately model the distributions of FRTE during mantle melting it is therefore necessary to model the major element melt composition. Unlike minor and trace elements which behave in a Henrian manner and can be described statistically using partition coefficients, major elements are the main constituents of minerals and their absolute concentrations control the phases present. Modelling their concentrations in the melt requires a full thermodynamic treatment. A simpler method is to construct a parameterisation based on experimental melting studies. The parameterisation of melt composition as a function of melt fraction and pressure of Watson and McKenzie [1991] is used in this model. This tracks the weight proportions of the major mineral-forming oxides SiO₂, TiO₂, Al₂O₃, FeO, MgO, CaO, Na₂O and K₂O. All other oxides are assumed to be of negligible concentration and their contribution is set to zero. The parameterisation is modified such that $F_{cpx-out}$ is consistent with the rest of the melting model.

The weight proportions are converted to molar concentrations and, by setting $K_{D_{Fe^{2+}-Mg}}^{ol/L}$, the forsterite content of olivine in equilibrium with the fractional melts is calculated. The ratio of Fe^{2+}/Fe^{3+} in the mantle is assumed to be 0.9.

$$K_{D_{Fe^{2+}-Mg}}^{ol/L} = \frac{x_{Fe^{2+}O}^L x_{MgO}^{ol}}{x_{Fe^{2+}O}^{ol} x_{MgO}^L} = \frac{0.9 x_{FeO}^L x_{MgO}^{ol}}{x_{FeO}^{ol} x_{MgO}^L} \quad (5.20)$$

$$Fo = \frac{100 x_{MgO}^L}{x_{MgO}^L + 0.9 K_{D_{Fe^{2+}-Mg}}^{ol/L} x_{FeO}^L} \quad (5.21)$$

The Mg and Fe concentration of the olivine is calculated using the constraint of stoichiometry by assuming Mg and Fe are the only species occupying the M1 sites.

$$x_{Mg}^{ol} = \frac{2}{3} \frac{x_{MgO}^L}{x_{MgO}^L + 0.9 K_{D_{Fe^{2+}-Mg}}^{ol/L} x_{FeO}^L} \quad (5.22)$$

$$x_{Fe}^{ol} = \frac{2}{3} \left(1 - \frac{x_{MgO}^L}{x_{MgO}^L + 0.9 K_{D_{Fe^{2+}-Mg}}^{ol/L} x_{FeO}^L} \right) \quad (5.23)$$

5.3.2 Minor element melt composition

The principle aim of this study is to model the Ni and Mn concentrations of olivines crystallized from primitive melts. A number of other FRTE minor elements were also included in the model.

The way in which trace elements partition between the solid and melt phase is described quantitatively by partition coefficients. A growing body of experimental work has gone into the determination of partition coefficients of trace elements under a range of conditions applicable to melting within the earth. Partition coefficients are in general found to be a function of temperature and melt composition with negligible pressure dependence. A common way of parameterising $D_i^{j/L}$ is to combine the temperature and melt composition dependence by expressing it in terms of $D_{Mg}^{j/L}$. $D_{Mg}^{j/L}$ is a function of the Mg and Fe content of the melt and mineral which in turn vary with F. $D_{Mg}^{ol/L}$ and $D_{Mg}^{o/L}$ are calculated using the model of Beattie [1993]:

$$D_{Mg}^{ol/L} = \frac{\frac{2}{3} - 0.027x_{Fe^{2+}}^L}{0.299x_{Fe^{2+}}^L + x_{Mg}^L} \quad (5.24)$$

$$D_{Mg}^{opx/L} = \frac{\frac{1}{2} - 0.129x_{Fe^{2+}}^L}{0.264x_{Fe^{2+}}^L + x_{Mg}^L} \quad (5.25)$$

The composition and temeprature dependence of the partition coefficients was only considered for olivine and orthopyroxene, which together account for 80-95 wt% of mantle peridotite. For the remaining phases constant partition coefficients were used. The partition coefficients used are given in Tables 5-7.

	$D_i^{ol/L}$	Reference
Fe	$0.279D_{Mg}^{ol} + 0.031$	Beattie <i>et al.</i> , 1991
Ca	$0.0056D_{Mg}^{ol} + 0.0135$	Beattie <i>et al.</i> , 1991
Sc	$0.063D_{Mg}^{ol} - 0.034$	Beattie <i>et al.</i> , 1991
Ti	0.015	Shaw, 2006
V	0.140	Davis <i>et al.</i> , 2013
Cr	$0.067D_{Mg}^{ol} + 0.183$	Herzberg, 2002
Mn	$0.214D_{Mg}^{ol} + 0.118$	Herzberg, 2002
Co	$0.786D_{Mg}^{ol} - 0.385$	Beattie <i>et al.</i> , 1991
Ni	$\ln(D_{Ni}^{molar}) = \frac{4338}{T} + 1.956 - \ln\left(\frac{x_{MgO}^L}{x_{MgSi_{0.5}O_2}^L}\right)$	Matzen <i>et al.</i> , 2013
Zn	1.04	Le Roux <i>et al.</i> , 2011

Table 5: Olivine-melt FRTE partition coefficients used in this model

	$D_i^{opx/L}$	Reference	$D_i^{cpx/L}$	Reference
Fe	$0.286D_{Mg}^{opx} + 0.059$	Beattie <i>et al.</i> , 1991	0.488	Davis <i>et al.</i> , 2013
Ca	$-0.28 + 0.1D_{Mg}^{opx} + \frac{0.55}{D_{Mg}^{opx}}$	Herzberg, 2002	0.86	Walter, 1998
Sc	$0.522D_{Mg}^{opx} - 0.66$	Beattie <i>et al.</i> , 1991	0.84	Davis <i>et al.</i> , 2013
Ti	$0.004 + 0.065D_{Mg}^{opx}$	Herzberg, 2002	0.124	Davis <i>et al.</i> , 2013
V	1.06	Davis <i>et al.</i> , 2013	1.48	Davis <i>et al.</i> , 2013
Cr	$-0.67 + 0.04D_{Mg}^{opx} + 0.753(D_{Mg}^{opx})^2$	Herzberg, 2002	7.5	Davis <i>et al.</i> , 2013
Mn	$0.14 + 0.274D_{Mg}^{opx}$	Herzberg, 2002	0.768	Davis <i>et al.</i> , 2013
Co	$0.467D_{Mg}^{opx} + 0.14$	Beattie <i>et al.</i> , 1991	0.86	Davis <i>et al.</i> , 2013
Ni	$-0.263 + 1.206D_{Mg}^{opx}$	Herzberg, 2002	4.0	Herzberg, 2002
Zn	0.451	Davis <i>et al.</i> , 2013	0.333	Davis <i>et al.</i> , 2013

Table 6: Orthopyroxene- and clinopyroxene-melt FRTE partition coefficients used in this model

	$D_i^{plag/L}$	Reference	$D_i^{sp/L}$	Reference	$D_i^{gt/L}$	Reference
Fe	0.2	Bindeman <i>et al.</i> , 1998	0.95	Davis <i>et al.</i> , 2013	0.654	Davis <i>et al.</i> , 2013
Ca	2.0	Drake and Weill, 1975	0.0036	Wasylewski <i>et al.</i> , 2003	0.46	Walter, 1998
Sc	0.0071	Phinney and Morrison, 1990	0.058	Davis <i>et al.</i> , 2013	5.96	Davis <i>et al.</i> , 2013
Ti	0.04	Shaw, 2006	0.084	Davis <i>et al.</i> , 2013	0.262	Davis <i>et al.</i> , 2013
V	0.022	Dunn and Sen, 1994	2.75	Davis <i>et al.</i> , 2013	1.84	Davis <i>et al.</i> , 2013
Cr	0.04	Shaw, 2006	188	Wasylewski <i>et al.</i> , 2003	10.2	Davis <i>et al.</i> , 2013
Mn	0.1	Dunn and Sen, 1994	0.46	Davis <i>et al.</i> , 2013	1.241	Davis <i>et al.</i> , 2013
Co	0.1	Dudas <i>et al.</i> , 1971	3.0	Davis <i>et al.</i> , 2013	0.83	Davis <i>et al.</i> , 2013
Ni	0.26	Shaw, 2006	16.0	Shaw, 2006	1.8	Shaw, 2006
Zn	0.35	Dudas <i>et al.</i> , 1971	5.2	Davis <i>et al.</i> , 2013	0.213	Davis <i>et al.</i> , 2013

Table 7: Plagioclase- spinel- and garnet-melt FRTE partition coefficients used in this model

With these values of $D^{j/L}$ and the mineralogy of the solid residue a bulk partition coefficient for each element is calculated:

$$D_i = \sum_j x^j D_i^{j/L} \quad (5.26)$$

Before calculating the trace element content of the melt the initial trace element concentration of the source is set. The major and trace element concentrations of upper mantle peridotite are constrained from mantle xenoliths carried in ultramafic magmas and from bulk Earth partitioning models. Due to variable enrichment and depletion of the mantle by partial melting and metasomatism, concentrations vary. Korenaga and Kelemen [2000] determined that bulk NiO of the depleted peridotite varies between 2500-3500ppm, corresponding to a bulk Ni of 1500-2500ppm. No such detailed study for the distribution of bulk MnO concentration is available. A range of 1100-1300ppm is used as this range covers the values reported in the literature (Workman and Hart, 2005; Davis *et al.*, 2009). This is actually a conservative estimate of the range. Lower values down to 800ppm are recorded for more depleted peridotites (Salters and Stracke, 2004). The effect of varying source concentration on the final olivine composition is discussed

in section 6.1. Estimates of the concentrations of all FRTE included in the model (excluding Fe and Ca which are included in the major element parameterisation) are given in Table 8.

Element	Median	Range
Sc	16.3	3.3-29.3
Ti	798	786-810
V	79	72-86
Cr	2500	2460-2540
Mn	1200	1100-1300
Co	106	92-120
Ni	2000	1500-2500
Zn	56	-

Table 8: FRTE concentration of upper mantle as reported by Salters and Stracke [2004] (excluding Ni and Mn). See text for references for estimates of Mn and Ni concentration.

The trace element concentration of the instantaneous fractional melt is then calculated. As melting is non-modal and often incongruent a ‘modified partition coefficient’, Q , must be introduced which accounts for the melting reaction. The expression for Q from Benito-García and López-Ruiz [1992] is used. This is included in the general expressions for fractional melting (Shaw, 2006).

$$c^L = \frac{c_0}{D_o} \left[1 - \frac{FQ}{D_0} \right]^{\left(\frac{1}{Q}-1\right)} \quad (5.27)$$

$$c^s = \frac{c_0(1-F) - c^L F}{1-F} \quad (5.28)$$

The trace element concentrations of the instantaneous melt fractions were calculated by applying this equation over each pressure increment; resetting C_0 and D_{i_0} at every step to account for changing trace element concentration and mineralogy of the solid residue.

From these instantaneous melt compositions the point average and point and depth average compositions are calculated using equations 5.16 and 5.19.

An intrinsic assumption of the fractional melting model is that there is no reequilibration of fractional melts as they travel to the surface such that they retain their original major and trace element signatures (e.g. Fitton, 2003).

5.4 Olivine crystallisation

The trace element concentration of the first olivines to crystallise from the melt is given by:

$$c^{ol} = c^L D^{ol} \quad (5.29)$$

Olivine starts to crystallise when the temperature drops below the basalt liquidus and olivine becomes saturated in the melt. The temperatures of the shallow basalt liquidus are calculated using equation 15 from Putirka [2008] assuming that olivine crystallizes at 0.2GPa ($\sim 6\text{km}$) (Matzen *et al.*, 2013) within the crust and that the melt is anhydrous with constant $x_{Na_2O}^L$ and $x_{K_2O}^L$ of 0.2 and 0.003 respectively.

$$T_{liquidus}^{basalt} = 815.3 + 265.5Fo + 15.37x_{MgO}^L + 8.61x_{FeO}^L + 6.646(x_{Na_2O}^L + x_{K_2O}^L) + 39.16P \quad (5.30)$$

These compositions represent the most primitive olivine phenocrysts to crystallise from the melts. Even when only highly magnesian basalts are sampled, a certain amount of crystal fractionation will have occurred. Olivine is the first phase to arrive on the liquidus followed by plagioclase and cpx. In all of the Icelandic samples olivine is the predominant phenocryst phase, however plagioclase phenocrysts also occur in smaller quantities in all but the Blafjall sample. It is assumed that fractionation of plagioclase has only a small affect on the melt composition and the crystal line of descent is modelled for olivine fractionation only.

Trace element concentrations of the melt and crystallising olivine are calculated using equations 5.31 and 5.32 taken from Shaw [2006].

$$c^L = c_0^L F^{(D^{ol/L}-1)} \quad (5.31)$$

$$c^{ol} = D^{ol/L} c^L \quad (5.32)$$

Where c_0^L is the trace element concentration of the melt prior to any crystallisation as calculated in equation 5.27. As when modelling fractional melting, to determine $D^{ol/L}$, the concentration of MgO and FeO in the melt must be tracked. This is done by calculating the equilibrium concentration of MgO and FeO in the olivine crystallised at each increment of crystallisation and performing a mass balance to calculate the concentration in the remaining melt.

$$c_{MgO}^L = \frac{1}{F} [c_{MgO_0}^L - c_{MgO}^{ol} (1 - F)] \quad (5.33)$$

$$c_{FeO}^L = \frac{1}{F} [c_{FeO_0}^L - c_{FeO}^{ol} (1 - F)] \quad (5.34)$$

Crystallisation is constrained to occur at the basalt liquidus as given by equation 5.30. At every increment of crystallisation the temperature of the liquidus is recalculated to match the compositional evolution of the residual melt. As olivine crystallises the residual melt becomes more evolved and the liquidus temperature decreases.

6 Fractional Melting Model Results

The results of the fractional melting model are presented in the figures below for melting at 1300°C and 1500°C .

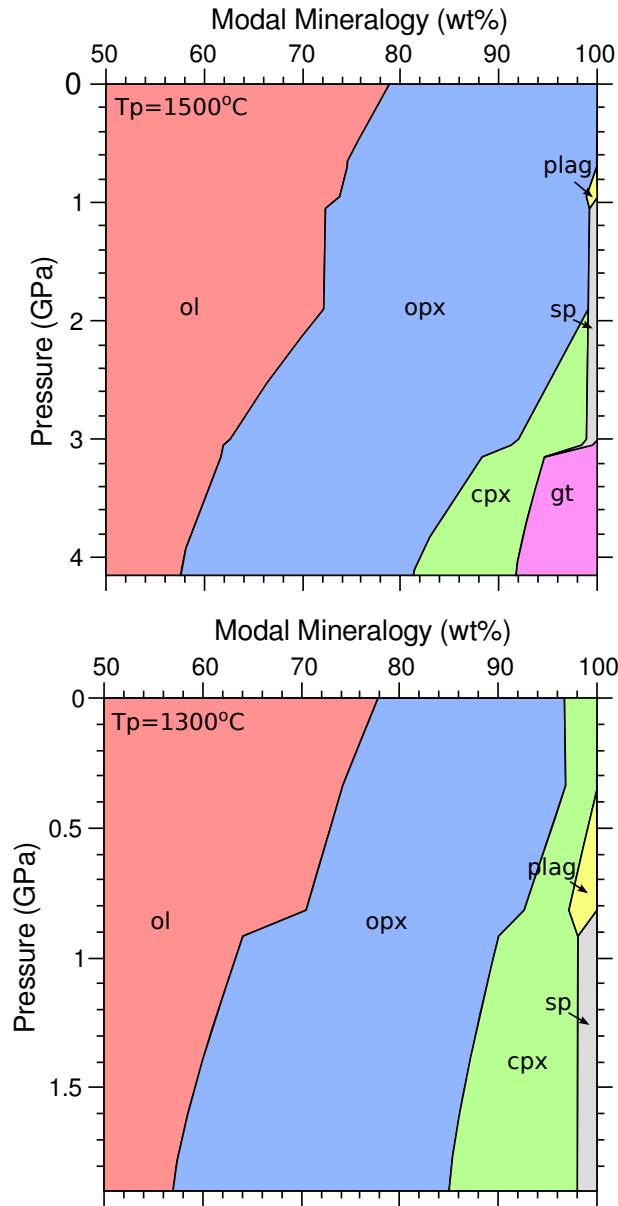


Figure 6.1: Modal mineralogy as a function of pressure within the melting column for mantle melting at a T_p of 1500°C (top) and 1300°C (bottom). The initial mineralogy of DMM from Workman and Hart [2005] was used.

Figure 6.1 shows that at elevated T_p melting starts within the garnet field. Modal cpx decreases rapidly and is exhausted at $\sim 2\text{GPa}$. The aluminous phase is preserved through the sp-field, but is promptly exhausted in the plag-field. At lower ('normal') T_p cpx is preserved in the residue, however the aluminous phase is again exhausted in the plag-field. Throughout the melting column olivine is the dominant mineral meaning all melting equilibria will be principally under olivine-control.

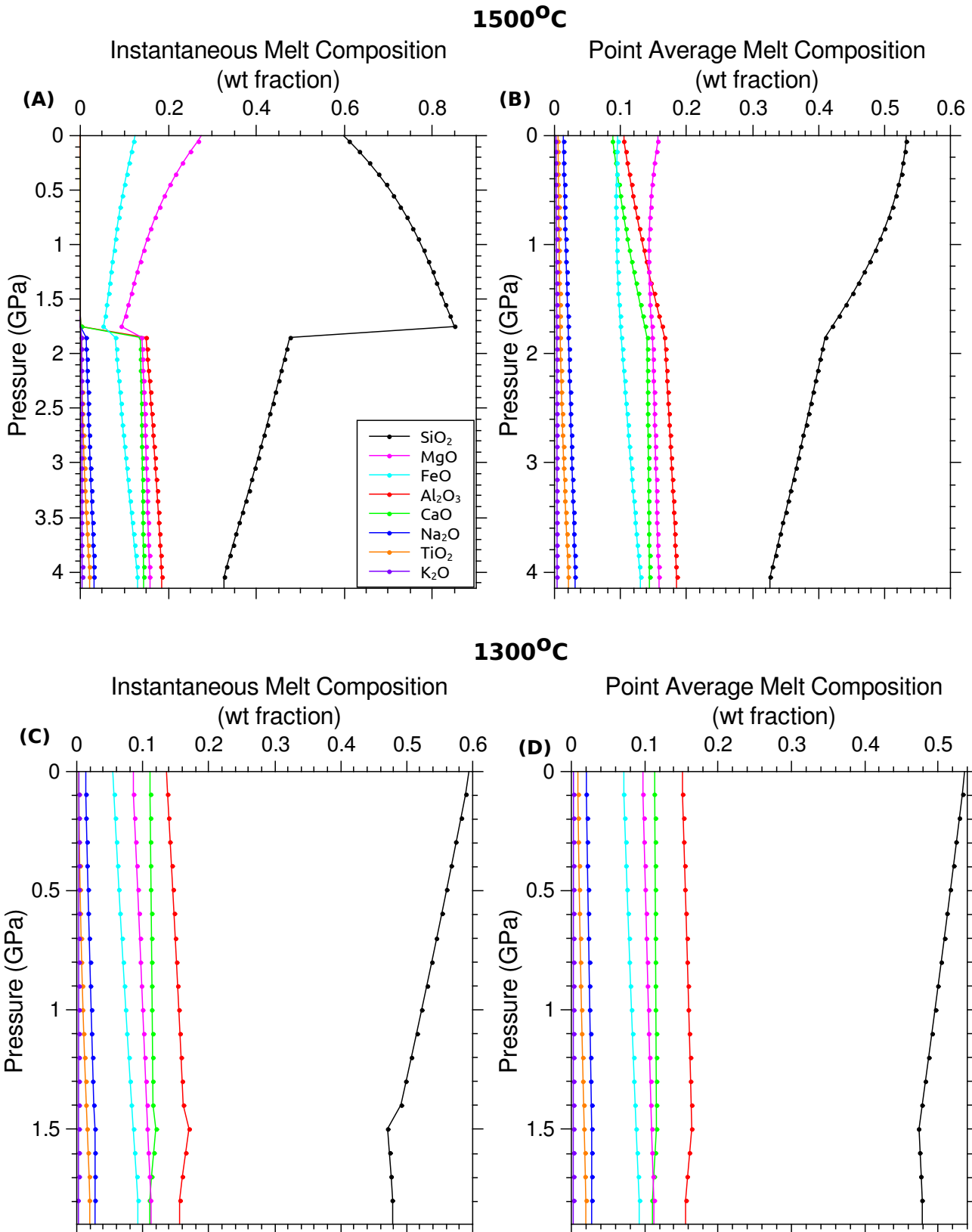


Figure 6.2: Major element melt composition as a function of pressure within the melting column for mantle melting at a T_p of 1500°C ((A) and (B)) and 1300°C ((C) and (D)). For both temperatures the instantaneous and point average melt compositions are shown. The discontinuity in (A) corresponds to cpx-out (model calculated with an initial modal cpx of 10 wt%). From this point onwards the contribution of Al_2O_3 , CaO , Na_2O , TiO_2 and K_2O to the melt is assumed to be negligible. Minimums in MgO and FeO occur at this point.

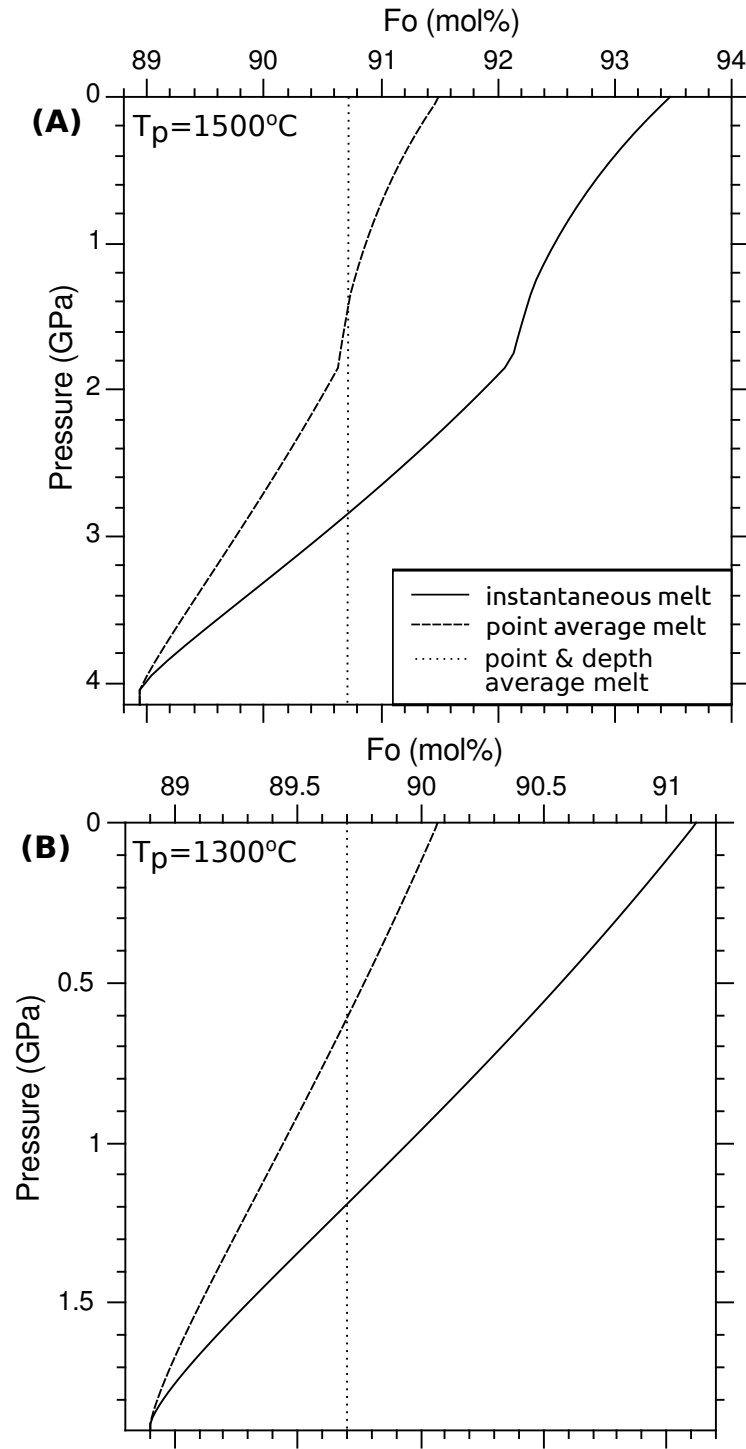


Figure 6.3: Forsterite content of olivine in equilibrium with fractional melts as a function of pressure within the melting column for mantle melting at a T_p of 1500°C (A) and 1300°C (B). The model is run with an initial modal cpx of 10 wt% and $K_{D_{Fe^{2+}-Mg}}^{ol/L} = 0.3$. Curves are shown for olivines crystallised from the aggregated fractional melts as well as the instantaneous melt fractions. Fo increases as pressure decreases and higher extents of melting are achieved.

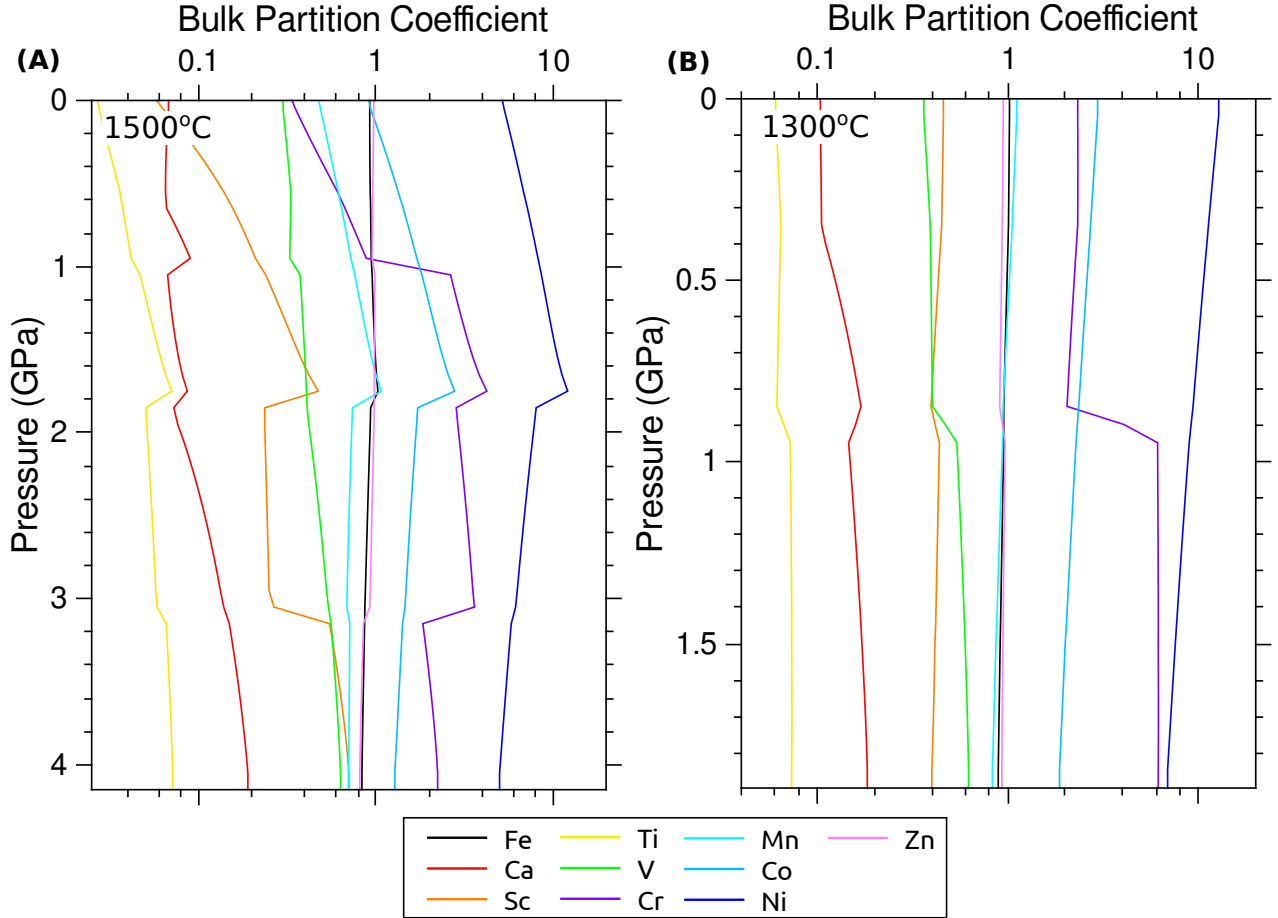


Figure 6.4: Bulk FRTE partition coefficients, D_i , as a function of pressure within the melting column for mantle melting at a T_p of 1500°C (A) and 1300°C (B). Calculated using the mineral-melt partition coefficients given in tables 5-7. The model is run with an initial modal cpx of 10 wt% and $K_{D_{Fe^{2+}-Mg}}^{ol/L} = 0.3$.

Partition coefficients are controlled by modal mineralogy of the solid residue and the melting conditions, including temperature and major element melt composition. The effect of changing mineralogy is most clearly seen at the garnet-spinel and spinel-plagioclase transitions. For trace elements including Sc and Cr the change in partition coefficient across the transitions is quite dramatic. A sharp peak in most partition coefficients coincides with the exhaustion of cpx from the residue. Rather than being due to a change in minerals contributing to the melt, this peak corresponds to minimums in x_{Mg}^L and x_{Fe}^L following exhaustion of cpx from the residue.

Although only D_{Ni} has an explicit temperature dependence (Matzen *et al.*, 2013), the partition coefficients of other FRTE including Mn vary significantly with mantle T_p . This is due both to the difference in residual mineralogy during melting (fig. 6.1) and, more importantly, the difference in melt composition at different T_p (fig. 6.2). At elevated T_p Mn behaves incompletely, but at lower T_p it becomes compatible for very shallow melting. The explicit temperature dependence of D_{Ni} causes Ni to become more compatible with decreasing T_p and for melting at shallower levels in the melting column. However following the exhaustion of cpx, melt compositional effects dominate and cause D_{Ni} to decrease. The compatibility of Ni and Mn change in opposite senses across the gt-sp transition: Ni is more compatible in the sp-field, while Mn is more compatible in the gt-field.

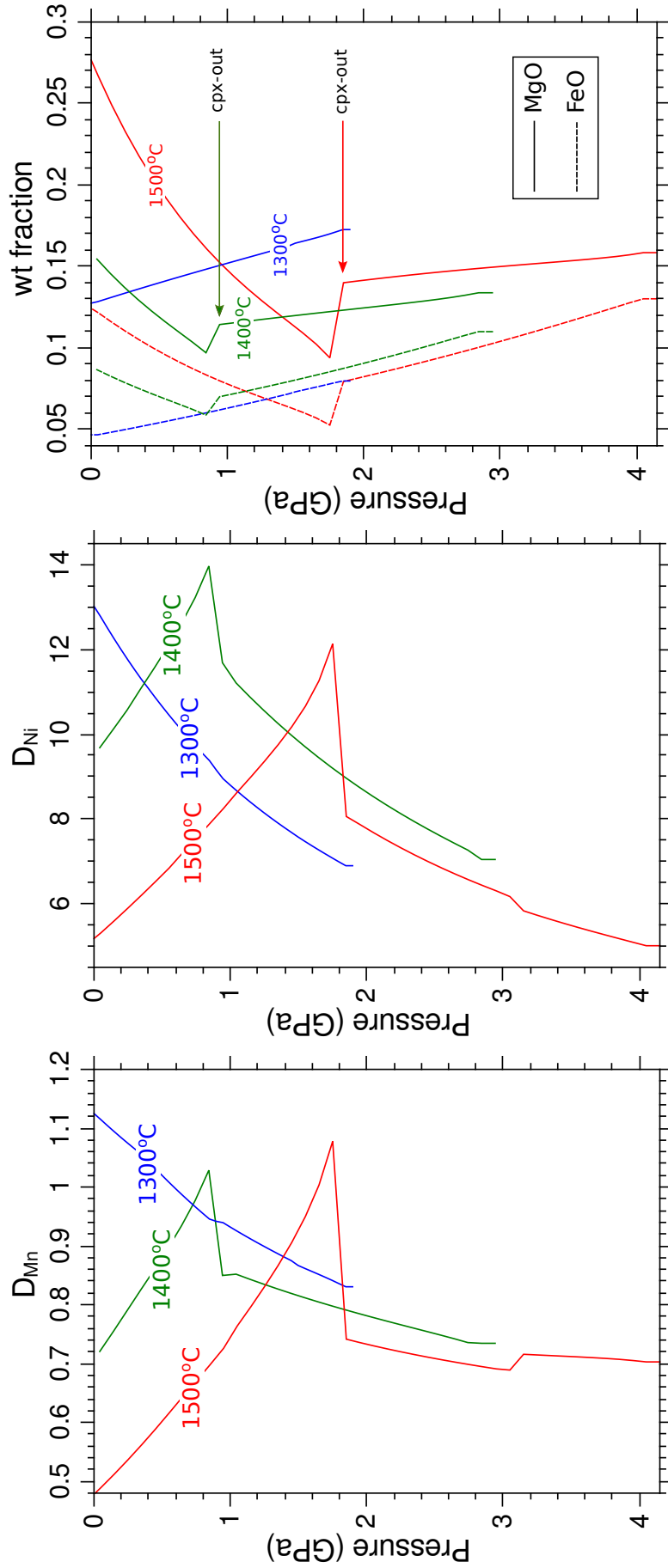


Figure 6.5: Bulk partition coefficients, D_i , for Ni and Mn for a range of mantle T_p as a function of pressure within the melting column. The model is run with an initial modal cpx of 10 wt% and $K_{D_{Fe^{2+}-Mg}}^{ol/L} = 0.3$. x_{Mg}^L and x_{Fe}^L are also plotted to demonstrate the compositional control on D_{Ni} and D_{Mn} . The peaks in D_{Ni} and D_{Mn} when melting at high T_p correspond to the sharp decrease in x_{Mg}^L and x_{Fe}^L following exhaustion of cpx.

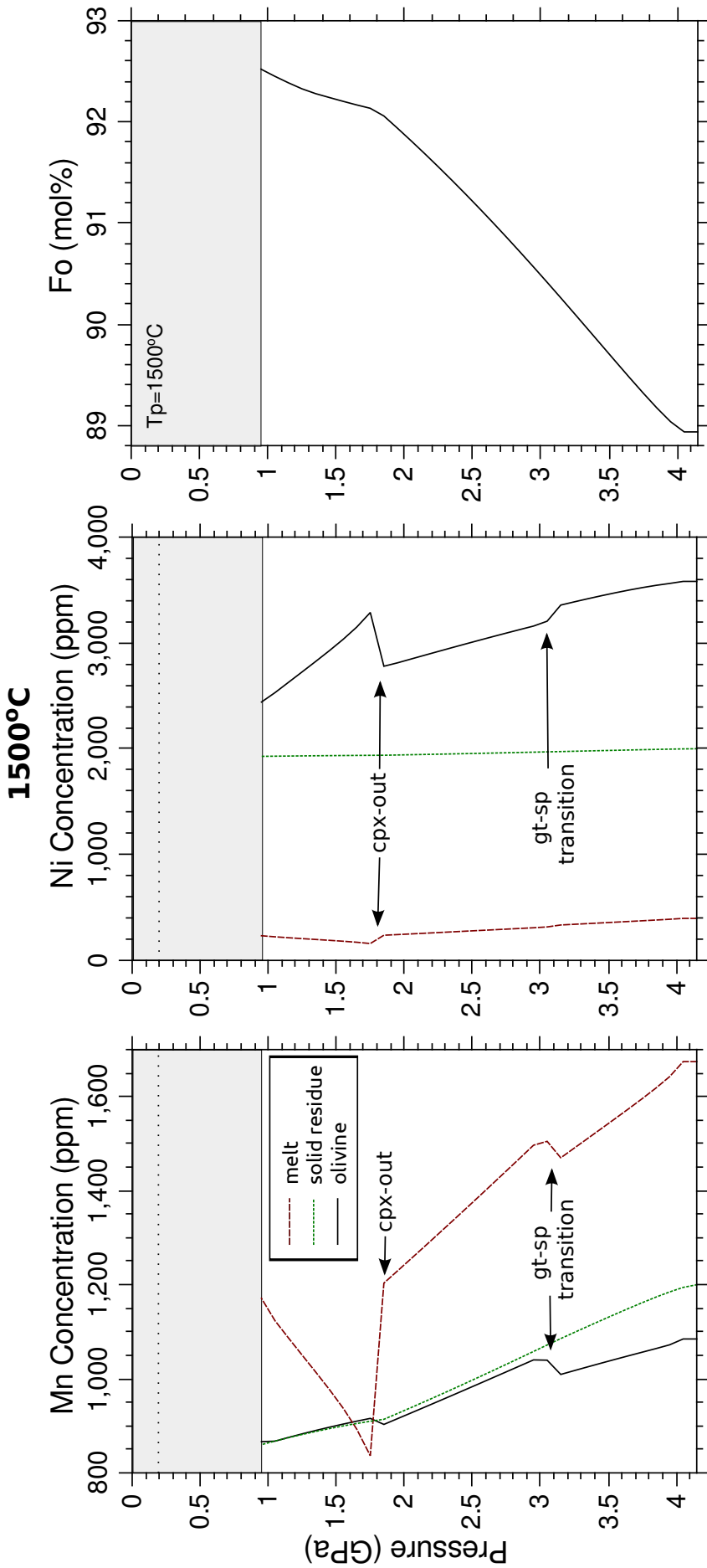


Figure 6.6: Ni and Mn contents of instantaneous fractional melts, the solid residue and the olivine derived from the melt fractions as a function of pressure within the melting column. Olivine crystallised from primitive fractional melts at the shallow basalt liquidus at 0.2 GPa in the crust (crystallisation horizon marked by horizontal dotted lines). The model results are shown for a mantle T_p of 1500°C and t_l of 30km to match estimates of crustal thickness in Iceland (Darbyshire *et al.*, 2000). Fo of the olivine in equilibrium with the fractional melts is also plotted. The model is run with an initial modal cpx of 10 wt%, $K_{D_{Fe^{2+}-Mg}}^{ol/L} = 0.3$, and initial concentrations of Mn and Ni in the mantle are 1200ppm and 2000ppm respectively.

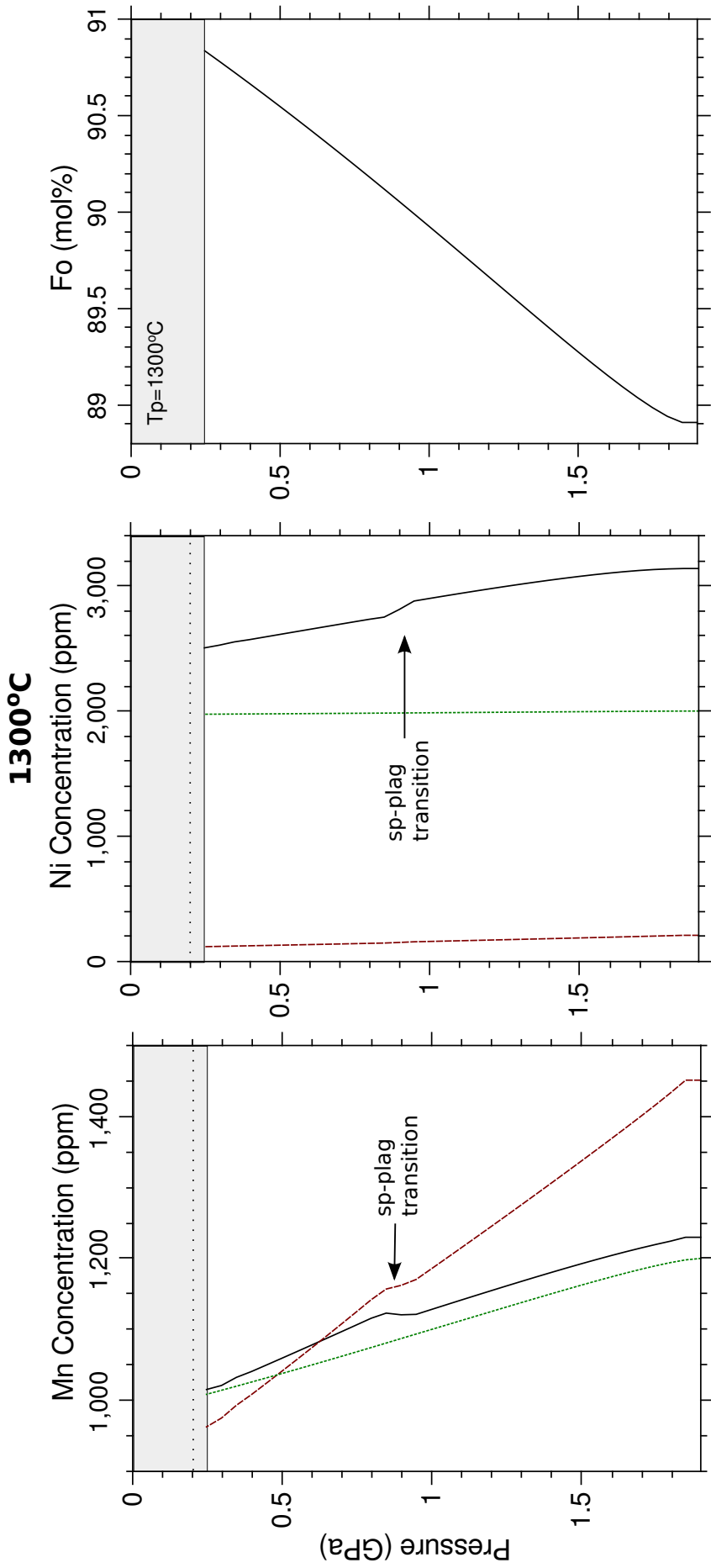


Figure 6.7: Ni and Mn contents of instantaneous fractional melts, the solid residue and the olivine derived from the melt fractions as a function of pressure within the melting column. Olivine crystallised from primitive fractional melts at the shallow basalt liquidus at 0.2 GPa in the crust (crystallisation horizon marked by horizontal dotted lines). The model results are shown for T_p of 1300°C and t_l of 7km to match the average oceanic crustal thickness at normal mid-ocean ridges. Fo of the olivine in equilibrium with the fractional melts is also plotted. The model is run with an initial modal cpx of 10 wt%, $K_{D_{Fe^{2+}-Mg}}^{ol/L} = 0.3$, and initial concentrations of Mn and Ni in the mantle are 1200 ppm and 2000 ppm respectively.

6.1 Effect of changing input variables

Exchange Coefficient

$K_{d_{Fe^{2+}-Mg}}^{ol/L}$ varies as a function of temperature pressure and melt composition. Recent experimental work has shown that $K_{d_{Fe^{2+}-Mg}}^{ol/L}$ covers at least the range 0.17-0.45 (Toplis, 2004). To simplify the model I have used a constant value throughout the melting column. The effect of changing its value is to change Fo of the olivine crystallised. Fo increases with decreasing $K_{d_{Fe^{2+}-Mg}}^{ol/L}$. When varied within the range $K_{d_{Fe^{2+}-Mg}}^{ol/L} = 0.25 - 0.35$ Fo changes by ~ 3 mol% (Figure 6.8). Changing $K_{d_{Fe^{2+}-Mg}}^{ol/L}$ has little effect on the olivine trace element concentration as all partition coefficients are largely independent of olivine composition.

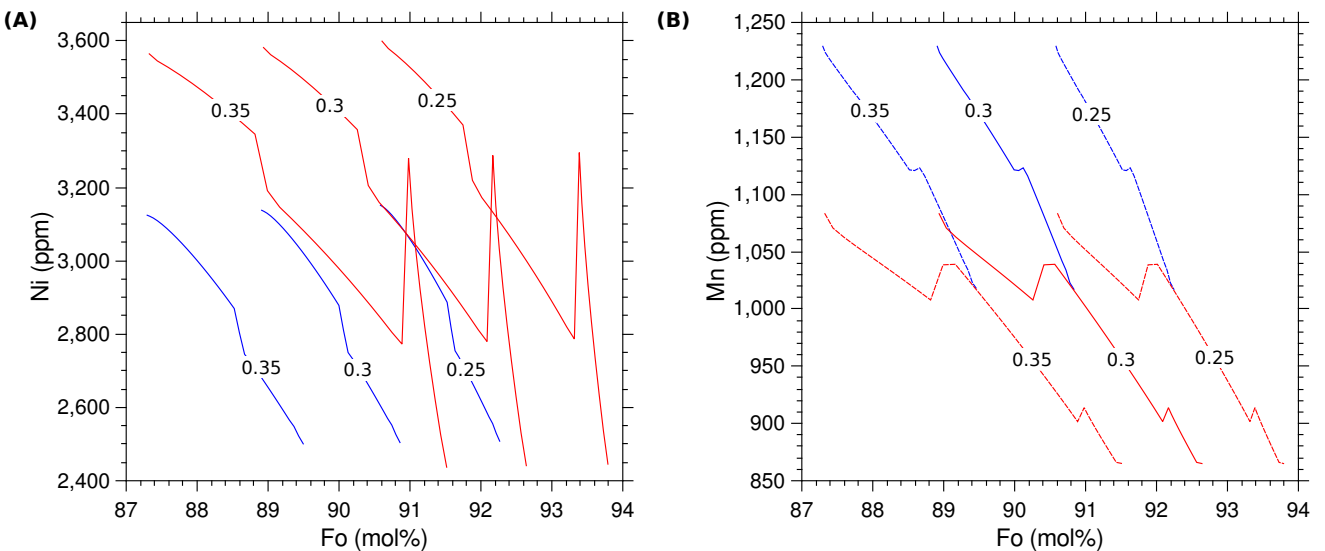


Figure 6.8: Effect of changing $K_{d_{Fe^{2+}-Mg}}^{ol/L}$ on model results of primitive olivine Ni and Mn concentration as a function of Fo. Results for two model set ups are shown. BLUE: Normal mid-ocean ridge conditions $T_p = 1300^\circ C$, $t_l = 7\text{ km}$. RED: Icelandic conditions $T_p = 1500^\circ C$, $t_l = 30\text{ km}$. Curves are labelled with the $K_{d_{Fe^{2+}-Mg}}^{ol/L}$ used.

Depth of garnet-spinel transition

Although not an input variable, this is one of the most poorly constrained parameters. It is shown here that, although changing the shape of the curves, varying the depth of the garnet-spinel transition has little effect on the ranges of Ni and Mn concentration of primitive olivine phenocrysts.

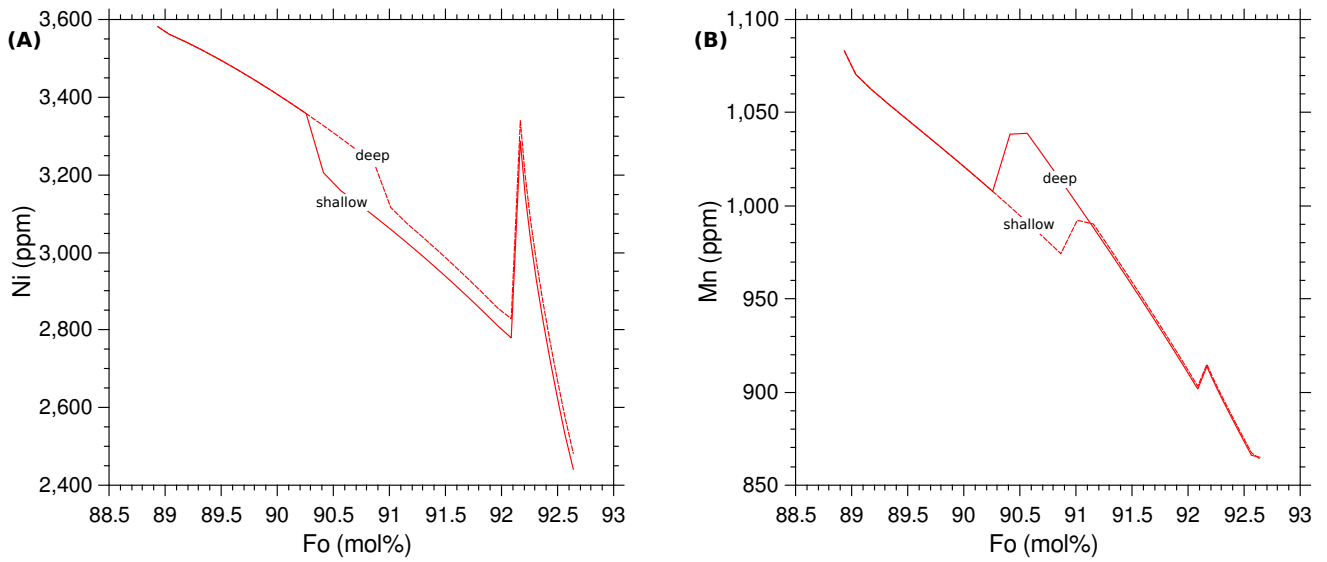


Figure 6.9: Effect of changing the depth of the garnet-spinel transition on model results of primitive olivine phenocryst Ni and Mn concentration as a function of Fo. Results for a set up run at $T_p = 1500^\circ C$, $t_l = 30\text{ km}$. The ‘deep’ curve corresponds to the transition depth reported by Robinson and Wood, 1998 and given as a function of T in section 5.2. The ‘shallow’ curve corresponds to a transition depth 0.4 GPa shallower than this.

Depth of olivine crystallisation

Most partition coefficients, including $D_{Mn}^{ol/L}$, have no explicit T-dependence. This means that provided the melt composition remains constant the concentration of olivine crystallised from the melt is independent of depth of crystallisation. $D_{Ni}^{ol/L}$ is temperature-dependent. Compatibility of Ni in olivine increases with decreasing temperature meaning olivine crystallised at shallower levels within the crust will be more enriched in Ni. Melts are stalled in the crust at a range of depths (e.g. White *et al.*, 2011) and olivine crystallised in mush-layers of deep chambers can be remobilised and erupted at the surface. For the Icelandic melting scenario varying the depth of crystallisation from 20km (lower crust intrusion) to 2km (shallow intrusion) causes Ni to increase by $\sim 300\text{ppm}$ (fig.6.10). For a polyphase crystallisation history in which olivine is crystallised at a range of depths, this effect may account for some of the variability observed in olivines from a single flow.

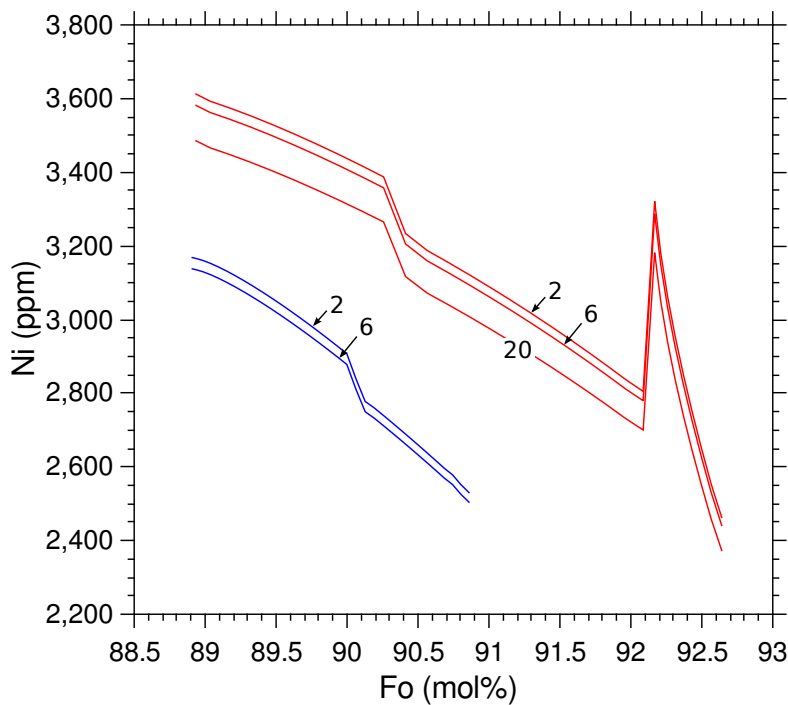


Figure 6.10: Effect of changing depth of olivine crystallisation within the crust on primitive olivine Ni concentration. Results for two model set ups are shown. BLUE: Normal mid-ocean ridge conditions $T_p = 1300^\circ\text{C}$, $t_l = 7\text{km}$. RED: Icelandic conditions $T_p = 1500^\circ\text{C}$, $t_l = 30\text{km}$. Curves are labelled with the depth of crystallisation in km.

Source concentration

The composition of the mantle beneath Iceland is inferred to vary on a short lengthscale (Shorttle and MacLennan, 2011). The consequence of this is that the initial trace element concentration cannot be assumed to be single-valued as magma erupted at the surface may sample a range of mantle compositions. This source variability may be largely responsible for the distribution of olivine Ni and Mn concentrations observed in a single eruption. Source heterogeneity is exaggerated in the final olivine composition. For example a range of 1000 ppm between minimum and maximum initial Ni leads to a range of 1800 ppm in the olivine concentration.

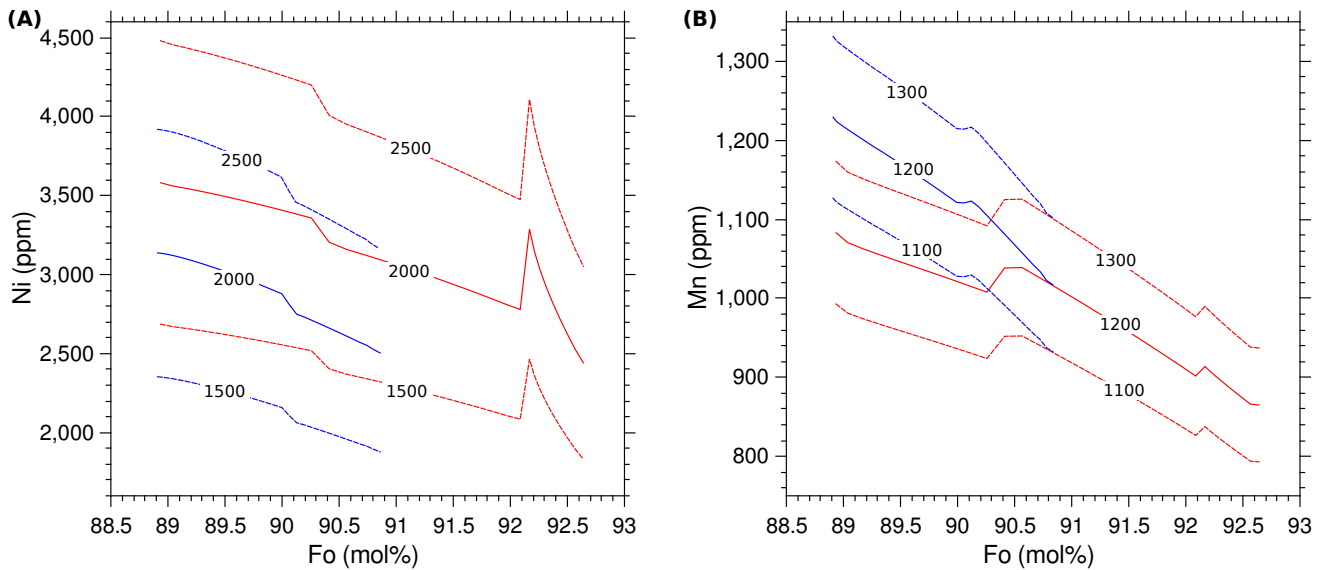


Figure 6.11: Effect of changing initial composition of mantle source on Ni and Mn concentrations of olivine phenocrysts. Results for two model set ups are shown. BLUE: Normal mid-ocean ridge conditions $T_p = 1300^\circ C$, $t_l = 7\text{ km}$. RED: Icelandic conditions $T_p = 1500^\circ C$, $t_l = 30\text{ km}$. Curves are labelled with the initial concentration of Ni or Mn in ppm. The solid lines are model results for the median mantle concentrations.

Source mineralogy

Mantle peridotite in the source region may be variably enriched or depleted. To explore the effect of fertility model results for the three peridotite modal mineralogies from section 5.2 are compared. Increasing fertility increases the modal cpx and decreases the relative abundance of olivine. This causes a slight increase in Ni concentration of the melt and of olivine crystallised from the melt due to the lower compatibility of Ni in cpx relative to olivine. Increased fertility has minor effect on Mn. The olivine Ni concentration from melting of a refractory harzburgite is lower for given Fo than for pyrolite due to the increased modal olivine. Mn concentration does not change in a predictable manner and is dependent on T_p . Cpx is exhausted from the residue very quickly causing productivity to be lower than when melting pyrolite. The effect of this is that lower melting degree and lower Fo are attained. The range in Ni and Mn concentrations are also significantly reduced.

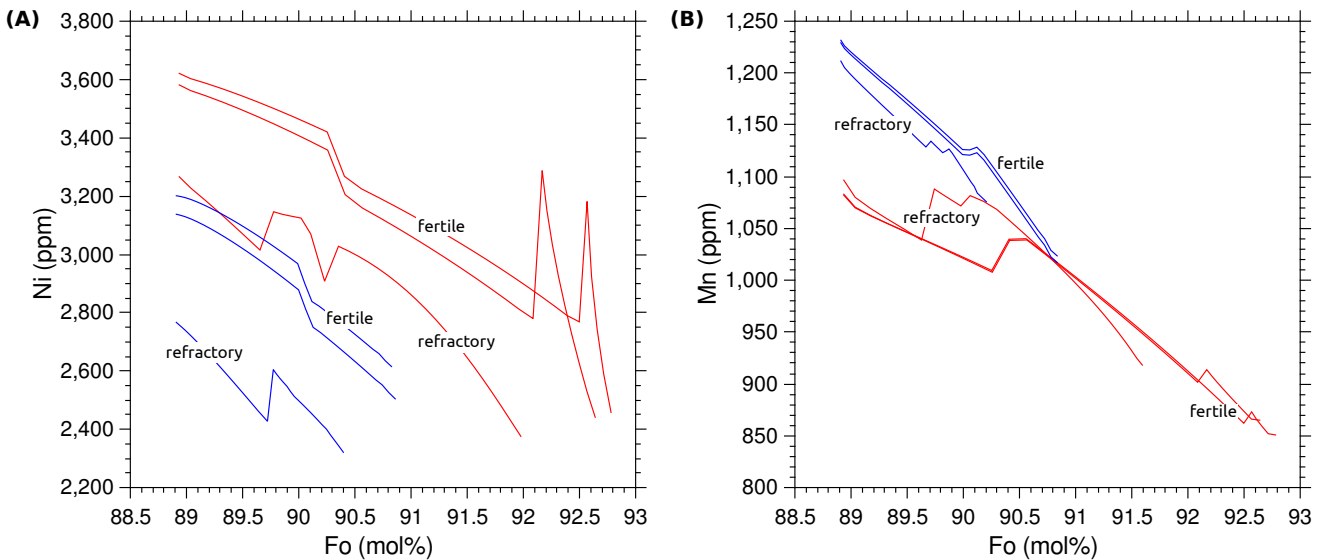


Figure 6.12: Effect of changing modal mineralogy of peridotite source on Ni and Mn concentrations of olivine phenocrysts. Results for two model set ups are shown. BLUE: Normal mid-ocean ridge conditions $T_p = 1300^\circ\text{C}$, $t_l = 7\text{km}$. RED: Icelandic conditions $T_p = 1500^\circ\text{C}$, $t_l = 30\text{km}$. The solid lines correspond to a ‘normal’ DMM (Workman and Hart, 2005), the dashed lines labelled ‘fertile’ correspond to a fertile lherzolite (KR4003; Walter, 1998), and the dash-dot lines labelled ‘refractory’ correspond to a refractory harzburgite (84-402; Eggins *et al.*, 1998).

7 Discussion

7.1 Comparison of model to olivine data: Can fractional melting do it?

The model shows that a wide range of melt compositions can be achieved during fractional melting of peridotite. The fundamental question this project aims to address is whether fractional melting of peridotite alone is sufficient to explain observed olivine minor element concentrations. This question is explored by comparison of synthetic results with measured olivine concentrations from Iceland and other geodynamic settings.

Icelandic data

On Iceland seismic and gravity studies constrain crustal thickness on Iceland to vary between 20 and 40km (Darbyshire *et al.*, 2000). The mantle T_p beneath Iceland is estimated to be $1480 - 1520^\circ\text{C}$ (Maclellan *et al.*, 2001). Melting is therefore modelled using $T_p=1500^\circ\text{C}$ and $t_l=30\text{km}$. ‘Normal’ pyrolytic mantle mineralogy is used, and olivine is made to crystallise at 6km depth. To match the Fo of the Icelandic data $K_{d_{Fe^{2+}-Mg}}^{ol/L} = 0.28$ is used. The fit of the model to the Icelandic data is first considered for Iceland as a whole, before focussing on how the differences between individual eruptions can be explained.

The ranges in model Ni and Mn concentrations of olivines crystallised from instantaneous fractional melts are significant, particularly for Ni. When extrapolated back to Fo=90-92 all Ni concentrations (excluding one anomalously forsteritic olivine from Midfell) can be fit by instantaneous fractional melts of a peridotite with initial bulk Ni of 1750ppm. For this to be the case all melt fractions, including the endmember melts generated at the very base and very top of the melting column, would have to ascend to the surface and erupt through the crust without any mixing or homogenisation occurring. For reasons discussed in section 5.3 this is unlikely to be true. If however the Ni concentration of the initial mantle source is allowed to range between 1500 and 2000ppm the data can be fit by the aggregated melts. This applies to both point average composition, which is used here to represent the case of partial homogenisation, and point and depth average composition, which would apply to the case of complete mixing of melts throughout the melting region. This interpretation requires the concentration of Ni in the mantle beneath Iceland to be at the lower end of the global distribution.

When coupled with models of Mn concentration the case for some degree of source heterogeneity is stronger. The range in Mn concentration from instantaneous fractional melts is not as large as for Ni and a single source composition is not sufficient to fit the data. Rather initial bulk Mn concentration is required to vary between 1100 and 1300ppm, i.e. cover almost the full range in estimated peridotite concentrations. As for Ni, Mn concentrations can be fit by any degree of melt mixing.

Additional variability in the model could also be introduced by allowing T_p to vary slightly (i.e. between $1450-1550^\circ\text{C}$), and by allowing polybaric crystallisation.

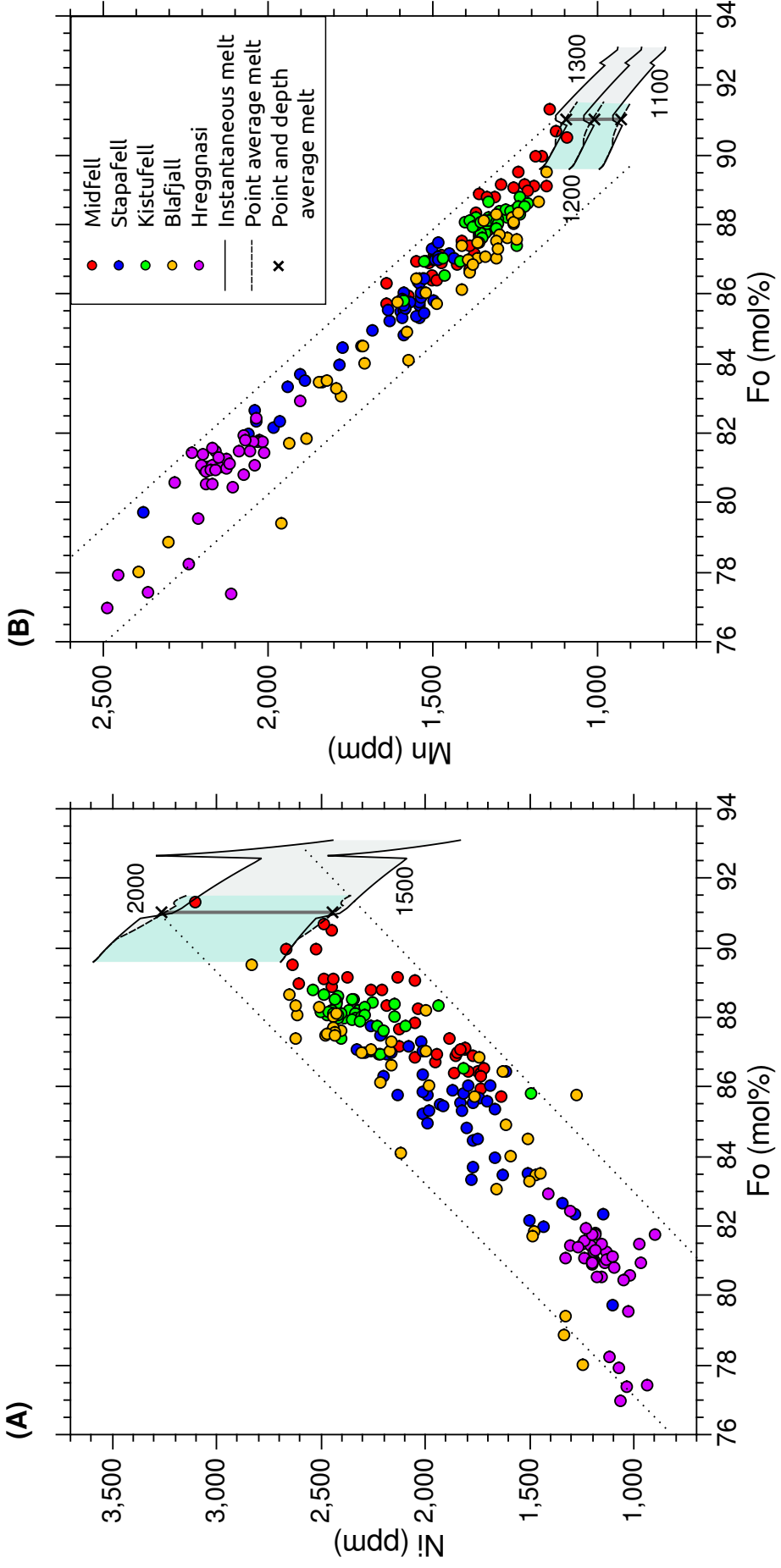


Figure 7.1: Comparison of Ni and Mn concentrations of olivine from five Icelandic eruptions with model results of primitive olivine compositions crystallised from fractional melts of pyrolytic peridotite. For both (A) and (B) dotted lines represent the crystal line of descent during olivine fractionation, allowing the evolved samples to be extrapolated back to their parental compositions. The model has been run at a range of initial concentrations of Ni and Mn in the source. Model curves are labelled with initial concentrations in ppm. For each initial concentration predicted compositions of olivines crystallised from both instantaneous fractional melts and aggregated melts (point average melt and point and depth average melt, see text) are shown. Shaded regions represent the ranges in olivine composition predicted by the model when initial source concentration is varied between the labelled values: light grey region = olivine crystallised from instantaneous fractional melts; turquoise region = olivine crystallised from point average aggregated melt; dark grey bar = olivine crystallised from point and depth average aggregated melt.

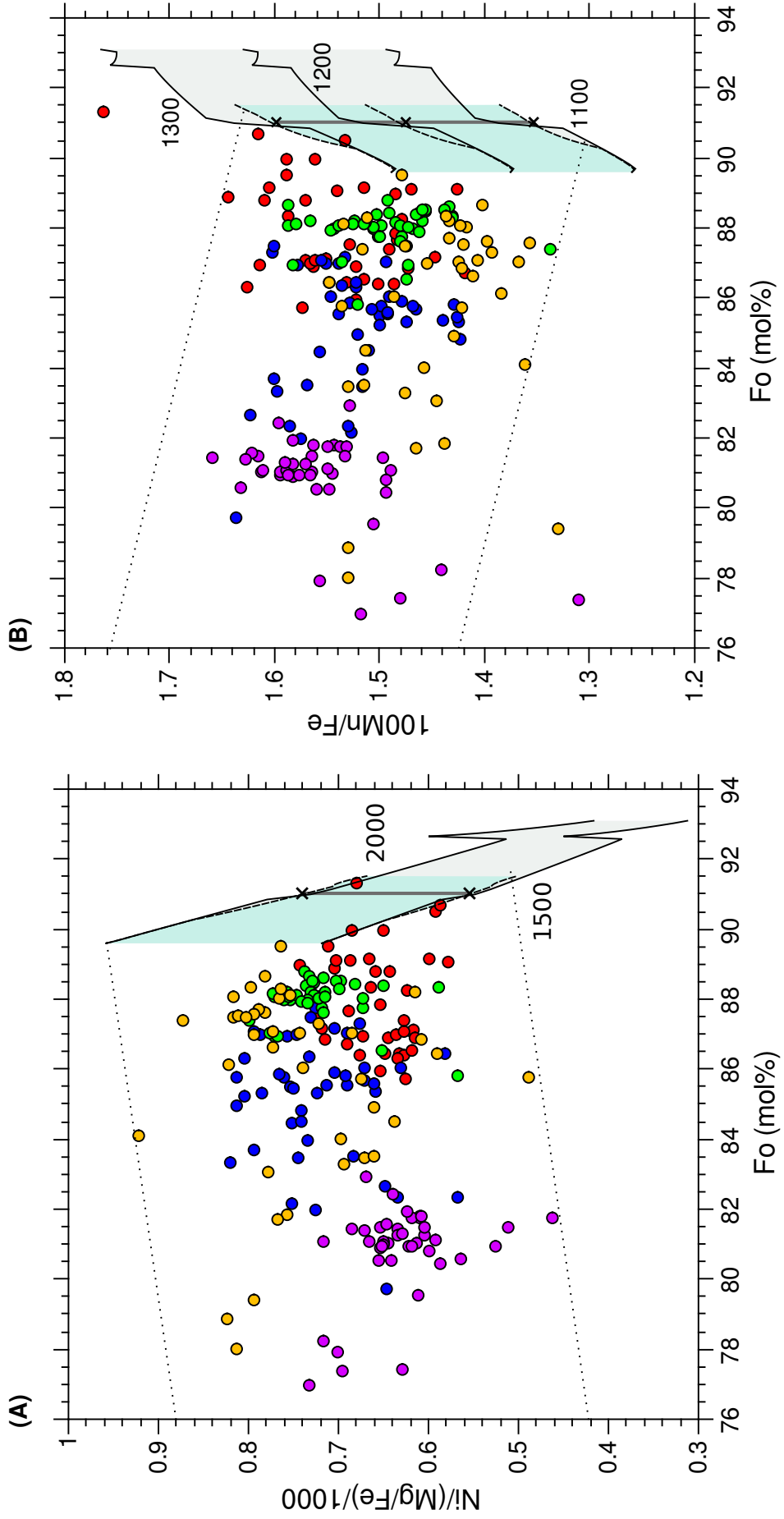


Figure 7.2: Comparison of $\text{Ni}/(\text{Mg}/\text{Fe})$ and Mn/Fe ratios measured in olivine from five Icelandic eruptions with model results of primitive olivine compositions crystallised from fractional melts of pyrolytic peridotite. For both (A) and (B) dotted lines represent the crystal line of descent during olivine fractionation, allowing the evolved samples to be extrapolated back to their parental compositions. The model has been run at a range of initial concentrations of Ni and Mn in the source. Model curves are labelled with initial concentrations in ppm. For each initial concentration predicted compositions of olivines crystallised from both instantaneous fractional melts and aggregated melts (point average melt and point and depth average melt) are shown. Shaded regions represent the ranges in olivine composition predicted by the model when initial source concentration is varied between the labelled values. Shading as described in figure 7.1.

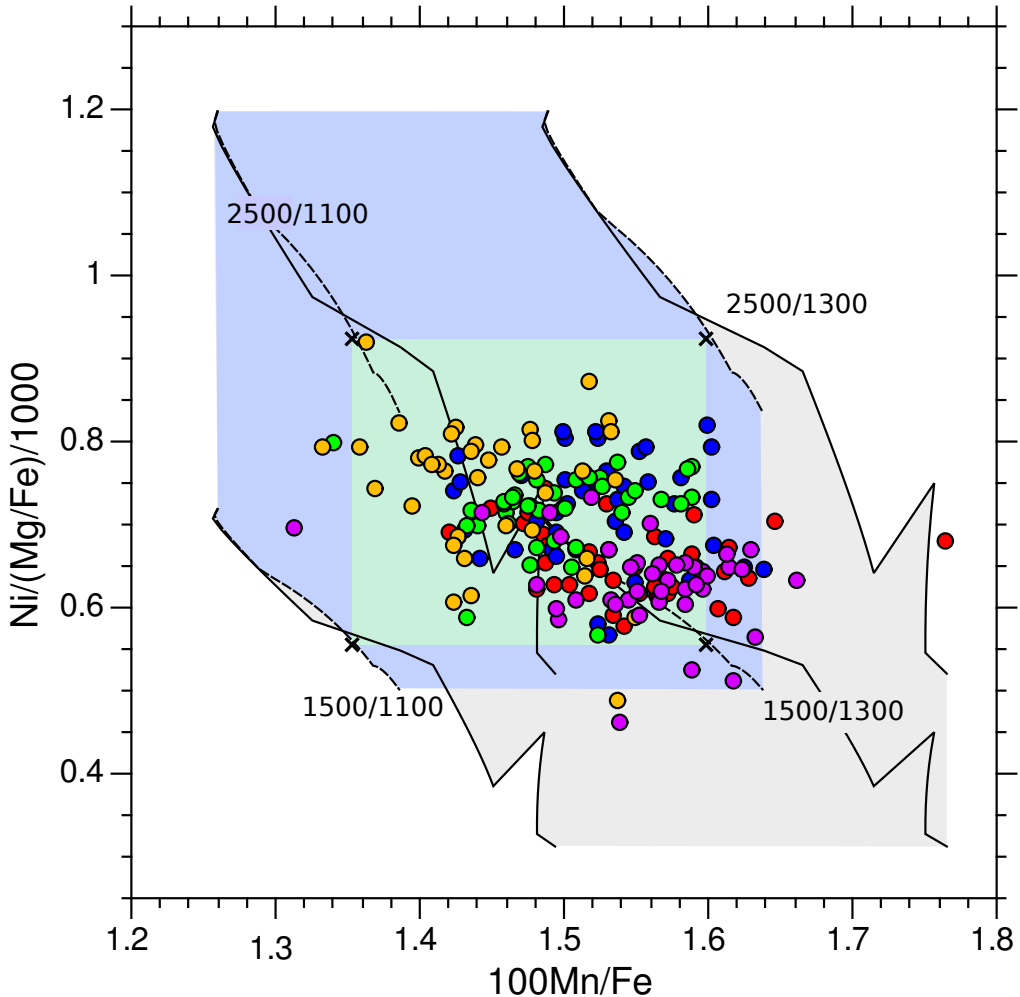


Figure 7.3: Comparison of $\text{Ni}/(\text{Mg}/\text{Fe})$ and Mn/Fe ratios (which are roughly independent of olivine fractionation) measured in olivine from five Icelandic eruptions with model results of primitive olivine compositions crystallised from fractional melts of pyrolytic peridotite. The model has been run at a range of initial concentrations of Ni and Mn in the source. Model curves are labelled with initial concentrations in ppm reported as $[\text{Ni}]_{\text{initial}}/[\text{Mn}]_{\text{initial}}$. For each initial concentration predicted compositions of olivines crystallised from both instantaneous fractional melts and aggregated melts (point average melt and point and depth average melt) are shown. Shaded regions show the range of olivine compositions predicted by the model: grey: olivine crystallised from instantaneous fractional melts; blue region= olivine crystallised from point average aggregated melt; turquoise region= olivine crystallised from point and depth average aggregated melt. Almost all samples lie within the shaded regions indicating that the basalts can be derived from fractional melting of a typical peridotite.

The requirement of a range of initial Ni and Mn source concentrations implies that the mantle beneath Iceland is heterogeneous on a small-scale. The small-scale variability can be mapped at higher resolution by looking at the composition of individual eruptions from different areas of Iceland.

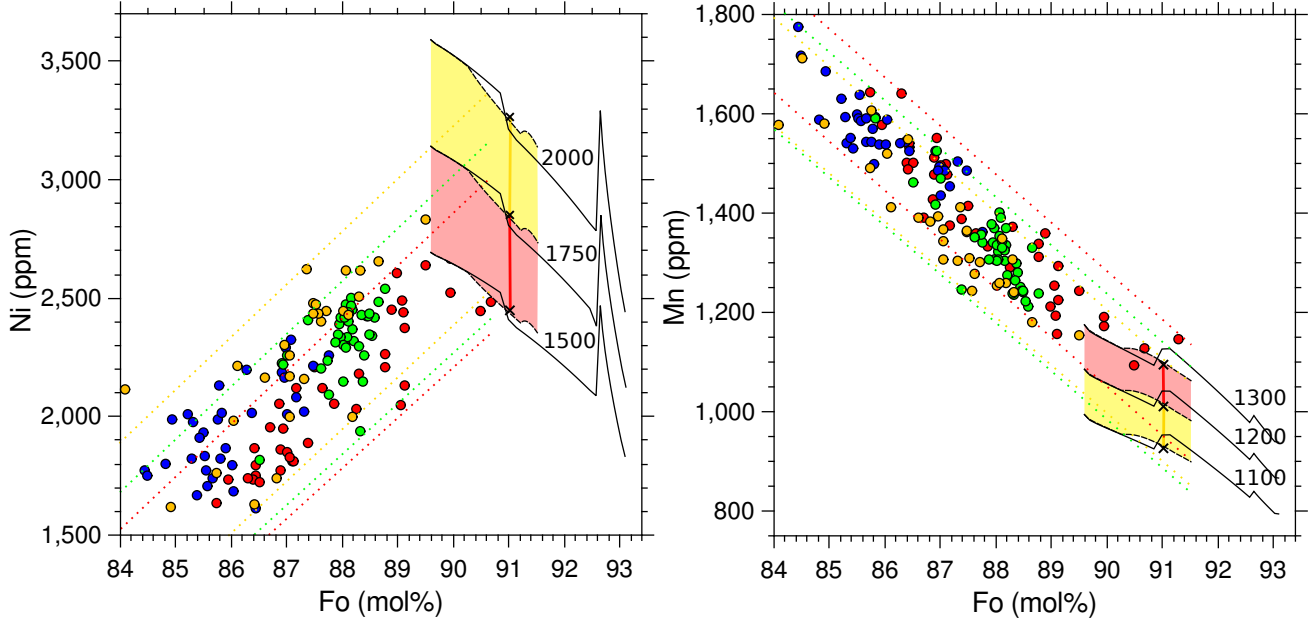


Figure 7.4: Comparison of Ni and Mn concentrations of olivines from the three most primitive Icelandic flows sampled (Midfell, Blafjall and Kistufell) with model results. To fit data from different eruptions, slightly different distributions in initial source concentration of Ni and Mn are required. Model results are labelled with the initial concentrations in ppm.

Global data

To further test the applicability of the melting model, model results are compared to olivine Ni and Mn concentrations from the global dataset of Sobolev *et al.* [2007]. This data is divided into four groups: (i) MORB; (ii) within plate magmas (WPM, magmas erupted far from plate boundaries) forming ocean island basalts (OIB) emplaced over thin lithosphere (<70 km thick), WPM-THIN; (iii) WPM (OIB and large igneous provinces (LIP)) emplaced over thick lithosphere (>70 km thick), WPM-THICK; and (iv) komatiites and associated magmas, KOMATIITES (these will not be considered here). WPM-thin and WPM-thick are associated with mantle hot-spots where mantle T_p is elevated ($1450 - 1550^\circ C$). The groups show distinct minor element trends. Olivine from WPM-thick samples is highly enriched in Ni and depleted in Mn relative to MORB while olivines from the WPM-thin group (which includes Icelandic samples) have intermediate Ni and Mn contents.

To evaluate the range of possible results the model is initially run at a T_p of $1250^\circ C$ and $1550^\circ C$ to bracket the range of T_p in the different melting settings. All other conditions are the same as when modelling the Icelandic data.

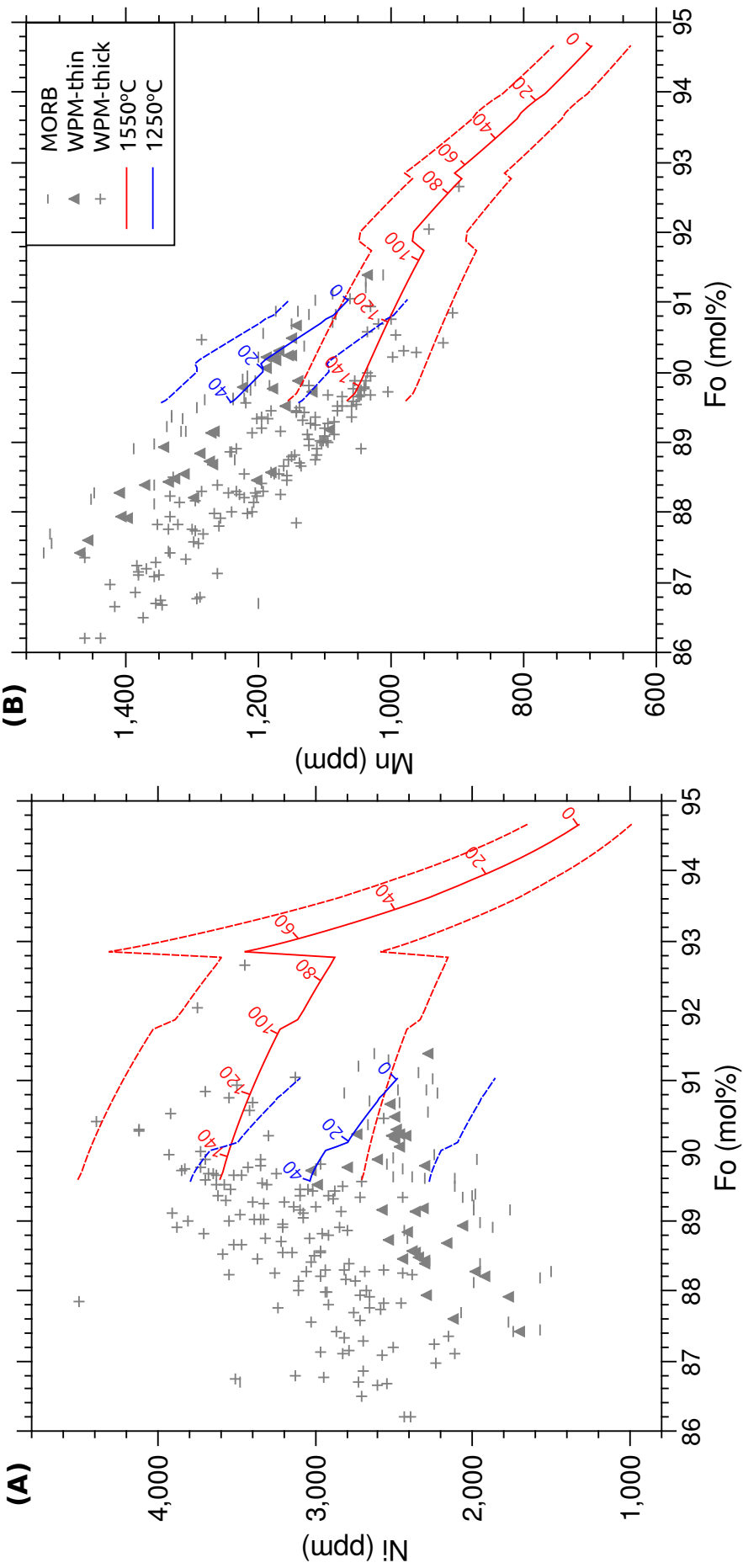


Figure 7.5: Comparison of Ni and Mn concentrations of olivine from the global dataset from Sobolev *et al.* [2007] with model results of compositions of primitive olivine crystallised from fractional melts of pyrolytic peridotite. Curves correspond to compositions of olivines crystallised from instantaneous fractional melts. Modelled for a range of initial concentrations of Ni and Mn in the source: $[Ni]_{\text{initial}}=2000\pm 500 \text{ ppm}$; $[Mn]_{\text{initial}}=1200\pm 100 \text{ ppm}$. Solid curves correspond to the median initial concentrations. Median curves are contoured for depth in km. Melting stops when the base of the lithosphere is reached meaning that for a given setting the curves are cut off at the local value of t_1 .

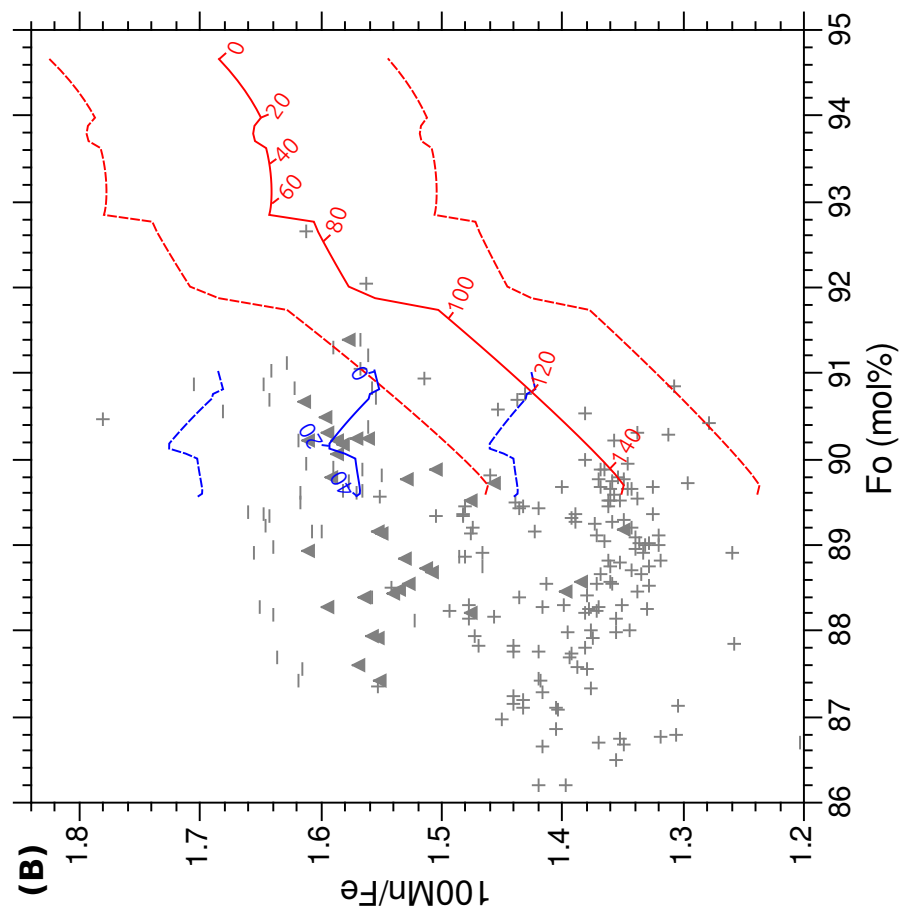
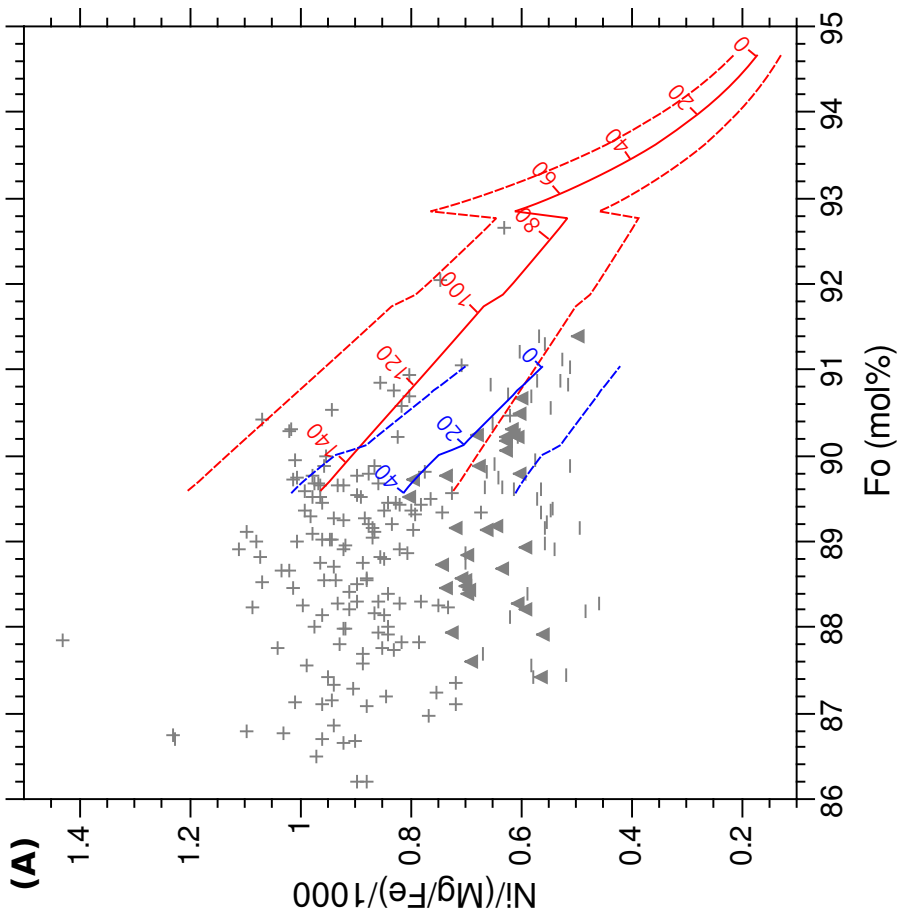


Figure 7.6: Comparison of $\text{Ni}/(\text{Mg}/\text{Fe})$ and Mn/Fe ratios from olivine from the global dataset from Sobolev *et al.* [2007] with model results of compositions of primitive olivine crystallised from fractional melts of pyrolytic peridotite. Curves correspond to compositions of olivines crystallised from instantaneous fractional melts. Modelled for a range of initial concentrations of Ni and Mn in the source: $[\text{Ni}]_{\text{initial}} = 2000 \pm 500 \text{ ppm}$; $[\text{Mn}]_{\text{initial}} = 1200 \pm 100 \text{ ppm}$. Solid curves correspond to the median initial concentrations. Median curves are contoured for depth in km. Melting stops when the base of the lithosphere is reached meaning that for a given setting the curves are cut off at the local value of t_1 .

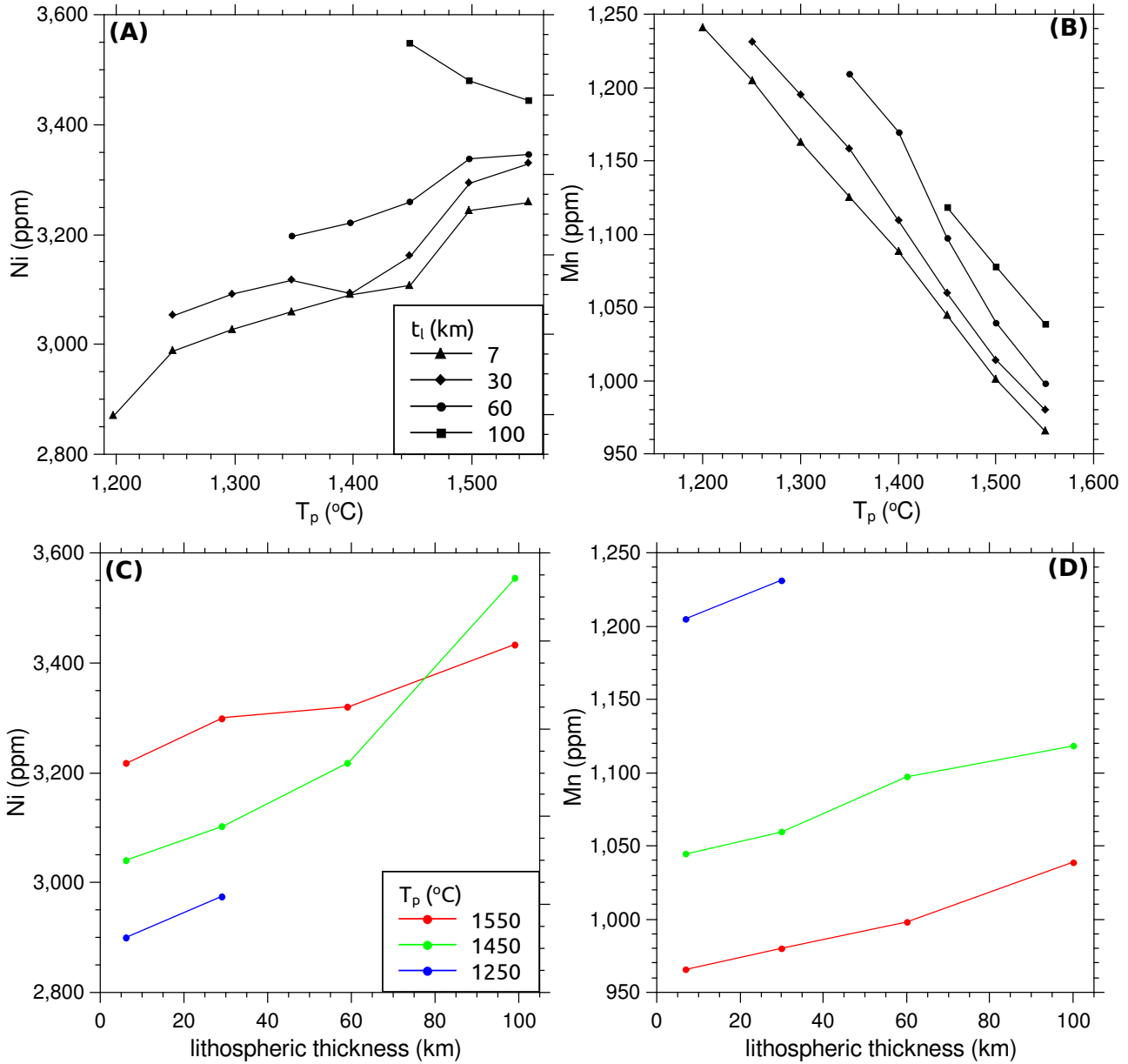


Figure 7.7: Ni and Mn concentrations of primitive olivine crystallised from the point and depth average melt generated in the melting region as a function of T_p ((A) and (B)), and t_l ((C) and (D)).

T_p is clearly an important parameter controlling olivine composition. Relative enrichment of Ni and depletion of Mn is predicted for olivines generated at high T_p . Due to the larger P range over which melting occurs and the greater degree of melting, the compositional range of instantaneous fractional melts is much larger for elevated T_p . The effects of T_p and t_l on the average fractional melt compositions are shown in figure 7.7.

Model parameters are then modified to optimise fit for different geodynamic settings. These fits are shown in figures 7.8-7.10. Almost all primitive olivine compositions can be generated by fractional melting of peridotite with variable bulk Mn and Ni concentrations and data can also be fit by variable degrees of melt mixing. The initial concentrations required are all within the estimated ranges for global peridotites. The model parameters used to fit the global data are given in table 9.

	T _p	t _l	K _{d_{Fe²⁺-Mg}} ^{ol/L}	[Ni] _{initial}	[Mn] _{initial}	source mineralogy
MORB	1300°C	7km	0.25	1500-2000ppm	1100-1200ppm	pyrolite ¹
WPM-thin	1500°C	40km	0.27	1500-2000ppm	1100-1300ppm	pyrolite ¹
WPM-thick	1500°C	100km	0.27	1500-2500ppm	1100-1300ppm	pyrolite ¹

Table 9: Model input parameters used to for curves shown in figures 7.8-7.10 for different geo-dynamic settings. 1. DMM mineralogy from Workman and Hart [2005].

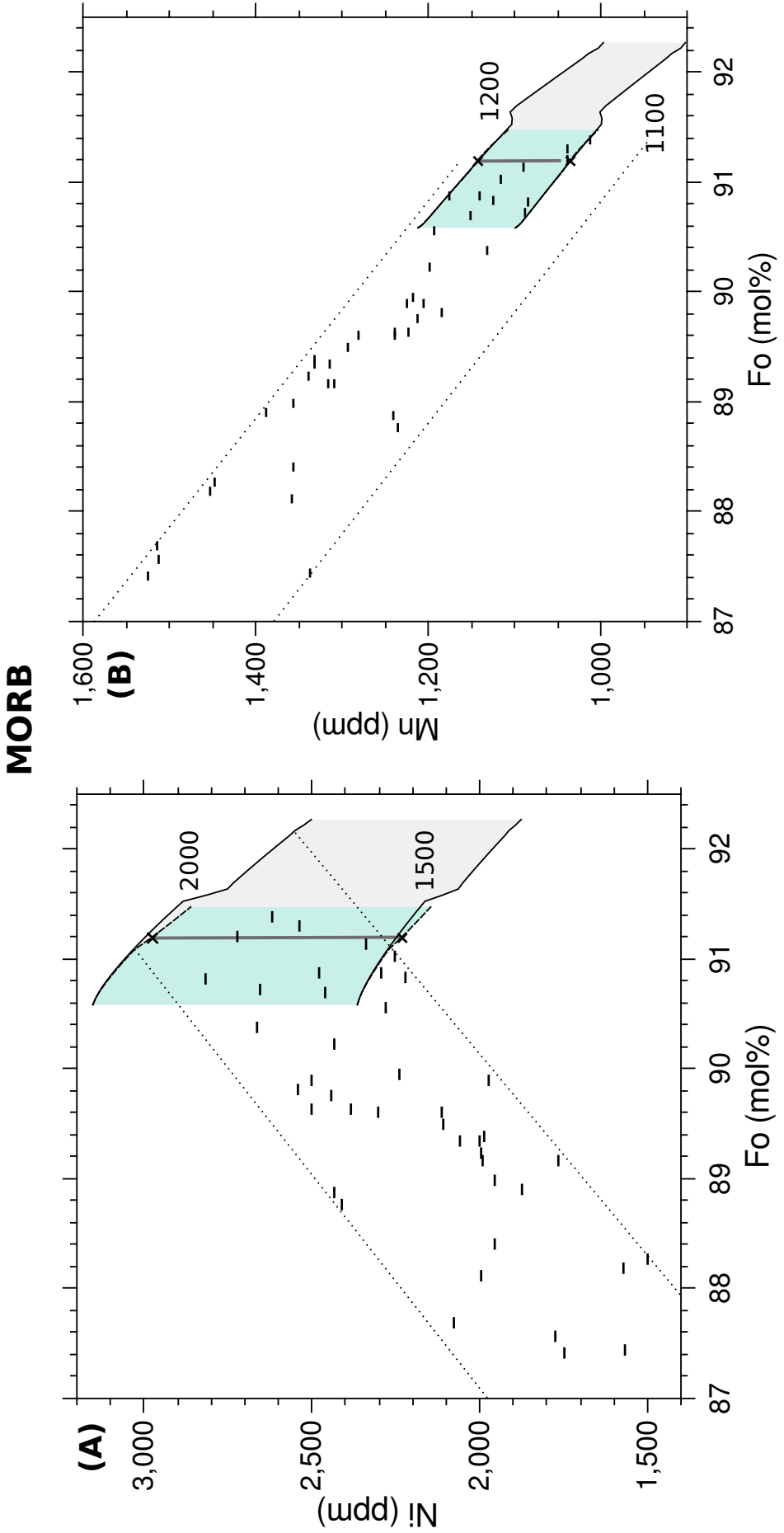


Figure 7.8: Comparison of Ni and Mn contents of olivines from MORB (taken from Sobolev *et al.*, 2007) with model results. Dotted lines represent the crystal line of descent during olivine fractionation, allowing the evolved samples to be extrapolated back to their parental compositions. Shown for a range of initial Ni and Mn in the source, which are labelled in ppm. Compositions of olivines crystallised from both instantaneous fractional melts and aggregated melts (point average melt and point and depth average melt) are shown. Shaded regions represent the ranges in olivine composition predicted by the model when initial source concentration is varied between the labelled values.

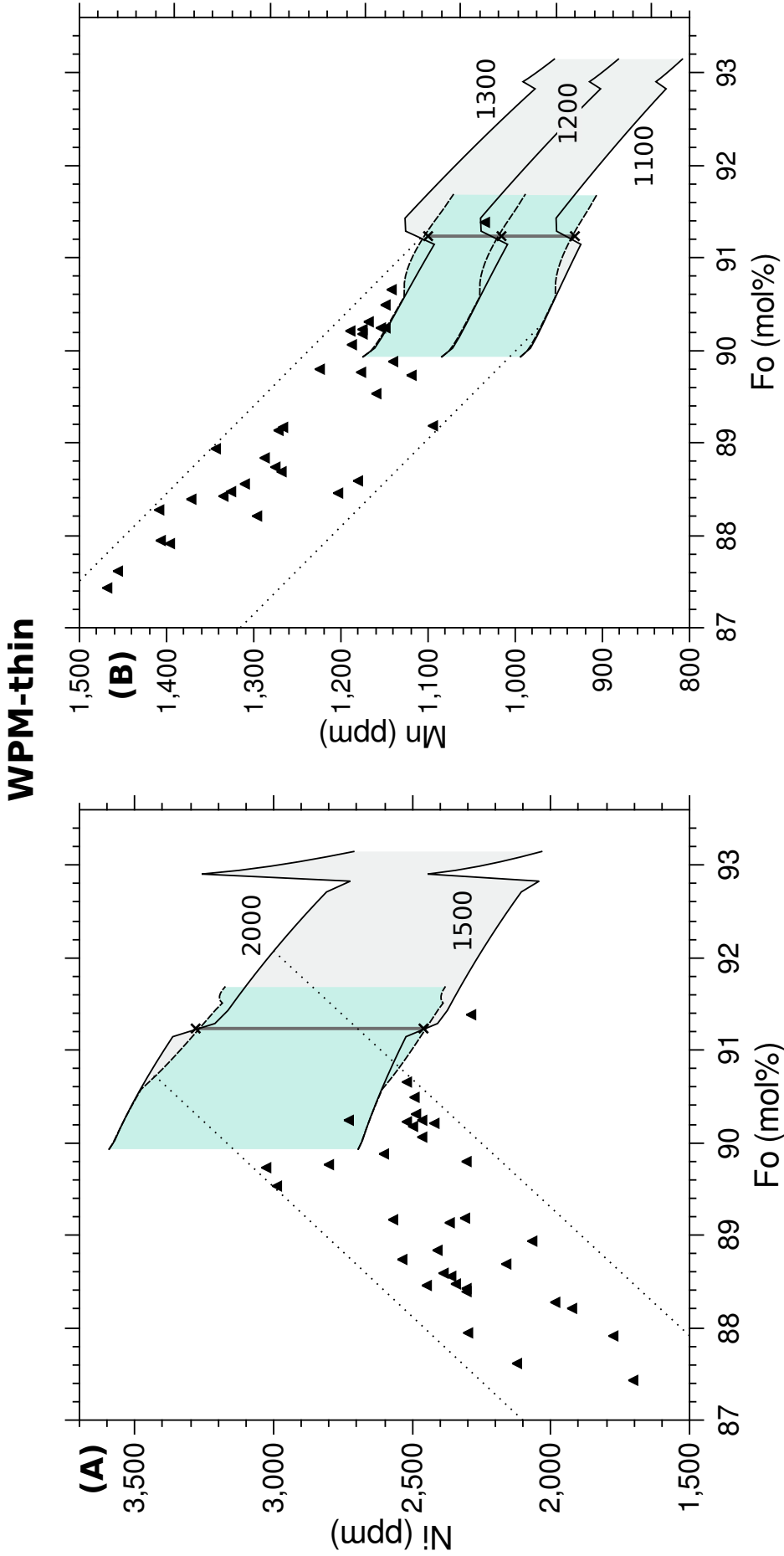


Figure 7.9: Comparison of Ni and Mn contents of olivines from WPM-thin (taken from Sobolev *et al.*, 2007) with model results. Dotted lines represent the crystal line of descent during olivine fractionation, allowing the evolved samples to be extrapolated back to their parental compositions. Shown for a range of initial Ni and Mn in the source, which are labelled in ppm. Compositions of olivines crystallised from both instantaneous fractional melts and aggregated melts (point average melt and point and depth average melt) are shown. Shaded regions represent the ranges in olivine composition predicted by the model when initial source concentration is varied between the labelled values.

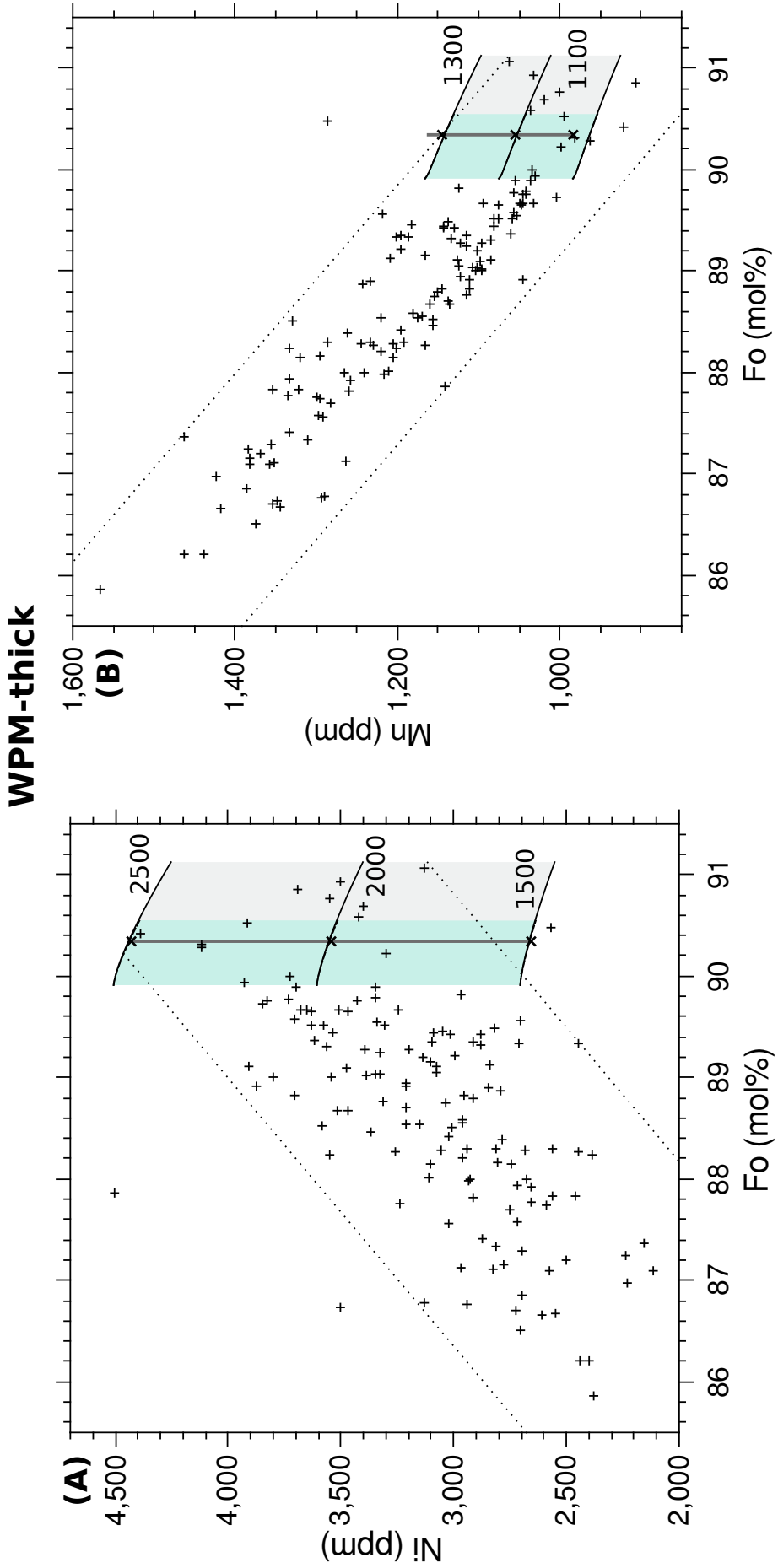


Figure 7.10: Comparison of Ni and Mn contents of olivines from WPM-thick (taken from Sobolev *et al.*, 2007) with model results. Dotted lines represent the crystal line of descent during olivine fractionation, allowing the evolved samples to be extrapolated back to their parental compositions. Shown for a range of initial Ni and Mn in the source, which are labelled in ppm. Compositions of olivines crystallised from both instantaneous fractional melts and aggregated melts (point average melt and point and depth average melt) are shown. Shaded regions represent the ranges in olivine composition predicted by the model when initial source concentration is varied between the labelled values.

7.2 Constraints on mantle source heterogeneity

Almost all the olivine compositions measured from both the new Icelandic data and published data are consistent with fractional melting of pyrolytic peridotite followed by fractionation of olivine in a crustal magma chamber. Some compositional heterogeneity is required, but this variation is well within the range observed in peridotitic mantle xenoliths and abyssal peridotites. Such variability can be envisioned to be caused by variable depletion by partial melting to produce basaltic melts or by metasomatic enrichment by addition of recycled MORB. Importantly an olivine-free source lithology as hypothesised by a number of researchers (e.g. Herzberg *et al.*, 2013; Sobolev *et al.*, 2005, 2007) is not required. The differences in the distributions of Ni and Mn concentrations seen in different geodynamic settings are principally controlled by the combined effects of variable T_p and t_l .

The higher upper bound of bulk Ni in the source required to fit data from the WPM-thick group suggests that compositional variation is convolved with fusibility of the source. Rather than being due to elevated bulk Ni and Mn in this source material this is more likely to be a result of mineralogical variability as hypothesised by Shorttle and MacLennan [2011]. Further modelling using sources variably enriched in basaltic melts is required to show this, however to do this the reduction in solidus temperature for these more fusible sources needs to be taken into consideration. To get a more complete story one needs to look at isotopes. Many studies have shown correlation between isotopes incompatible trace elements and major elements (e.g. Fitton, 2003; Shorttle and MacLennan, 2011) suggesting heterogeneities do exist as mineralogically distinct regions.

As shown from the variation within single eruption and between different eruptions on Iceland, mantle heterogeneity must occur on a small-scale with the Icelandic mantle plume.

8 Conclusions

- FRTE partition coefficients are found to be strongly dependent on the major element melt composition which in turn is controlled by mantle T_p . The accurate melt composition control often overwhelms explicit temperature dependence. As T_p increases D_{Mn} decreases while D_{Ni} tends to increase causing the Mn content of crystallised olivine to decrease and Ni content to increase. Peaks in D_{Mn} and D_{Ni} , and correspondingly in olivine Mn and Ni concentration, occur at the point when clinopyroxene is exhausted from the residue.
- For the Icelandic samples ranges of 1200pm and 1500ppm are found in the Ni and Mn concentrations respectively, with a large part of this variation correlating with olivine fractionation. At given Fo ranges of 800ppm and 300ppm are observed in Ni and Mn respectively. Of the three most primitive samples studied, Blafjall has the highest Ni and lowest Mn content while Midfell has the greatest affinity to MORB, with lower Ni and higher Mn. These differences are most likely to reflect differences in source composition.
- For Ni and Mn, the range in minor element concentrations of primitive olivines can be generated solely by the fractional melting of peridotitic mantle. An olivine-free source lithology is not required.
- The comparison indicates that a single source composition cannot account for all the variation in Ni and Mn. The variation in initial bulk Ni and Mn concentration of the peridotite required to match the data is in line with published estimates based on mantle xenoliths and abyssal peridotites.
- When source variability is permitted, data can be fit by any degree of melt mixing. The absence of highly forsteritic olivine ($Fo > 92$) predicted for instantaneous fractional melts generated at shallow levels does however imply that some mixing of melts occurs.
- The variation in Ni and Mn concentrations between olivines from a single sample and from different eruptions implies that lithological heterogeneity occurs on a short lengthscale within the mantle plume.
- Preferential sampling of the high Ni and low Mn source in areas overlain by thick lithosphere indicates that compositional variation is convolved with fusibility and hence mineralogy of the source.
- This work highlights the important role of fractional melting in minor element partitioning and draws into question the validity of quantitative estimates of the amount of recycled material in the mantle source region based on simplified melting models. Further work is required to develop a bimimetic melting model for a peridotite-pyroxenite mantle source to evaluate more directly the potential contribution of olivine-free lithologies in the source region. If it is found that ranges in Ni and Mn contents of olivine crystallised from fractional melts of peridotite and pyroxenite overlap considerably it would be impossible to deconvolve the relative contributions from the different lithologies. There would be a tradeoff between extent of mixing of instantaneous fractional melts from different levels in the melting region and the contribution from melting of recycled lithologies.

References

- Claude J Allègre and Donald L Turcotte. Implications of a two-component marble-cake mantle. *Nature*, 323:123–127, 1986.
- P. D. Asimow, J. E. Dixon, and C. H. Langmuir. A hydrous melting and fractionation model for mid-ocean ridge basalts: Application to the Mid-Atlantic Ridge near the Azores. *Geochemistry, Geophysics, Geosystems*, 5(1):n/a–n/a, January 2004.
- Paul Beattie, Clifford Ford, and Douglas Russell. Partition coefficients for olivine-melt and orthopyroxene-melt systems. *Contributions to Mineralogy and Petrology*, 109:212–224, 1991.
- Paul Beattie. Olivine-melt and orthopyroxene-melt equilibria. *Contributions to Mineralogy and Petrology*, 115(1):103–111, 1993.
- D R Bell and G R Rossman. Water in Earth's Mantle: The Role of Nominally Anhydrous Minerals. *Science (New York, N.Y.)*, 255(5050):1391–7, March 1992.
- R Benito-García and J López-Ruiz. Mineralogical changes of the residual solid and trace-element fractionation during partial incongruent melting. *Geochimica et Cosmochimica Acta*, 56(10):3705–3710, 1992.
- Ilya N. Bindeman, Andrew M. Davis, and Michael J. Drake. Ion Microprobe Study of Plagioclase-Basalt Partition Experiments at Natural Concentration Levels of Trace Elements. *Geochimica et Cosmochimica Acta*, 62(7):1175–1193, 1998.
- G. Borghini, P. Fumagalli, and E. Rampone. The Stability of Plagioclase in the Upper Mantle: Subsolidus Experiments on Fertile and Depleted Lherzolite. *Journal of Petrology*, 51(1-2):229–254, December 2009.
- K Breddam. Kistufell: Primitive Melt from the Iceland Mantle Plume. *Journal of Petrology*, 43(2):345–373, 2002.
- Fiona A Darbyshire, Robert S White, and Keith F Priestley. Structure of the crust and uppermost mantle of Iceland from a combined seismic and gravity study. *Earth and Planetary Science Letters*, 181(3):409–428, 2000.
- Rajdeep Dasgupta, Matthew G Jackson, and Cin-Ty A Lee. Major element chemistry of ocean island basalts – Conditions of mantle melt heterogeneity of mantle source. *Earth and Planetary Science Letters*, 289:377–392, 2010.
- F. A. Davis, J. A. Tangeman, T. J. Tenner, and M. M. Hirschmann. The composition of KLB-1 peridotite. *American Mineralogist*, 94(1):176–180, January 2009.
- Fred A. Davis, Munir Humayun, Marc M. Hirschmann, and Rupert S. Cooper. Experimentally determined mineral/melt partitioning of first-row transition elements (FRTE) during partial melting of peridotite at 3GPa. *Geochimica et Cosmochimica Acta*, 104:232–260, 2013.
- Michael J Drake and Daniel F Weill. Partition of Sr, Ba, Ca, Y, Eu²⁺, Eu³⁺, and other REE between plagioclase feldspar and magmatic liquid: an experimental study. *Geochimica et Cosmochimica Acta*, 39(5):689–712, 1975.

M.J. Dudas, R.A. Schmitt, and M.E. Harward. Trace element partitioning between volcanic plagioclase and dacitic pyroclastic matrix. *Earth and Planetary Science Letters*, 11(1):440–446, 1971.

Todd Dunn and Cuneyt Sen. Mineral/matrix partition coefficients for orthopyroxene, plagioclase, and olivine in basaltic to andesitic systems: A combined analytical and experimental study. *Geochimica et Cosmochimica Acta*, 58(2):717–733, 1994.

S.M Eggins, R.L Rudnick, and W.F McDonough. The composition of peridotites and their minerals: a laser-ablation ICP MS study. *Earth and Planetary Science Letters*, 154(1):53–71, 1998.

J Godfrey Fitton. Does depleted mantle form an intrinsic part of the Iceland plume? *Geochemistry Geophysics Geosystems*, 4(3), 2003.

M S Ghiorso, Marc M. Hirschmann, P W Reiners, and V C Kress. The pMELTS: a revision of MELTS for improved calculation of phase relations and major element partitioning related to partial melting of the mantle to 3 GPa. *Geochemistry Geophysics Geosystems*, 3(5):1030, 2002.

A A Gurenko and M Chaussidon. Enriched and depleted primitive melts included in Olivine from Icelandic tholeiites – Origin by melting of a single manlte column. *Geochimica et Cosmochimica Acta*, 59(14):2905–2917, July 1995.

Andrey a. Gurenko and Alexander V. Sobolev. Crust-primitive magma interaction beneath neovolcanic rift zone of Iceland recorded in gabbro xenoliths from Midfell, SW Iceland. *Contributions to Mineralogy and Petrology*, 151(5):495–520, March 2006.

Erik H. Hauri. Major-element variability in the Hawaiian mantle plume. *Nature*, 382(6590):415–419, August 1996.

Claude Herzberg, Paul D Asimow, Dmitri A Ionov, Chris Vidito, Matthew G Jackson, and Dennis Geist. Nickel and helium evidence for melt above the core-mantle boundary. *Nature*, 493(7432):393–7, January 2013.

C. Herzberg. Plume-Associated Ultramafic Magmas of Phanerozoic Age. *Journal of Petrology*, 43(10):1857–1883, October 2002.

Claude Herzberg. Identification of source lithology in the Hawaiian and Canary Islands: Implications for origins. *Journal of Petrology*, 52(1):113–146, 2011.

Albrecht W. Hofmann and William M. White. Mantle plumes from ancient oceanic crust. *Earth and Planetary Science Letters*, 57(2):421–436, 1982.

Garrett Ito, Jian Lin, and Carl W Gable. Dynamics of mantle flow and melting at a ridge-centered hotspot: Iceland and the Mid-Atlantic Ridge. *Earth and Planetary Science Letters*, 144(1-2):53–74, October 1996.

Richard F Katz, Marc Spiegelman, and Charles H Langmuir. A new parametrization of hydrous mantle melting. *Geochemistry, Geophysics and Geosystems*, 4(9), 2003.

- P. B. Kelemen, G. Hirth, N. Shimizu, M. Spiegelman, and H. J. Dick. A review of melt migration processes in the adiabatically upwelling mantle beneath oceanic spreading ridges. *Philosophical Transactions of the Royal Society A: Mathematical, Physical and Engineering Sciences*, 355(1723):283–318, February 1997.
- L. H. Kellogg. Compositional Stratification in the Deep Mantle. *Science*, 283(5409):1881–1884, March 1999.
- Jun Korenaga and Peter B. Kelemen. Major element heterogeneity in the mantle source of the North Atlantic igneous province. *Earth and Planetary Science Letters*, 184(1):251–268, 2000.
- V. Le Roux, R. Dasgupta, and C.-T.A. Lee. Mineralogical heterogeneities in the Earth’s mantle: Constraints from Mn, Co, Ni and Zn partitioning during partial melting. 2011.
- John Longhi. Some phase equilibrium systematics of lherzolite melting: I. *Geochemistry, Geophysics, Geosystems*, 3(3):1–33, March 2002.
- John MacLennan, Dan McKenzie, and K. Gronvöld. Plume-driven upwelling under central Iceland. *Earth and Planetary Science Letters*, 194(1-2):67–82, December 2001.
- J. MacLennan. Concurrent Mixing and Cooling of Melts under Iceland. *Journal of Petrology*, 49(11):1931–1953, November 2008.
- John MacLennan. Lead isotope variability in olivine-hosted melt inclusions from Iceland. *Geochimica et Cosmochimica Acta*, 72(16):4159–4176, 2008.
- A. K. Matzen, M. B. Baker, J. R. Beckett, and E. M. Stolper. The Temperature and Pressure Dependence of Nickel Partitioning between Olivine and Silicate Melt. *Journal of Petrology*, pages egt055–, October 2013.
- Dan McKenzie and M J Bickle. The volume and Composition of Melt Generated by Extension of the Lithosphere. *Journal of Petrology*, 29:625–679, 1988.
- D. McKenzie. The Generation and Compaction of Partially Molten Rock. *Journal of Petrology*, 25(3):713–765, August 1984.
- D.W. Peate, K. Breddam, J.A. Baker, M.D. Kurz, A.K. Barker, T. Prestvik, N. Grassineau, and A.C. Skovgaard. Compositional characteristics and spatial distribution of enriched Icelandic mantle components. *Journal of Petrology*, 51(7):1447, 2010.
- Maik Pertermann and Marc M. Hirschmann. Partial melting experiments on a MORB-like pyroxenite between 2 and 3 GPa: Constraints on the presence of pyroxenite in the basalt source regions from solidus location and melting rate. *Journal of Geophysical Research*, 108(B2), 2003.
- W.C Phinney and D.A Morrison. Partition coefficients for calcic plagioclase: Implications for Archean anorthosites. *Geochimica et Cosmochimica Acta*, 54(6):1639–1654, 1990.
- Jason Phipps Morgan. Thermodynamics of pressure release melting of a veined plum pudding mantle. *Geochemistry Geophysics Geosystems*, 2(4), April 2001.
- Keith Putirka, F J Ryerson, Michael Perfit, and W Ian Ridley. Mineralogy and composition of the oceanic mantle. *Journal of Petrology*, 52(2):279–313, 2011.

- K. D. Putirka. Thermometers and Barometers for Volcanic Systems. *Reviews in Mineralogy and Geochemistry*, 69(1):61–120, January 2008.
- C. Richardson and D. McKenzie. Radioactive disequilibria from 2D models of melt generation by plumes and ridges. *Earth and Planetary Science Letters*, 128(3):425–437, 1994.
- J. Andrew C. Robinson and Bernard J. Wood. The depth of the spinel to garnet transition at the peridotite solidus. *Earth and Planetary Science Letters*, 164(1):277–284, 1998.
- Vincent J. M. Salters and Andreas Stracke. Composition of the depleted mantle. *Geochemistry Geophysics Geosystems*, 5(5):Q05B07, May 2004.
- Henrik Schiellerup. Generation and equilibration of olivine tholeiites in the northern rift zone of Iceland. A petrogenetic study of Bláfjall table mountain. *Journal of Volcanology and Geothermal Research*, 65:161–179, 1995.
- Denis Martin Shaw. *Trace Elements in Magmas: A Theoretical Treatment*. Cambridge University Press, 2006.
- O. Shorttle and J. MacLennan. Compositional trends of Icelandic basalts: Implications for short-length scale lithological heterogeneity in mantle plumes. *Geochemistry, Geophysics, Geosystems*, 12(11):n/a–n/a, November 2011.
- Alexander V Sobolev, Albrecht W. Hofmann, Stephan V Sobolev, and Igor K Nikogosian. An olivine-free mantle source of Hawaiian shield basalts. *Nature*, 434:412–417, 2005.
- A.V. Sobolev, Albrecht W. Hofmann, D.V. Kuzmin, G.M. Yaxley, Nicholas T. Arndt, S.L. Chung, L.V. Danyushevsky, Tim Elliott, F.A. Frey, M.O. Garcia, and Others. The amount of recycled crust in sources of mantle-derived melts. *Science*, 316(5823):412, 2007.
- Andreas Stracke, Michael Bizimis, and Vincent J. M. Salters. Recycling oceanic crust: Quantitative constraints. *Geochemistry, Geophysics, Geosystems*, 4(3):n/a–n/a, March 2003.
- Andreas Stracke, Albrecht W. Hofmann, and Stan R. Hart. FOZO, HIMU, and the rest of the mantle zoo. *Geochemistry, Geophysics, Geosystems*, 6(5):n/a–n/a, May 2005.
- Eiichi Takahashi. Melting of a dry peridotite KLB-1 up to 14 GPa: Implications on the Origin of peridotitic upper mantle. *Journal of Geophysical Research*, 91(B9):9367, 1986.
- A. Thomson and J. MacLennan. The Distribution of Olivine Compositions in Icelandic Basalts and Picrites. *Journal of Petrology*, pages egs083–, December 2012.
- M. J. Toplis. The thermodynamics of iron and magnesium partitioning between olivine and liquid: criteria for assessing and predicting equilibrium in natural and experimental systems. *Contributions to Mineralogy and Petrology*, 149(1):22–39, November 2004.
- Michael J Walter. Melting of Garnet Peridotite and the Origin of Komatiite and Depleted Lithosphere. *Journal of Petrology*, 39(1):29–60, 1998.
- Laura E Wasylenki, Michael B Baker, Adam J R Kent, and Edward M Stolper. Near-solidus melting of the shallow upper mantle: Partial melting experiments on depleted peridotite. *Journal of Petrology*, 44(7):1163–1191, 2003.

S. Watson and D. McKenzie. Melt Generation by Plumes: A Study of Hawaiian Volcanism. *Journal of Petrology*, 32(3):501–537, June 1991.

Robert S. White, Julian Drew, Hilary R. Martens, Janet Key, Heidi Soosalu, and Steinunn S. Jakobsdóttir. Dynamics of dyke intrusion in the mid-crust of Iceland. 2011.

Rhea K Workman and Stanley R Hart. Major and trace element composition of the depleted MORB mantle (DMM). *Earth and Planetary Science Letters*, 231(1-2):53–72, February 2005.

Gregory M Yaxley and David H Green. Reactions between eclogite and peridotite: mantle refertilisation by subduction of oceanic crust. *Contributions to Mineralogy and Petrology*, 139:326–338, 2000.

Alan Zindler and Stan Hart. Helium: problematic primordial signals. *Earth and Planetary Science Letters*, 79(1):1–8, 1986.

9 Acknowledgements

- Thanks to my supervisor John Maclennan who gave invaluable guidance and constructive criticism throughout this project.
- Thanks to John Maclennan, Oliver Shorttle and Margaret Hartley who provided an introduction to the field geology of Iceland and instructed in sample collection during fieldwork in Summer 2013.
- Oliver Shorttle collected and prepared the olivine crystals from Hreggnasi for electron microprobe analysis.
- Ben Winpenney collected the samples from Kistufell.
- Martin Walker helped make the epoxy mounts.
- David Neave gave much-appreciated guidance when polishing samples and also instructed in the use of Linux-based software.
- Iris Buisman gave support with the electron microprobe.
- Fieldwork in Summer 2013 was funded by Pembroke College and the Cambridge University Spencer fund.

10 Self-Assesment

I choose this project because it offered the prospect of developing a broad skill-set- involving both labwork and computing and the opportunity to do fieldwork in Iceland. The project also stood out as it had a clear objective which had potentially important repercussions on a topical area of research.

The fieldwork in Iceland over the summer was really enjoyable. John and Oli Shorttle were brilliant company in the field and gave a lot of guidance. I feel that visiting the field area and collecting my own samples gave me a deeper understanding of Icelandic geology and also enhanced my enthusiasm for the project.

I decided to prepare my own samples for microprobe analysis. This was very time-consuming and took up over two weeks. Despite this I felt it was useful to learn the techniques, and I could now prepare the samples a lot more efficiently.

The incorrect set-up used for the first two days on the probe meant that all data measured in these sessions were discarded losing me a full week of work. Thankfully I managed to get an extra day on the probe meaning that although some time was wasted, all the high-quality data required for the rest of the project was obtained in the end.

Having no previous experience coding or using matlab, the learning curve for the model-development was steep. Throwing myself in at the deep end meant that I learnt the necessary skills very fast, however it also meant that the model was built on shaky foundations. I found myself continually back-tracking and restructuring the code as the model became more complex.

The initial aim was to develop a bi-lithologic melting model to directly explore the involvement of lithologic heterogeneities in mantle melting. Due to the time-constraints I decided to limit the model to melting of a single lithology. This was also in part a pragmatic decision. The partitioning data available in the literature for pyroxenite melting is sparse and it would have been almost impossible to parameterise the major element melt composition without relying on a thermodynamic model such as MELTs. The model would therefore have been unreliable at best. Focussing on peridotite melting, for which there is a large body of relevant literature, meant I could explore the effects of different variables on the melting systematics more thoroughly. The outcome of this is a model which I am confident gives physically meaningful results. Despite this I plan to continue developing a bi-lithologic model in the future.

The large undertaking of building the melting model from scratch meant that I did not have time to delve into the relevant literature to the extent I would have liked. The majority of the reading I did was focussed on getting up-to-date model parameters, rather than on the general arguments surrounding major and trace element heterogeneity of the mantle. Not having time to form a more well-rounded view on this topic is one of my regrets of the project.

To summarise, working on this project has been a very positive experience. John has been a great supervisor- very enthusiastic and always prepared to give advice. The project was perhaps overly ambitious, but I feel I have done justice to its core aims. Over and above the scientific results, I think the most valuable aspect of this project is the varied skillset that I have gained. Many of these skills, in particular those gained from the computing and lab-based work will be very useful for future research.

A Project Proposal

C2

Topic: Minor element variations in Icelandic olivines: Source or process controlled?

Supervisor: John Maclennan

Aims A number of high-profile recent publications have used the minor element contents of olivines contained in primitive basalts to infer the presence of large quantities of recycled basaltic material in their mantle source regions. Surprisingly, in locations such as Hawaii and the Siberian Traps, a growing number of researchers are taking the view that the dominant sources for the magmatism are olivine-poor pyroxenites rather than peridotites. This view is driven by an interpretation of measurements of the Ni and Mn contents of olivines that is founded upon a number of assumptions regarding the partitioning behaviour of such minor elements during mantle melting. The aim of the project is to assess the diversity of minor element contents of olivines in Icelandic samples and then to evaluate whether this variation can be accounted for by changes in the physical conditions of mantle melting alone, or if the spread in the olivines composition requires mineralogical heterogeneity in the mantle source regions.

Methods A large dataset of Icelandic olivine compositions has previously been compiled and it is hoped that, by sampling and subsequent micro-analysis, the student will be able to add a significant amount of high-quality data to this compilation. The student will build models in order to link variation in the physical conditions of melting, mantle mineralogy, and olivine crystallisation to observed olivine compositions. They will use the results of a number of new partitioning studies in order to build these models. By comparison of the model results with the observations, it is hoped that they will be able to distinguish the effects of source heterogeneity and melting.

Logistics If the student wishes to undertake fieldwork in Iceland, that will take place in the summer of 2013, at localities decided in discussion with the supervisor. Sample preparation and electron probe microanalysis will take place in the Department, with guidance from technical experts. The development of the models will require the student to learn to code in a suitable language, probably MATLAB, and the supervisor will assist with those choices.

Finance Funding for fieldwork may be partly obtained by the student. Support for related summer work in the Harker Collection may also be available. Funds are available to support the sample preparation and micro-analysis. Database manipulation and model development have no costs.

Reading List

- Sobolev et al., (2007). The Amount of Recycled Crust in Sources of Mantle-Derived Melts, Science, 316, 412-417. Herzberg, C. (2011). Identification of Source Lithology in the Hawaiian and Canary Islands: Implications for Origins. Journal of Petrology 52, 113-146.
- Shorttle, Oliver and Maclennan, John (2011) Compositional trends of Icelandic basalts: Implications for short-lengthscale lithological heterogeneity in mantle plumes. Geochemistry Geophysics Geosystems, 12 . Q11008.

B Major and trace element data

Midfell

Ref	Fo	SiO ₂	TiO ₂	Cr ₂ O ₃	Al ₂ O ₅	FeO*	MnO	NiO	MgO	CaO	P ₂ O ₅	Total
ol6A	88.9(4)	40.8(3)	0.005(24)	0.08(3)	0.069(8)	10.7(2)	0.176(13)	0.313(15)	47.8(4)	0.363(12)	0.010(10)	100.32
ol1A	89.0(4)	40.9(3)	0.010(18)	0.10(3)	0.055(7)	10.5(2)	0.163(13)	0.262(15)	47.9(4)	0.382(12)	0.005(6)	100.27
ol2A	89.1(4)	40.9(3)	0.015(18)	0.08(3)	0.080(8)	10.5(2)	0.155(13)	0.318(16)	47.9(4)	0.329(11)	0.014(6)	100.24
ol3A	86.7(4)	40.7(3)	0.019(18)	0.07(3)	0.067(8)	12.7(3)	0.181(14)	0.251(15)	46.5(4)	0.357(12)	0.011(6)	100.82
ol4A	89.1(4)	40.9(3)	0.014(26)	0.06(3)	0.065(8)	10.5(2)	0.150(13)	0.312(16)	47.9(4)	0.374(12)	0.006(6)	100.28
ol5A	90.5(3)	41.2(3)	0.024(26)	0.10(3)	0.068(7)	9.2(2)	0.142(13)	0.314(15)	49.2(4)	0.360(12)	0.011(6)	100.62
ol7A	87.1(4)	40.6(3)	0.019(18)	0.05(3)	0.067(7)	12.3(3)	0.194(14)	0.232(14)	46.6(4)	0.345(11)	0.003(7)	100.45
ol8A	90.7(3)	41.3(3)	0.002(25)	0.11(3)	0.072(8)	9.0(2)	0.146(13)	0.318(15)	49.1(4)	0.372(12)	0.011(6)	100.45
ol9A	88.2(4)	40.8(3)	0.006(18)	0.04(3)	0.075(7)	11.3(3)	0.168(13)	0.261(15)	47.7(4)	0.362(12)	0.010(7)	100.73
ol10A	86.8(4)	40.6(3)	0.014(26)	0.07(3)	0.059(7)	12.5(3)	0.186(14)	0.263(15)	46.4(4)	0.345(11)	0.014(7)	100.54
ol11A	87.1(4)	40.6(3)	0.007(25)	0.08(3)	0.065(8)	12.3(3)	0.192(14)	0.232(15)	46.7(4)	0.353(12)	0.007(6)	100.50
ol12A	89.5(4)	40.9(3)	0.012(18)	0.10(3)	0.078(8)	10.1(2)	0.161(13)	0.337(16)	48.2(4)	0.360(12)	0.030(6)	100.29
ol13A	85.9(4)	40.4(3)	0.014(18)	0.03(2)	0.053(7)	13.4(3)	0.205(14)	0.222(14)	45.8(4)	0.356(12)	0.004(6)	100.44
ol14A	87.5(4)	40.6(3)	0.026(25)	0.06(3)	0.054(7)	11.9(3)	0.183(14)	0.282(15)	46.8(4)	0.362(12)	0.011(7)	100.32
ol15A	87.6(4)	40.7(3)	0.021(15)	0.04(3)	0.056(7)	11.9(3)	0.177(13)	0.272(15)	47.1(4)	0.360(12)	0.008(6)	100.56
ol16A	86.9(4)	40.5(3)	0.013(25)	0.05(2)	0.064(8)	12.5(3)	0.192(14)	0.238(14)	46.5(4)	0.346(12)	0.013(6)	100.45
ol17A	86.4(4)	40.6(3)	0.015(15)	0.05(3)	0.049(8)	13.0(3)	0.200(14)	0.225(14)	46.3(4)	0.353(12)	0.007(6)	100.75
ol18A	87.2(4)	40.5(3)	0.000	0.04(3)	0.061(7)	12.3(3)	0.179(13)	0.272(15)	46.8(4)	0.379(12)	0.004(7)	100.45
ol19A	89.9(3)	41.1(3)	0.014(18)	0.08(3)	0.076(8)	9.7(2)	0.152(13)	0.341(16)	48.6(4)	0.357(12)	0.020(10)	100.48
ol20A	88.8(4)	40.6(3)	0.014(18)	0.07(3)	0.067(8)	10.8(2)	0.170(13)	0.289(15)	47.6(4)	0.391(12)	0.012(10)	100.06

Table 10: Electron microprobe data for Midfell olivines reported as wt% oxides. FeO* assumes all Fe present as FeO. Fo=100MgO/(MgO+FeO*) on a molar basis. These are average concentrations of three point measurements taken for each olivine. Numbers in parentheses adjacent to each oxide value are one sample standard deviation in terms of the least units cited, e.g. 40.6(4) represents 40.6 ± 0.4 . Dashes indicate that the element was not analysed or was below the detection limit of the microprobe.

Midfell (continued)

Ref	Fo	SiO ₂	TiO ₂	Cr ₂ O ₃	Al ₂ O ₅	FeO*	MnO	NiO	MgO	CaO	P ₂ O ₅	Total
ol1B	86.4(5)	40.3(3)	0.009(15)	0.043(15)	0.063(2)	12.8(3)	0.193(12)	0.220(9)	45.6(4)	0.354(7)	-	99.61
ol2B	89.9(4)	40.9(3)	0.008(22)	0.106(17)	0.078(2)	9.6(3)	0.153(12)	0.320(11)	48.1(4)	0.349(7)	-	99.61
ol3aB	89.1(4)	40.7(3)	0.004(16)	0.079(16)	0.059(2)	10.3(3)	0.157(12)	0.301(10)	47.5(4)	0.357(7)	-	99.51
ol4B	87.4(5)	40.6(3)	0.019(15)	0.057(16)	0.067(2)	12.0(3)	0.179(12)	0.240(9)	46.4(4)	0.345(7)	-	99.89
ol5B	86.9(5)	40.5(3)	0.018(21)	0.040(15)	0.050(2)	12.4(3)	0.195(12)	0.225(9)	46.1(4)	0.349(7)	-	99.87
ol6B	87.0(5)	40.4(3)	0.015(22)	0.054(16)	0.061(2)	12.2(3)	0.192(12)	0.234(9)	45.9(4)	0.337(7)	-	99.45
ol7B	87.8(4)	40.6(3)	0.015(13)	0.069(16)	0.065(2)	11.5(3)	0.172(12)	0.261(10)	46.7(4)	0.356(8)	-	99.77
ol8B	89.0(4)	40.8(3)	0.013(13)	0.132(17)	0.103(2)	10.5(3)	0.156(12)	0.331(11)	47.4(4)	0.363(8)	-	99.81
ol10B	86.9(5)	40.5(3)	0.017(21)	0.070(16)	0.069(2)	12.3(3)	0.200(12)	0.248(10)	46.0(4)	0.343(7)	-	99.76
ol11B	91.3(4)	41.2(3)	0.019(13)	0.102(17)	0.087(2)	8.3(2)	0.148(11)	0.394(12)	49.0(4)	0.358(8)	-	99.69
ol9B	85.7(5)	40.4(3)	0.009(16)	0.042(15)	0.050(2)	13.4(4)	0.212(13)	0.208(9)	45.1(4)	0.361(8)	-	99.75
ol12B	88.3(4)	40.6(3)	0.025(15)	0.082(16)	0.068(2)	11.1(3)	0.177(12)	0.277(10)	46.9(4)	0.366(8)	-	99.62
ol13B	88.8(4)	40.7(3)	0.005(15)	0.072(16)	0.066(2)	10.6(3)	0.172(12)	0.280(10)	47.2(4)	0.399(8)	-	99.52
ol14B	86.5(5)	40.4(3)	0.014(12)	0.047(15)	0.053(2)	12.7(3)	0.193(12)	0.219(9)	45.6(4)	0.370(8)	-	99.62
ol15B	86.4(5)	40.5(3)	0.016(15)	0.057(16)	0.067(2)	12.8(3)	0.199(13)	0.229(9)	45.6(4)	0.362(8)	-	99.80
ol16B	89.1(4)	40.9(3)	0.027(15)	0.053(16)	0.060(2)	10.3(3)	0.167(12)	0.271(10)	47.5(4)	0.379(8)	-	99.65
ol17B	86.3(5)	40.3(3)	0.008(15)	0.039(15)	0.051(2)	13.0(3)	0.212(13)	0.221(9)	45.7(4)	0.356(8)	-	99.85
ol18B	86.4(5)	40.4(3)	0.020(15)	0.034(15)	0.049(2)	12.9(3)	0.192(12)	0.238(10)	45.8(4)	0.354(7)	-	99.88
ol19B	87.0(5)	40.5(3)	0.006(16)	0.044(16)	0.049(2)	12.2(3)	0.192(13)	0.233(10)	46.1(4)	0.366(8)	-	99.74

Table 11: Electron microprobe data for Midfell olivines (continued)

Stapafell

Ref	Fo	SiO ₂	TiO ₂	Cr ₂ O ₃	Al ₂ O ₅	FeO*	MnO	NiO	MgO	CaO	P ₂ O ₅	Total
ol1A	82.6(5)	39.8(3)	0.014(13)	0.020(15)	0.039(2)	16.1(4)	0.263(14)	0.171(9)	43.1(4)	0.299(7)	-	99.82
ol2A	86.0(5)	40.3(3)	0.018(16)	0.028(15)	0.046(2)	13.2(3)	0.205(13)	0.215(9)	45.5(4)	0.269(6)	-	99.77
ol7A	87.1(5)	40.6(3)	0.014(16)	0.044(16)	0.044(2)	12.2(3)	0.188(12)	0.265(10)	46.3(4)	0.270(6)	-	99.93
ol6A	86.9(5)	40.4(3)	0.013(13)	0.055(16)	0.052(2)	12.4(3)	0.197(12)	0.278(10)	46.2(4)	0.278(6)	-	99.90
ol5A	83.3(5)	39.8(3)	0.005(16)	0.038(15)	0.038(2)	15.6(4)	0.250(14)	0.226(9)	43.6(4)	0.277(6)	-	99.78
ol4A	79.7(6)	39.2(3)	0.005(16)	0.005(15)	0.037(2)	18.7(5)	0.307(15)	0.140(8)	41.1(4)	0.294(7)	-	99.74
ol3A	85.5(5)	40.2(3)	0.028(21)	0.054(16)	0.049(2)	13.7(4)	0.206(13)	0.246(10)	45.3(4)	0.265(6)	-	99.97
ol8A	85.7(5)	40.2(3)	0.013(13)	0.046(15)	0.048(2)	13.5(4)	0.199(12)	0.222(9)	45.3(4)	0.268(6)	-	99.86
ol9A	87.3(5)	40.5(3)	0.011(16)	0.063(16)	0.049(2)	12.1(3)	0.194(12)	0.258(10)	46.5(4)	0.252(6)	-	99.89
ol10A	85.7(5)	40.0(3)	0.009(22)	0.062(16)	0.048(2)	13.5(4)	0.199(12)	0.253(10)	45.5(4)	0.281(6)	-	99.89
ol11A	85.5(5)	40.1(3)	0.007(16)	0.026(15)	0.045(2)	13.7(4)	0.205(13)	0.233(9)	45.2(4)	0.257(6)	-	99.77
ol12A	85.2(5)	39.9(3)	0.020(13)	0.065(16)	0.051(2)	13.9(4)	0.210(13)	0.255(10)	44.9(4)	0.286(6)	-	99.62
ol13A	87.7(5)	40.5(3)	0.017(15)	0.062(16)	0.051(2)	11.7(3)	0.176(12)	0.287(10)	46.8(4)	0.281(6)	-	99.76
ol22A	83.7(5)	39.7(3)	0.022(13)	0.047(16)	0.040(2)	15.2(4)	0.245(13)	0.225(9)	43.8(4)	0.288(6)	-	99.62
ol18A	87.0(5)	40.2(3)	0.021(12)	0.068(16)	0.042(2)	12.4(3)	0.192(12)	0.291(10)	46.3(4)	0.289(6)	-	99.75
ol17A	85.3(5)	40.0(3)	0.010(16)	0.035(15)	0.044(2)	13.9(4)	0.206(13)	0.232(9)	45.1(4)	0.272(6)	-	99.78
ol16A	85.5(5)	40.0(3)	0.023(13)	0.021(15)	0.043(2)	13.6(4)	0.211(13)	0.225(9)	45.2(4)	0.244(6)	-	99.56
ol15A	87.5(5)	40.2(3)	0.011(15)	0.054(16)	0.045(2)	11.9(3)	0.191(12)	0.280(10)	46.4(4)	0.251(6)	-	99.23
ol14A	86.4(5)	40.1(3)	0.007(15)	0.056(15)	0.051(2)	12.9	0.198(12)	0.255(10)	45.6(4)	0.267(6)	-	99.34
ol19A	85.8(5)	39.9(3)	0.014(16)	0.049(16)	0.052(2)	13.4(4)	0.202(12)	0.270(10)	45.3(4)	0.283(6)	-	99.46
ol20A	86.3(5)	40.0(3)	0.021(22)	0.068(16)	0.048(2)	13.0(3)	0.198(12)	0.279(10)	45.7(4)	0.275(6)	-	99.57
ol21A	87.1(5)	40.2(3)	0.018(16)	0.050(16)	0.053(2)	12.2(3)	0.191(12)	0.295(10)	46.1(4)	0.274(6)	-	99.41
ol23A	86.9(5)	40.2(3)	0.006(22)	0.055(16)	0.048(2)	12.3(3)	0.191(12)	0.274(10)	46.1(4)	0.278(6)	-	99.43

Table 12: Electron microprobe data for Stapafell olivines reported as wt% oxides. FeO* assumes all Fe present as FeO. Fo=100MgO/(MgO+FeO*) on a molar basis. These are average concentrations of three point measurements taken for each olivine. Numbers in parentheses adjacent to each oxide value are one sample standard deviation in terms of the least units cited, e.g. 40.6(4) represents 40.6 ± 0.4 . Dashes indicate that the element was not analysed or was below the detection limit of the microprobe.

Stapafell (continued)

Ref	Fo	SiO ₂	TiO ₂	Cr ₂ O ₃	Al ₂ O ₅	FeO*	MnO	NiO	MgO	CaO	P ₂ O ₅	Total
ol1B	83.4(4)	39.9(3)	0.013(18)	0.02(2)	0.030(7)	15.7(3)	0.239(15)	0.210(14)	44.3(4)	0.251(10)	0.010(6)	100.66
ol2B	85.3(4)	40.2(3)	0.012(15)	0.06(3)	0.058(7)	14.0(3)	0.200(14)	0.253(14)	45.5(4)	0.272(10)	0.000	100.47
ol3B	83.9(4)	40.0(3)	0.019(26)	0.03(3)	0.033(7)	15.2(3)	0.232(14)	0.214(14)	44.7(4)	0.265(10)	0.010(6)	100.76
ol4B	85.8(5)	40.4(3)	0.022(24)	0.04(3)	0.043(9)	13.6(4)	0.196(17)	0.234(18)	46.1(4)	0.237(12)	0.020(7)	100.98
ol5B	82.1(4)	39.7(2)	0.021(18)	0.02(2)	0.030(7)	16.9(3)	0.259(15)	0.193(14)	43.5(4)	0.239(10)	0.018(6)	100.78
ol6B	84.4(4)	40.0(3)	0.004(18)	0.03(3)	0.046(7)	14.7(3)	0.230(15)	0.227(15)	44.8(4)	0.273(11)	0.006(6)	100.36
ol7B	83.5(4)	39.9(2)	0.019(25)	0.03(3)	0.031(7)	15.6(3)	0.245(14)	0.193(14)	44.2(4)	0.289(11)	0.020(6)	100.49
ol8B	84.9(4)	40.2(3)	0.012(15)	0.03(2)	0.033(7)	14.4(3)	0.219(14)	0.255(15)	45.3(4)	0.251(10)	0.007(6)	100.67
ol9B	85.9(4)	40.3(3)	0.023(15)	0.05(3)	0.050(7)	13.5(3)	0.200(14)	0.240(14)	46.1(4)	0.287(10)	0.011(6)	100.75
ol10B	86.0(4)	40.3(3)	-	0.06(3)	0.049(7)	13.4(3)	0.200(14)	0.230(14)	46.1(4)	0.269(10)	0.014(6)	100.61
ol11B	85.4(4)	40.3(3)	0.015(18)	0.03(2)	0.037(7)	13.9(3)	0.201(14)	0.214(14)	45.5(4)	0.265(10)	0.013(11)	100.53
ol12B	85.6(4)	40.4(3)	0.014(15)	0.03(3)	0.045(7)	13.8(3)	0.207(14)	0.219(14)	45.8(4)	0.271(10)	0.009(7)	100.81
ol13B	82.3(4)	39.8(2)	0.012(15)	0.03(2)	0.033(7)	16.6(3)	0.265(15)	0.165(14)	43.5(4)	0.282(11)	0.020(11)	100.72
ol14B	87.0(4)	40.6(3)	0.007(18)	0.06(3)	0.039(7)	12.4(3)	0.187(14)	0.258(14)	46.7(4)	0.265(10)	0.009(7)	100.63
ol15B	86.4(4)	40.5(3)	0.018(18)	0.06(2)	0.043(7)	13.0(3)	0.199(14)	0.207(14)	46.4(4)	0.269(10)	0.001(7)	100.71
ol16B	82.3(4)	39.7(2)	0.019(15)	0.03(2)	0.042(7)	16.6(3)	0.255(15)	0.147(13)	43.3(4)	0.296(11)	0.027(6)	100.40
ol17B	85.6(4)	40.4(3)	0.009(15)	0.03(2)	0.046(7)	13.7(3)	0.207(14)	0.223(14)	45.7(4)	0.272(10)	0.006(7)	100.54
ol18B	85.8(4)	40.3(3)	0.031(18)	0.04(3)	0.051(7)	13.5(3)	0.207(14)	0.257(15)	45.7(4)	0.292(11)	0.007(6)	100.32
ol19B	84.8(4)	40.2(3)	0.010(18)	0.01(2)	0.049(7)	14.5(3)	0.207(15)	0.231(14)	45.3(4)	0.283(11)	0.008(7)	100.87
ol20B	85.4(4)	40.3(3)	0.023(15)	0.02(3)	0.044(7)	13.9(3)	0.199(14)	0.245(15)	45.6(4)	0.269(10)	0.032(11)	100.53
ol21B	82.0(4)	39.7(2)	0.007(18)	0.01(2)	0.040(7)	16.9(3)	0.268(15)	0.184(14)	43.2(4)	0.260(10)	0.003(10)	100.60
ol22B	84.5(4)	40.2(3)	0.010(18)	0.01(3)	0.044(8)	14.7(3)	0.223(15)	0.224(15)	44.8(4)	0.284(10)	0.007(10)	100.43

Table 13: Electron microprobe data for Stapafell olivines (continued)

Kistufell

Ref	Fo	SiO ₂	TiO ₂	Cr ₂ O ₃	Al ₂ O ₅	FeO*	MnO	NiO	MgO	CaO	Total
ol1A	88.4(4)	40.6(4)	0.004(16)	0.037(15)	0.031(2)	11.1(3)	0.167(11)	0.272(9)	47.0(8)	0.253(6)	99.48
ol2A	85.8(5)	40.2(4)	0.026(13)	0.019(15)	0.022(2)	13.4(3)	0.205(12)	0.189(8)	45.4(8)	0.153(5)	99.64
ol3A	86.5(5)	40.4(4)	0.008(13)	0.035(15)	0.050(2)	12.7(3)	0.188(11)	0.230(8)	45.7(8)	0.320(6)	99.57
ol4A	88.3(5)	40.8(4)	0.003(13)	0.015(15)	0.071(2)	11.1(3)	0.159(11)	0.246(9)	46.9(8)	0.310(6)	99.65
ol5A	88.8(4)	40.9(4)	0.014(15)	0.045(15)	0.071(2)	10.7(3)	0.160(11)	0.322(9)	47.2(8)	0.321(6)	99.70
ol6A	87.9(5)	40.6(4)	0.011(13)	0.052(16)	0.067(2)	11.4(3)	0.172(11)	0.303(9)	46.6(8)	0.326(6)	99.56
ol7A	88.6(4)	40.8(4)	0.013(16)	0.073(16)	0.060(2)	10.7(3)	0.171(11)	0.315(9)	47.0(8)	0.314(6)	99.48
ol8A	88.6(4)	40.8(4)	0.011(13)	0.049(16)	0.060(2)	10.9(3)	0.156(11)	0.307(9)	47.2(8)	0.326(6)	99.80
ol9A	87.7(5)	40.5(4)	0.015(13)	0.052(16)	0.066(2)	11.6(3)	0.173(11)	0.266(9)	46.6(8)	0.332(6)	99.64
ol10A	88.0(5)	40.8(4)	0.017(22)	0.051(16)	0.048(2)	11.3(3)	0.170(11)	0.293(9)	46.7(8)	0.322(6)	99.73
ol11A	88.2(5)	40.8(4)	-	0.050(15)	0.037(2)	11.2(3)	0.165(11)	0.295(9)	47.0(8)	0.294(6)	99.87
ol12A	88.4(5)	41.0(4)	0.008(16)	0.035(15)	0.030(2)	11.1(3)	0.165(11)	0.288(9)	47.2(8)	0.271(6)	100.02
ol13A	88.4(4)	40.7(4)	0.012(13)	0.065(16)	0.065(2)	11.0(3)	0.161(11)	0.308(9)	47.0(8)	0.312(6)	99.63
ol14A	88.5(4)	40.8(4)	0.016(16)	0.057(16)	0.060(2)	11.0(3)	0.160(11)	0.308(9)	47.1(8)	0.316(6)	99.84
ol15A	88.3(5)	40.7(4)	0.0084(15)	0.060(16)	0.066(2)	11.1(3)	0.163(11)	0.309(9)	47.1(8)	0.319(6)	99.88
ol16A	87.4(5)	40.6(4)	0.011(16)	0.043(15)	0.063(2)	11.9(3)	0.161(11)	0.306(9)	46.3(8)	0.318(6)	99.78
ol17A	88.5(4)	40.8(4)	0.015(16)	0.049(16)	0.061(2)	10.9(3)	0.160(11)	0.309(9)	47.1(8)	0.314(6)	99.72
ol18A	86.9(5)	40.5(4)	0.0224(15)	0.031(15)	0.030(2)	12.3(3)	0.183(11)	0.282(9)	45.9(8)	0.280(6)	99.58
ol19A	88.5(4)	40.7(4)	0.024(13)	0.051(16)	0.063(2)	10.9(3)	0.157(11)	0.297(9)	47.1(8)	0.319(6)	99.62
ol20A	88.59(4)	40.7(4)	0.013(13)	0.025(16)	0.057(2)	10.9(3)	0.160(11)	0.298(9)	47.1(8)	0.346(7)	99.61
ol21A	88.3(5)	40.9(4)	0.011(13)	0.045(15)	0.061(2)	11.1(3)	0.160(11)	0.292(9)	47.0(8)	0.320(6)	99.98

Table 14: Electron microprobe data for Kistufell olivines reported as wt% oxides. FeO* assumes all Fe present as FeO. Fo=100MgO/(MgO+FeO*) on a molar basis. These are average concentrations of three point measurements taken for each olivine. Numbers in parentheses adjacent to each oxide value are one sample standard deviation in terms of the least units cited, e.g. represents 40.6 ± 0.4 . Dashes indicate that the element was not analysed or was below the detection limit of the microprobe.

Kistufell (continued)

Ref	Fo	SiO ₂	TiO ₂	Cr ₂ O ₃	Al ₂ O ₅	FeO*	MnO	NiO	MgO	CaO	Total
011B	88.0(4)	40.6(3)	-	0.061(16)	0.049(2)	11.4(3)	0.172(12)	0.273(10)	46.9(4)	0.332(7)	99.79
012B	88.0(4)	40.5(3)	0.011(12)	0.055(16)	0.058(2)	11.4(3)	0.168(12)	0.307(10)	46.7(4)	0.313(7)	99.60
013B	88.1(4)	40.6(3)	0.0054(15)	0.044(15)	0.066(2)	11.3(3)	0.180(12)	0.313(11)	46.7(4)	0.312(7)	99.49
014B	88.2(4)	40.6(3)	0.011(16)	0.037(16)	0.073(2)	11.2(3)	0.176(12)	0.301(11)	46.9(4)	0.315(7)	99.63
015B	88.1(4)	40.8(3)	0.008(12)	0.040(15)	0.024(2)	11.3(3)	0.179(12)	0.297(10)	46.9(4)	0.255(6)	99.83
016B	88.1(4)	40.5(3)	0.015(22)	0.053(15)	0.065(2)	11.3(3)	0.168(12)	0.317(11)	47.0(4)	0.311(7)	99.68
017B	87.0(5)	40.5(3)	0.0154(15)	0.037(15)	0.058(2)	12.3(3)	0.189(12)	0.287(10)	46.0(4)	0.303(7)	99.61
018B	86.9(5)	40.4(3)	0.012(21)	0.047(15)	0.039(2)	12.3(3)	0.196(12)	0.282(10)	46.0(4)	0.310(7)	99.65
019B	88.2(4)	40.7(3)	0.0174(15)	0.072(16)	0.069(2)	11.3(3)	0.172(12)	0.312(11)	47.0(4)	0.314(7)	99.90
0110B	88.1(4)	40.6(3)	0.006(13)	0.047(16)	0.065(2)	11.2(3)	0.171(12)	0.313(11)	46.8(4)	0.311(7)	99.59
0111B	88.1(4)	40.7(3)	0.032(22)	0.058(16)	0.067(2)	11.3(3)	0.173(12)	0.306(11)	46.9(4)	0.313(7)	99.86
0112B	87.7(5)	40.7(3)	0.0084(15)	0.044(16)	0.065(2)	11.6(3)	0.175(12)	0.284(10)	46.5(4)	0.333(7)	99.70
0113B	87.6(5)	40.6(3)	0.009(21)	0.021(15)	0.047(2)	11.7(3)	0.174(12)	0.280(10)	46.4(4)	0.286(7)	99.57
0114B	88.1(4)	40.8(3)	0.019(13)	0.050(16)	0.060(2)	11.3(3)	0.171(12)	0.310(11)	46.8(4)	0.317(7)	99.74
0115B	88.0(4)	40.7(3)	0.0044(15)	0.061(15)	0.064(2)	11.4(3)	0.176(12)	0.297(10)	46.7(4)	0.311(7)	99.71
0116B	87.9(4)	40.7(3)	0.011(13)	0.050(16)	0.061(2)	11.4(3)	0.178(12)	0.298(10)	46.6(4)	0.317(7)	99.65
0117B	88.0(4)	40.8(3)	0.019(22)	0.038(16)	0.062(2)	11.3(3)	0.169(12)	0.308(11)	46.8(4)	0.314(7)	99.90
0118B	88.0(4)	40.7(3)	0.007(22)	0.062(15)	0.058(2)	11.3(3)	0.168(12)	0.292(10)	46.6(4)	0.315(7)	99.53
0119B	88.1(4)	40.7(3)	0.012(22)	0.054(16)	0.075(2)	11.3(3)	0.174(12)	0.291(10)	46.6(4)	0.325(7)	99.51
0120B	87.9(4)	40.7(3)	0.011(13)	0.055(16)	0.061(2)	11.5(3)	0.168(12)	0.294(10)	46.6(4)	0.313(7)	99.66

Table 15: Electron microprobe data for Kistufell olivines (continued)

Blafjall

Ref	Fo	SiO ₂	TiO ₂	Cr ₂ O ₃	Al ₂ O ₅	FeO*	MnO	NiO	MgO	P ₂ O ₅	Total
ol1A	87.6(5)	40.7(4)	0.005(13)	0.071(16)	0.067(2)	11.8(3)	0.165(11)	0.306(9)	46.6(8)	0.323(6)	-
ol2A	87.5(5)	40.6(4)	0.012(22)	0.083(16)	0.064(2)	11.9(3)	0.176(11)	0.315(9)	46.4(8)	0.308(6)	-
ol3A	87.4(6)	40.6(4)	0.009(16)	0.068(20)	0.098(3)	12.0(3)	0.182(14)	0.334(11)	46.4(10)	0.292(7)	-
ol4A	88.2(5)	40.6(4)	0.001(15)	0.022(15)	0.053(2)	11.3(3)	0.162(11)	0.254(9)	47.2(8)	0.301(6)	-
ol5A	85.8(5)	40.3(4)	0.014(22)	0.003(14)	0.074(2)	13.4(3)	0.207(12)	0.163(8)	45.4(8)	0.295(6)	-
ol6A	83.4(5)	39.9(3)	0.014(16)	0.043(15)	0.043(2)	15.6(3)	0.239(12)	0.187(8)	43.9(8)	0.197(5)	-
ol7A	78.9(6)	39.1(3)	0.020(13)	0.042(15)	0.057(2)	19.4(4)	0.298(13)	0.170(8)	40.5(7)	0.319(6)	-
ol8A	88.0(5)	40.7(4)	0.002(22)	0.083(16)	0.064(2)	11.4(3)	0.162(11)	0.311(9)	46.9(8)	0.329(6)	-
ol9A	88.1(5)	40.8(4)	0.009(13)	0.100(16)	0.070(2)	11.4(3)	0.163(11)	0.335(9)	47.2(8)	0.319(6)	-
ol10A	87.0(5)	40.5(4)	0.008(15)	0.048(16)	0.046(2)	12.3(3)	0.177(11)	0.255(9)	46.5(8)	0.260(6)	-
ol11A	88.3(5)	40.8(4)	0.021(15)	0.097(16)	0.065(2)	11.1(3)	0.161(11)	0.334(9)	47.1(8)	0.319(6)	-
ol12A	84.0(5)	40.1(4)	0.003(16)	0.027(15)	0.042(2)	15.1(3)	0.221(12)	0.203(8)	44.4(8)	0.185(5)	-
ol13A	81.8(6)	39.7(3)	0.008(16)	0.046(15)	0.076(2)	16.9(4)	0.244(12)	0.189(8)	42.6(7)	0.315(6)	-
ol14A	87.7(5)	40.6(4)	0.015(22)	0.082(16)	0.073(2)	11.7(3)	0.168(11)	0.311(9)	46.6(8)	0.331(6)	-
ol15A	86.6(5)	40.6(4)	0.003(22)	0.066(16)	0.066(2)	12.7(3)	0.180(11)	0.276(9)	45.9(8)	0.307(6)	-
ol16A	78.0(6)	39.0(3)	0.025(13)	0.024(15)	0.070(2)	20.1(4)	0.308(13)	0.159(8)	39.8(7)	0.323(6)	-
ol17A	88.3(5)	40.7(4)	0.010(13)	0.076(16)	0.069(2)	11.1(3)	0.168(11)	0.318(9)	46.9(8)	0.331(6)	-
ol18A	84.5(5)	40.1(4)	0.018(13)	0.024(15)	0.043(2)	14.5(3)	0.220(11)	0.192(8)	44.3(8)	0.228(5)	-
ol19A	88.6(4)	40.8(4)	-	0.091(17)	0.081(2)	10.8(3)	0.152(11)	0.338(9)	47.3(8)	0.327(6)	-
ol20A	89.5(4)	41.0(4)	0.013(13)	0.087(16)	0.089(2)	10.1(2)	0.149(11)	0.361(10)	48.1(8)	0.281(6)	-

Table 16: Electron microprobe data for Blafjall olivines reported as wt% oxides. FeO* assumes all Fe present as FeO. Fo=100MgO/(MgO+FeO*) on a molar basis. These are average concentrations of three point measurements taken for each olivine. Numbers in parentheses adjacent to each oxide value are one sample standard deviation in terms of the least units cited, e.g. 40.6(4) represents 40.6 ± 0.4 . Dashes indicate that the element was not analysed or was below the detection limit of the microprobe.

Blaafjall (continued)

Ref	Fo	SiO ₂	TiO ₂	Cr ₂ O ₃	Al ₂ O ₅	FeO*	MnO	NiO	MgO	CaO	P ₂ O ₅	Total
ol1B	84.1(4)	40.2(3)	0.017(15)	0.07(3)	0.066(8)	15.0(3)	0.205(14)	0.271(15)	44.4(4)	0.306(11)	0.009(6)	100.51
ol2B	88.1(4)	41.0(3)	0.009(18)	0.09(3)	0.118(8)	11.4(3)	0.175(14)	0.311(16)	47.3(4)	0.363(12)	0.008(7)	100.69
ol3B	86.4(4)	40.6(3)	0.006(18)	0.04(2)	0.059(7)	12.9(3)	0.201(14)	0.209(14)	46.1(4)	0.308(11)	0.014(6)	100.52
ol4B	87.6(4)	40.8(3)	0.006(18)	0.10(3)	0.080(8)	11.9(3)	0.162(14)	0.312(16)	46.9(4)	0.317(11)	0.013(10)	100.63
ol5B	86.0(4)	40.6(3)	0.012(18)	0.05(3)	0.072(8)	13.2(3)	0.197(14)	0.253(15)	45.5(4)	0.310(11)	0.012(6)	100.23
ol6B	87.5(4)	40.9(3)	-	0.08(3)	0.075(8)	12.0(3)	0.170(14)	0.317(16)	47.0(4)	0.304(11)	0.010(7)	100.77
ol7B	83.1(4)	40.0(3)	0.012(18)	0.04(3)	0.080(8)	15.9(3)	0.231(14)	0.212(14)	43.7(4)	0.293(11)	0.013(7)	100.49
ol8B	87.0(4)	40.7(3)	0.011(15)	0.07(3)	0.070(8)	12.4(3)	0.170(14)	0.278(15)	46.5(4)	0.312(11)	0.005(6)	100.50
ol9B	86.1(4)	40.6(3)	0.023(18)	0.07(3)	0.068(8)	13.2(3)	0.183(14)	0.284(15)	45.8(4)	0.309(11)	0.003(6)	100.53
ol10B	84.9(4)	40.4(3)	0.011(18)	0.02(2)	0.048(7)	14.3(3)	0.205(14)	0.207(14)	45.1(4)	0.266(10)	0.013(6)	100.51
ol11B	87.0(4)	40.7(3)	0.016(15)	0.07(3)	0.079(8)	12.3(3)	0.174(14)	0.289(15)	46.4(4)	0.290(11)	0.013(6)	100.38
ol12B	81.7(4)	39.9(3)	0.018(18)	0.01(2)	0.043(7)	17.1(3)	0.252(15)	0.191(14)	42.9(4)	0.169(9)	0.012(6)	100.62
ol13B	87.3(4)	40.8(3)	0.012(14)	0.07(3)	0.084(8)	12.1(3)	0.169(14)	0.276(15)	46.6(4)	0.322(11)	0.006(6)	100.35
ol14B	79.4(5)	39.5(3)	0.015(18)	0.01(2)	0.051(7)	19.0(4)	0.254(15)	0.170(14)	41.2(3)	0.174(9)	0.005(8)	100.34
ol16B	83.3(4)	40.3(3)	0.007(25)	0.01(2)	0.040(7)	15.7(3)	0.233(15)	0.193(14)	43.9(4)	0.160(9)	0.014(7)	100.66
ol17B	87.0(4)	40.9(3)	0.018(18)	0.07(3)	0.059(8)	12.4(3)	0.181(14)	0.295(15)	46.4(4)	0.309(11)	0.011(7)	100.60
ol18B	86.8(4)	40.8(3)	-	0.02(2)	0.046(7)	12.6(3)	0.179(14)	0.223(14)	46.4(4)	0.271(10)	0.009(6)	100.46
ol19B	87.5(4)	40.8(3)	0.011(18)	0.07(3)	0.078(8)	12.0(3)	0.177(14)	0.312(16)	46.8(4)	0.304(11)	0.008(7)	100.61
ol20B	85.7(4)	40.6(3)	0.011(18)	0.04(2)	0.037(7)	13.6(3)	0.194(14)	0.226(14)	45.7(4)	0.242(10)	0.013(6)	100.70
ol21B	83.5(4)	40.2(3)	0.008(18)	0.02(2)	0.055(7)	15.6(3)	0.237(15)	0.186(14)	44.2(4)	0.216(10)	0.008(6)	100.70

Table 17: Electron microprobe data for Blaafjall olivines (continued)

Hreggnasi

Ref	Fo	SiO ₂	TiO ₂	Cr ₂ O ₃	Al ₂ O ₅	FeO*	MnO	NiO	MgO	CaO	Total
ol1A	81.4(6)	39.5(3)	0.020(16)	0.016(15)	0.052(2)	17.0(4)	0.268(12)	0.158(8)	42.0(7)	0.285(6)	99.30
ol2A	81.8(6)	39.5(3)	0.025(13)	0.008(15)	0.044(2)	16.8(4)	0.260(12)	0.150(8)	42.2(7)	0.274(6)	99.25
ol3A	77.4(6)	38.8(3)	0.024(13)	0.010(14)	0.041(2)	20.3(4)	0.302(13)	0.118(8)	39.1(7)	0.271(6)	99.03
ol4A	77.9(6)	38.7(3)	0.008(13)	0.012(15)	0.040(2)	20.2(5)	0.316(15)	0.136(8)	39.9(4)	0.273(6)	99.65
ol5A	82.9(5)	39.5(3)	0.025(13)	0.022(15)	0.050(2)	15.9(4)	0.245(13)	0.179(9)	43.4(4)	0.270(6)	99.60
ol6A	80.9(6)	39.2(3)	0.019(13)	0.020(15)	0.046(2)	17.6(4)	0.282(14)	0.145(8)	41.8(4)	0.270(6)	99.45
ol7A	81.7(5)	39.5(3)	0.015(13)	0.016(15)	0.046(2)	16.9(4)	0.262(14)	0.114(8)	42.5(4)	0.272(6)	99.65
ol8A	80.5(6)	39.1(3)	0.023(13)	0.016(15)	0.049(2)	18.0(4)	0.282(14)	0.147(8)	41.7(4)	0.276(6)	99.67
ol9A	81.0(6)	39.2(3)	0.018(13)	0.006(15)	0.046(2)	17.5(4)	0.281(14)	0.152(8)	41.9(4)	0.263(6)	99.45
ol10A	81.0(5)	39.1(3)	0.025(11)	0.021(13)	0.049(2)	17.5(4)	0.262(14)	0.168(9)	41.9(4)	0.269(6)	99.28
ol11A	81.7(5)	39.5(3)	0.019(13)	0.008(15)	0.047(2)	16.9(4)	0.260(14)	0.151(8)	42.4(4)	0.263(6)	99.54
ol12A	81.0(6)	39.4(3)	0.038(13)	0.022(15)	1.076(8)	17.4(4)	0.282(14)	0.156(8)	41.6(4)	0.264(7)	100.19

Table 18: Electron microprobe data for Hreggnasi olivines reported as wt% oxides. FeO* assumes all Fe present as FeO. Fo=100MgO/(MgO+FeO*) on a molar basis. These are average concentrations of three point measurements taken for each olivine. Numbers in parentheses adjacent to each oxide value are one sample standard deviation in terms of the least units cited, e.g. 40.6(4) represents 40.6 ± 0.4 . Dashes indicate that the element was not analysed or was below the detection limit of the microprobe.

Hreggnasi (continued)

Ref	Fo	SiO ₂	TiO ₂	Cr ₂ O ₃	Al ₂ O ₅	FeO*	MnO	NiO	MgO	CaO	Total
ol1D	76.9(6)	38.4(3)	0.032(16)	0.001(14)	0.040(2)	21.0(5)	0.320(15)	0.135(8)	39.3(4)	0.257(6)	99.52
ol2D	81.5(5)	39.4(3)	0.034(13)	0.005(15)	0.047(2)	17.1(4)	0.277(14)	0.124(8)	42.2(4)	0.268(6)	99.40
ol3D	81.1(6)	39.2(3)	0.022(13)	0.015(15)	0.047(2)	17.5(4)	0.279(14)	0.154(8)	42.1(4)	0.270(6)	99.63
ol4D	77.4(6)	38.7(3)	0.017(13)	0.007(14)	0.042(2)	20.7(5)	0.273(14)	0.131(8)	39.7(4)	0.166(5)	99.73
ol5D	82.4(5)	39.6(3)	0.022(16)	0.032(15)	0.049(2)	16.4(4)	0.263(14)	0.166(9)	43.2(4)	0.274(6)	99.99
ol6D	81.4(5)	39.3(3)	0.022(13)	0.014(15)	0.052(2)	17.3(4)	0.288(14)	0.153(8)	42.3(4)	0.264(6)	99.62
ol7D	80.5(6)	39.2(3)	0.022(13)	0.015(15)	0.046(2)	18.0(4)	0.280(14)	0.150(8)	41.7(4)	0.285(7)	99.62
ol8D	81.5(5)	39.3(3)	0.019(15)	0.015(15)	0.046(2)	17.1(4)	0.279(14)	0.158(8)	42.4(4)	0.258(6)	99.63
ol9D	81.2(5)	39.2(3)	0.020(13)	0.022(15)	0.047(2)	17.3(4)	0.275(14)	0.144(8)	42.0(4)	0.271(6)	99.36
ol10bD	81.7(5)	39.4(3)	0.011(13)	0.009(15)	0.051(2)	16.9(4)	0.263(14)	0.153(8)	42.5(4)	0.258(6)	99.55
ol10aD	81.9(5)	39.1(3)	0.027(13)	0.013(15)	0.048(2)	16.8(4)	0.266(14)	0.155(8)	42.6(4)	0.257(6)	99.25
ol11D	81.4(5)	39.3(3)	0.028(13)	0.028(14)	0.047(2)	17.3(4)	0.259(14)	0.166(9)	42.3(4)	0.267(6)	99.64
ol12D	81.0(6)	39.2(3)	0.021(13)	0.017(14)	0.046(2)	17.5(4)	0.275(14)	0.144(8)	42.0(4)	0.261(6)	99.47
ol13D	81.3(5)	39.3(3)	0.020(13)	0.009(15)	0.052(2)	17.3(4)	0.283(14)	0.162(9)	42.3(4)	0.265(6)	99.72
ol14D	81.8(5)	39.2(3)	0.014(13)	0.009(15)	0.048(2)	16.9(4)	0.266(14)	0.150(8)	42.6(4)	0.268(6)	99.49
ol15D	81.1(5)	39.1(3)	0.019(13)	0.014(14)	0.047(2)	17.5(4)	0.283(14)	0.157(9)	42.0(4)	0.251(6)	99.36
ol16D	80.9(6)	39.2(3)	0.025(13)	0.007(15)	0.047(2)	17.7(4)	0.282(14)	0.153(8)	42.1(4)	0.257(6)	99.82
ol17D	78.2(6)	38.7(3)	0.032(13)	0.018(15)	0.045(2)	19.9(5)	0.289(14)	0.142(8)	40.1(4)	0.275(6)	99.57
ol18D	80.9(6)	39.1(3)	0.012(13)	0.022(15)	0.048(2)	17.7(4)	0.274(14)	0.152(8)	42.1(4)	0.266(6)	99.67
ol19D	80.9(6)	39.0(3)	0.028(13)	0.010(15)	0.047(2)	17.6(4)	0.279(14)	0.152(8)	42.0(4)	0.260(6)	99.38
ol20D	79.5(6)	39.0(3)	0.019(13)	0.019(15)	0.045(2)	18.8(5)	0.285(14)	0.131(8)	41.0(4)	0.270(6)	99.55
ol21D	80.9(6)	39.0(3)	0.019(13)	0.009(15)	0.046(2)	17.7(4)	0.282(14)	0.123(8)	42.0(4)	0.265(6)	99.43
ol24D	81.2(5)	39.3(3)	0.017(13)	0.015(15)	0.049(2)	17.4(4)	0.274(14)	0.152(8)	42.1(4)	0.273(6)	99.61
ol25D	80.6(6)	39.1(3)	0.026(13)	0.022(14)	0.046(2)	17.9(4)	0.293(14)	0.129(8)	41.7(4)	0.261(6)	99.48
ol26D	80.4(6)	39.1(3)	0.015(13)	0.011(15)	0.045(2)	18.0(5)	0.270(14)	0.133(8)	41.5(4)	0.261(6)	99.28

Table 19: Electron microprobe data for Hreggnasi olivines (continued)

C

Matlab Code